# First observation of the rare decay $K^+ \to \mu^+\nu_\mu\mu^+\mu^-$ at the NA62 experiment

by

Adam M. Tomczak

A thesis submitted to the University of Birmingham
for the degree of *Doctor of Philosophy*

**Supervisors**:
Prof Evgueni Goudzovski
Prof Cristina Lazzeroni
Dr Angela Romano

Particle Physics Research Group
School of Physics and Astronomy
University of Birmingham
September 2024

# Abstract

The first observation of the rare decay $K^+ \to \mu^+\nu_\mu\mu^+\mu^-$ using data collected by the NA62 Experiment in 2017 and 2018 is presented in this thesis. The $K^+ \to \mu^+\nu_\mu\mu^+\mu^-$ branching ratio is measured using the $K^+ \to \pi^+\mu^+\mu^-$ process as a normalisation channel. The number of observed data candidates is 1832, with a background contamination of 168 ± 9. The analysis yields $\mathfrak{B}(K^+ \to \mu^+\nu_\mu\mu^+\mu^-) = (1.307 \pm 0.034_{\mathrm{Stat}} \pm 0.025_{\mathrm{Syst}} \pm 0.012_{\mathrm{Ext}}) \times 10^{-8}$, including a complete treatment of relevant systematic effects.

The complete software package for the ANTI-0 detector, added to the NA62 setup in 2021, was developed by the author within the NA62 software framework and is described in detail. The software tools allowing for short and long-term verification of ANTI-0 data quality are presented, with their output used to summarise the commissioning and performance of the detector in the 2021, 2022 and 2023 NA62 data-taking campaigns.

# Acknowledgments

The presented results could not have been achieved if not for the help, guidance and hard work of many people.

Firstly, the author would like to extend words of gratitude to the trio of his supervisors. The guidance of Evgueni Goudzovski was instrumental in the work on the $K^+ \to \mu^+\nu_\mu\mu^+\mu^-$ analysis, helped the author in understanding of the physics environment of the NA62 Experiment and allowed to better the authors critical thinking skills. The author is grateful to Angela Romano for the training and discussions on the practicalities of operating the KTAG detector, which improved the authors problem-solving skills. The kind words and holistic perspective of Cristina Lazzeroni, as well as the outreach activities conducted under her supervision, helped the author appreciate the full landscape of Particle Physics. Finally, the author would like to thank all three supervisor for their input into the thesis writing process, which elucidated and allowed to correct for numerous issues of both scientific and stylistic nature.

Participating in data-taking activities of the NA62 Collaboration allowed the author to appreciate the ingenuity and complexity of the experimental setup, as well as the hard work necessary to collect good quality physics data. The analysis process illuminated the constant improvement of the NA62 software framework and intricate logistics of data management. The author is hence grateful to all past and present members of the NA62 Collaboration who contributed to data collection, the provision of tools and services necessary for analysis, and the many fruitful discussions.

The author would like to express his gratitude to all past and present fellow Birmingham NA62 PhD students, as well as the Birmingham Particle Physics group in general, for the pleasant working environment and the many small technical issues solved with their help.

On a personal note, the author appreciates the unwavering support of his closest family, instrumental in fostering an environment allowing for personal and professional development, which culminated in the presented work. The author is grateful to his parents for their emotional and material support at all stages of education and inspiring a thorough approach to work and life in general. Perhaps most importantly, the author thanks his wife, Ania, for the countless gestures of kindness and unquestioning support throughout the effort of obtaining the presented results.

# Contents

# List of Figures

# List of Tables

# Declaration of Author's Contribution

The theoretical description of Chapter 2 provides a background for the presented analysis, as well as a broader physics context for the NA62 Experiment at CERN. Chapter 3 contains a summary of the NA62 Experiment, including the beam line, detector and data acquisition system, used to collect the data analysed for this work. The summary of the result on the very rare $K^+ \to \pi^+ \nu \bar{\nu}$ decay on Run1 (2017 and 2018) NA62 data [1] in Section 3.5 aids in understanding the experimental design and highlights the overall performance of the setup.

The studies on motivation for the introduction of the ANTI-0 detector and the details of detector design, in which the author did not participate, are contained in Sections 4.1 and 4.2 to contextualise the development of the complete software package for the ANTI-0 detector within the NA62 software framework. The detector simulation of Section 4.3.1 and analysis-level tools described in Sections 4.3.3 and 4.3.4 were implemented by the author. The reconstruction algorithm of Section 4.3.2, written by the author, relies on existing NA62 software framework functionality, including the treatment of time corrections and methods for “digitisation” of simulated data. Section 4.4 is entirely the author's work. The author served as the data quality responsible for the ANTI-0 during the 2021, 2022 and 2023 data-taking campaigns, verifying the long-term performance of the detector using the developed tools.

The measurement of the branching ratio of the rare $K^+ \to \mu^+ \nu_\mu \mu^+ \mu^-$ decay using Run1 NA62 data presented in Chapter 5 is entirely the author's work. The $K^+ \to \pi^+ \mu^+ \mu^-$ process was used as a normalisation channel, with the general outline of the normalisation event selection following the approach of a recent NA62 publication on this decay [2]. The $K^+ \to \mu^+ \nu_\mu \mu^+ \mu^-$ analysis utilises the standard tools available within the NA62 software framework, including the different simulation modes described in Section 5.3. The author contributed to the maintenance of the “Fast” functionality, extended the “Capped” simulation mode to include the $K^+ \to \pi^+ \pi^- \mu^+ \nu_\mu$ decay and was part of the team that implemented the propagation of the decision of the “capping” algorithm for individual particles to the analysis level.

No other qualifications have been achieved with the work reported in this thesis.

# Chapter 1

# Introduction

High Energy Physics, often referred to as Particle Physics, is a field of study dedicated to probing the smallest known constituents of matter and their interactions. Despite being divided into the theoretical and experimental branches, the success of Particle Physics as a whole crucially depends on the interplay between the two, as demonstrated by its history. To provide one such example, the discovery of charge-parity (CP) violation in the neutral kaon system in the 1960s [3] led to the theoretical postulation of necessary existence of two third-generation quarks in the 1970s [4], the last of which, the top quark, was conclusively observed only in 1995 [5][6].

Decades of scientific effort culminated in the Standard Model of High Energy Physics (SM), a theoretical framework encompassing all the known elementary particles and three of the four fundamental interactions. The SM is one of the most comprehensive and extensively tested scientific theories, completed by the discovery of the Higgs boson in 2012 [7][8]. As exemplified by the case of CP violation observed in the neutral kaon system, the SM describes not only the matter contents of the universe and their properties but also allows for numerical predictions of the fundamental processes and symmetries they are subject to. This second aspect enables tests of the framework through precision measurements, where instead of qualitative verification of a process, numerical values describing its properties can be extracted from experimental data and compared to the most accurate available theoretical prediction. With the particle content of the SM complete and the limited phase-space for direct detection of new Beyond-Standard-Model particles and forces given the current experimental capabilities, the field increasingly relies on such precision measurements as a source of indirect evidence of new physics. Such evidence takes the form of a statistically significant deviation in a parameter predicted by the theoretical framework to high precision or a violation of a fundamental symmetry. While direct detection of new particles is fundamentally limited by the energies achievable at accelerator facilities (with the current limit at the TeV scale), precision measurements at the intensity frontier of the meson sector allow access to new physics models at mass scales in excess of 100 TeV [9].

The NA62 Experiment at the European Organization for Nuclear Research (CERN) was designed and operates with the goal of a precise measurement of the ultra-rare decay of positively charged kaon, $K^+ \to \pi^+ \nu \bar{\nu}$, in line with the above approach. The experimental complexity and rare nature of this decay allows for other measurements in the kaon sector using NA62 data, including the observation and quantitative verification of rare kaon decays, such as the yet unmeasured $K^+ \to \mu^+ \nu_\mu \mu^+ \mu^-$ process. The measurement of the $K^+ \to \mu^+ \nu_\mu \mu^+ \mu^-$ branching ratio provides a test of the next-to-leading order SM prediction [10]. The process offers access to form factors for radiative kaon decays and potential reach into the range of new physics models capable of addressing the muon $g-2$ anomaly [11]. The analysis of NA62 data collected in 2017 and 2018 (Run1) in search of the $K^+ \to \mu^+\nu_\mu\mu^+\mu^-$ decay is the main topic of the presented work.

The SM and the theoretical framework employed for the most precise prediction of the rate of the rare $K^+ \to \mu^+\nu_\mu\mu^+\mu^-$ decay are described in Chapter 2. Chapter 3 covers the beam, detector and data acquisition system of the NA62 experiment, concluding with a summary of the Run1 $K^+ \to \pi^+\nu\bar{\nu}$ result. Chapter 4 introduces the ANTI-0 detector, a new system added to the NA62 experiment in 2021, and describes the software package used to simulate, reconstruct and verify the quality of data produced by it. A summary of ANTI-0 performance in 2021 to 2023 data-taking campaigns is included. The measurement of the branching ratio of the $K^+ \to \mu^+\nu_\mu\mu^+\mu^-$ decay using Run1 NA62 data is presented in Chapter 5. The descriptions of analysis strategy, event selections, used real and simulated data samples and background modelling techniques are complemented by a complete treatment of relevant systematic effects, leading to the first observation of this decay and a precise measurement of the branching ratio.

# Chapter 2

# Theoretical framework

## 2.1 The Standard Model of Particle Physics

The Standard Model of Particle Physics (SM) is a self-consistent description of three out of four fundamental forces and all the known elements of matter. Gravitational interactions fall outside the scope of the SM, with the gravitational coupling being multiple orders of magnitude smaller than those of the other forces. The SM is a renormalisable gauge quantum field theory, with the matter particles represented by fundamental fields and interactions driven by local Abelian ($U(1)_Y$) and non-Abelian symmetries, with the total symmetry group of $SU(3)_C \times SU(2)_L \times U(1)_Y$.

The particle content comprises twelve fermions of spin 1/2, further divided into six quarks and six leptons, five vector bosons of spin 1, mediators of the fundamental forces, and the Higgs boson of spin 0, all of which are depicted in Figure 2.1. The SM also includes the antiparticles of the fermions, that is particles with the same mass and opposite algebraically additive quantum numbers, such as electric charge, weak isospin or colour charge. The six distinct quark flavours: up, down, charm, strange, top and bottom, can be grouped into three generations or two types, as shown in Figure 2.1. There are three lepton flavours, where each charged lepton is complemented by a neutrino, both defined as having a positive unit of lepton flavour charge, with the antiparticles carrying a negative unit. Values for the nine masses of quarks and charged leptons are not inherent properties of the SM but remain to be measured as free parameters, while the three neutrinos are massless in the SM.

The unbroken $SU(3)_C$ group of the SM represents the strong force, mathematically formulated as Quantum ChromoDynamics (QCD) [12]. QCD describes the interactions between quarks as mediated by gluons, through the *colour* degree of freedom. The coupling strength of strong interaction depends on the energy, with its dependence defined by theory in contrast to the overall scale, $g_S$. Another free parameter of the SM introduced in the QCD sector is the CP violating parameter, $\theta_{QCD}$. The parameter is experimentally constrained to $\lesssim 10^{-10}$ [13] by measurements of the electric dipole moment of a neutron [14] [15], with this fine-tuning referred to as the “strong CP problem”. While not directly enforced by QCD, the strong interaction exhibits colour confinement, i.e. the inability to directly observe particles of non-zero colour charge. This leads to individual quarks only being observable as part of hadrons, composite systems of at least two quarks.

The remaining two forces, weak and electromagnetic, are represented by the broken $SU(2)_L \times U(1)_Y$ symmetry, together referred to as the electroweak interaction [16]. The electroweak bosons include the

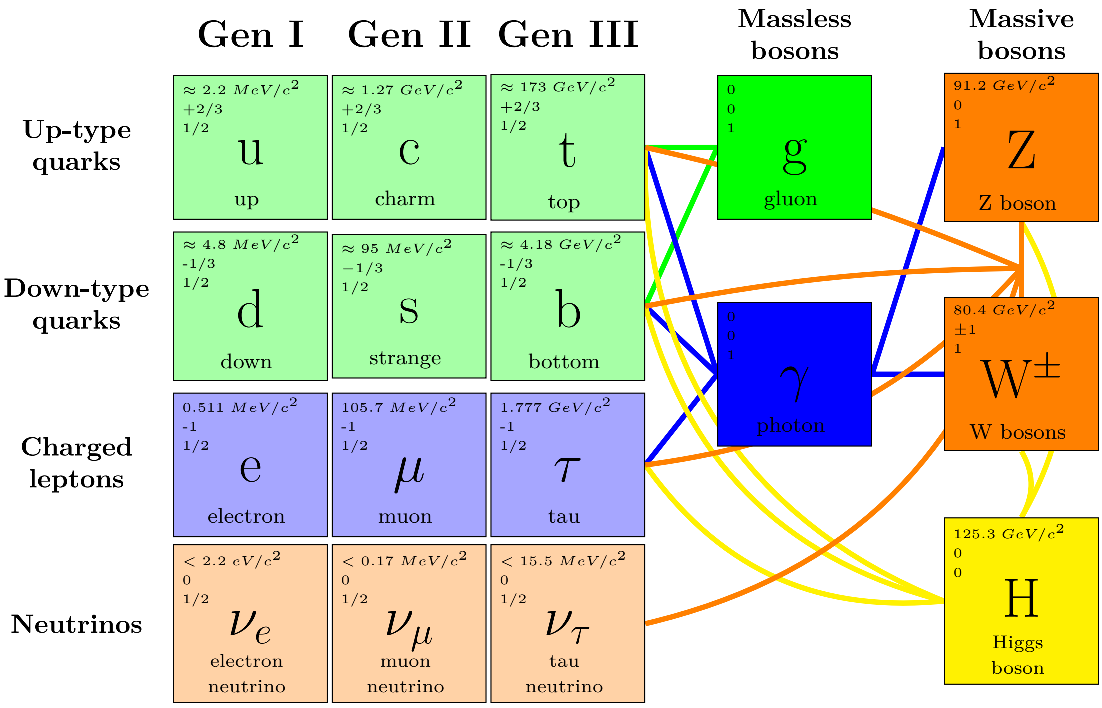

Figure 2.1: Particle content of the SM with the masses, electric charges and spins top to bottom. Coloured lines show allowed couplings between bosons and fermions, excluding self-interactions.

photon, the massless mediator of electromagnetic interaction, as well as the massive $Z^0$, $W^\pm$ particles. The spontaneous breaking of the $SU(2)_L \times U(1)_Y$ symmetry is caused by the Higgs field [17], the interactions with which generate the masses of the electroweak bosons, quarks and charged leptons. The electroweak scalar sector contributes a further four free parameters of the SM, namely: the electromagnetic coupling, $\alpha$, the Weinberg mixing angle, the masses of the $Z^0$ and Higgs bosons, $m_{Z^0}$ and $m_H$ respectively. The final four parameters originate from couplings of quarks to the $W^\pm$ bosons described in the next section, completing the set of nineteen independent variables defining the SM.

### 2.1.1 Flavour structure of the Standard Model

Contrary to interactions mediated by the gluons, photons and $Z^0$ bosons, those involving the $W^\pm$ do not conserve flavour symmetry. The symmetry breaking leads to non-alignment of the mass (strong) and interaction (weak) eigenstates of quarks. By convention, only the down-type quark eigenstates are rotated by the complex unitary Cabbibo-Kobayashi-Masakawa (CKM) matrix [4], $V_{CKM}$, so that

$$\underbrace{\begin{bmatrix} d \\ s \\ b \end{bmatrix}}_{\substack{\text{mass}\\\text{eigenstates}}} = V_{CKM} \underbrace{\begin{bmatrix} d' \\ s' \\ b' \end{bmatrix}}_{\substack{\text{weak}\\\text{eigenstates}}} = \begin{pmatrix} V_{ud} & V_{us} & V_{ub} \\ V_{cd} & V_{cs} & V_{cb} \\ V_{td} & V_{ts} & V_{tb} \end{pmatrix} \begin{bmatrix} d' \\ s' \\ b' \end{bmatrix}. \tag{2.1.1}$$

The magnitude of matrix elements determines the coupling strength entering at a vertex containing the respective pair of quarks. The CKM matrix can be fully described by four parameters, often described as three angles for inter-generation mixing and a single complex phase, introducing CP

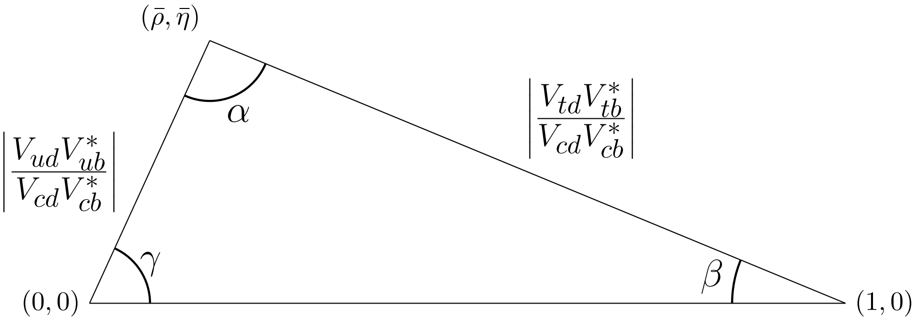

Figure 2.2: One of the CKM unitarity triagnles.

violation. The Wolfenstein parametrisation [18] can be used to exhibit the element hierarchy,

$$V_{CKM} = \begin{pmatrix} 1-\lambda^2 & \lambda & A\lambda^3(\rho - i\eta) \\ -\lambda & 1-\lambda^2 & A\lambda^2 \\ A\lambda^3(1-\rho-i\eta) & -A\lambda^2 & 1 \end{pmatrix} + O(\lambda^4), \tag{2.1.2}$$

where

$$\lambda = \frac{|V_{us}|}{\sqrt{|V_{ud}|^2 + |V_{us}|^2}}, \quad A = \frac{1}{\lambda}\left|\frac{V_{cb}}{V_{us}}\right|, \quad \bar{\rho} + i\bar{\eta} = -\frac{V_{ud}V_{ub}^*}{V_{cd}V_{cb}^*} \tag{2.1.3}$$

with

$$\bar{\rho} = \rho(1 - \lambda^2/2 + ...) \quad \text{and} \quad \bar{\eta} = \eta(1 - \lambda^2/2 + ...). \tag{2.1.4}$$

Global fits combining all experimental measurements for the parameters give [13]

$$\lambda = 0.2250 \pm 0.00067, \quad A = 0.826^{+0.018}_{-0.015}, \quad \bar{\rho} = 0.159 \pm 0.010, \quad \bar{\eta} = 0.348 \pm 0.010. \tag{2.1.5}$$

While the CKM matrix elements can be measured independently, the Wolfenstein parametrisation underlines CKM suppression, i.e. a reduction in the rate of processes involving quarks from different generations.

The variety of experimentally measurable combinations of the matrix elements allows to over-constrain the values, testing the self-consistency of the SM. The unitary character of $V_{CKM}$ can be verified making use of the identities $\Sigma_i V_{ij} V_{ik}^* = \delta_{jk}$ and $\Sigma_j V_{ij} V_{kj}^* = \delta_{ik}$, which provide six closed triangles in the complex plane. Of particular interest is the unitary triangle

$$V_{ud}V_{ub}^* + V_{cd}V_{cb}^* + V_{td}V_{tb}^* = 0, \tag{2.1.6}$$

with all terms having a leading contribution of order $A\lambda^3$. By dividing all sides by $V_{cd}V_{cb}^*$, one obtains the triangle shown in Figure 2.2, with corners located at $(0, 0)$, $(1, 0)$ and $(\bar{\rho}, \bar{\eta})$.

## 2.2 Beyond the Standard Model

Despite the enormous success and many decades of development, the SM does not address all the experimentally observed aspects of the microscopic universe, both in terms of its total content and precise predictions of the properties of its known components. Extensions to the theoretical framework, as well as empirical evidence in favour of existence of additional particles and phenomena are often collectively referred to as Beyond Standard Model (BSM) physics.

### 2.2.1 Dark Matter

A variety of astronomical evidence implies the presence of Dark Matter, defined as interacting gravitationally but not electromagnetically. This property makes it susceptible only to indirect observation on astronomical scales, as exemplified by the evidence for it found in galaxy rotation curves [19] and gravitational lensing [20]. Measurements of the energy density of different components of the universe, together with a study of the anisotropies of the Cosmic Microwave Background find the baryonic matter content (fraction of total matter energy density) to be 15.6%, with Dark Matter contributing the remaining 84.4% [13].

Decades of experimental searches for Dark Matter particles, including production at colliders, detection by nuclear recoil and annihilation into SM particles, have substantially limited the theoretically allowed phase-space, both in terms of candidate masses and the strength of coupling to SM particles. While new experiments, making use of developments in detection techniques, continue to probe the remaining regions of phase-space, ongoing theoretical efforts aim to utilise alternative mechanisms to explain the phenomenon, see Reference [21].

### 2.2.2 Matter-antimatter asymmetry

Another shortcoming of the SM from the macroscopic perspective is the inability to quantitatively explain the baryonic asymmetry of the universe, that is the prevalence of matter over antimatter. Given the empirical evidence for near homogeneous and symmetric production of matter and antimatter during the Big Bang, such an asymmetry necessitates the presence of Baryon-number and CP-violating processes out of thermal equilibrium [22]. Within the SM, CP-violation can enter through two free parameters: the complex phase of the CKM matrix and $\theta_{QCD}$. Measured values for both [13] are inconsistent with the observed matter-antimatter asymmetry.

### 2.2.3 Neutrino masses

With no mechanism for generating masses for neutrinos within the SM, they should remain the only elementary fermions with zero mass. However, both neutrinos generated in the Sun and the atmosphere were observed to oscillate [23] [24] [25], i.e. change their flavour as they propagate through space. This phenomenon in only possible for massive particles and implies the non-alignment of mass and weak interaction neutrino eigenstates. A theoretical description analogous to the treatment of quarks, as described in Section 2.1.1, results in the PNMS mixing matrix [26] [27].

The existence of neutrino masses necessitates an extension of the SM Lagrangian with a mass-generating term. Such a term can take two forms, depending on whether the particles exhibit Majorana or Dirac properties, i.e. whether they are or not their own antiparticles. The former case would imply of a set of distinct, experimentally measurable phenomena, such as neutrinoless double beta decay.

### 2.2.4 Muon anomalous magnetic moment

Muons, being charged fermions satisfying the Dirac equation, have an intrinsic magnetic dipole moment

$$\vec{M} = g_\mu \frac{e}{2m_\mu} \vec{S}, \tag{2.2.1}$$

where $\vec{S}$ is the spin of the particle, with $m_\mu$, $e$ and $g_\mu$ defining the mass, electric charge and gyromagnetic ratio of the muon. Excluding quantum loop effects, the Dirac theory gives $g_\mu = 2$, leading to the definition of the anomalous magnetic moment as

$$a_\mu = \frac{g_\mu - 2}{2}. \tag{2.2.2}$$

Within the SM, the leading contribution to $a_\mu$ comes from electron, muon and tau loops through Quantum ElectroDynamics (QED), precisely calculated to 5-loop order. A second class involves electroweak processes mediated by $W$, $Z$ and Higgs bosons. Quark and gluon loop contributions, jointly termed hadronic, present the largest computational challenge and involve substantial systematic uncertainties. The complete prediction, with the error dominated by the hadronic component, gives [28]

$$a_\mu^{SM} = (116\,591\,810 \pm 43) \times 10^{-11}. \tag{2.2.3}$$

Measurements of the muon anomalous magnetic moment have been performed by a succession of experiments, in line with increasingly precise theoretical predictions. The Muon $g-2$ Collaboration [29] at the Fermi National Laboratory is the latest effort in this domain, motivated by the previously observed discrepancy between theory and measurement and is expected to provide a final result with the precision of 0.14 parts per million. The current experimental world average for the anomalous magnetic moment is [13]

$$a_\mu^{exp} = (116\,592\,059 \pm 22) \times 10^{-11}, \tag{2.2.4}$$

with the small uncertainty driven by the precision of the latest results from the Muon $g-2$ Collaboration [30]. The resultant discrepancy of $5.2\sigma$ significance, referred to as the muon $g-2$ anomaly, could be a signature of BSM physics, with its importance reduced by the discrepancies in hadronic cross section data used for the theoretical prediction of the hadronic contribution. Recent advances in lattice QCD (see [31] for an overview) allow for an independent estimate for the hadronic contribution [32] of similar precision to the value obtained from data-driven methods used in the most recent SM estimate [28]. The former method yields a $a_\mu^{SM}$ prediction significantly closer to the experimentally measured value, with a $2.1\,\sigma$ tension between the theoretical approaches, where $\sigma$ is the sum in quadrature of the uncertainties on the two theoretical predictions. Additional independent lattice QCD calculations and collection of hadronic data for the latter method are hence in progress.

## 2.3 Kaon physics

Kaons, mesons composed of a single first generation quark (anti-quark) and a strange anti-quark (quark), can be described as the minimal flavour laboratory, being the lightest particles exhibiting all phenomena due to the flavour structure of the quark sector of the SM. There are four weak eigenstates of kaons, with their properties listed in Table 2.1. Since their discovery in 1947 from cosmic rays [33], kaons have played a key role in the the development of the SM. With only 3 known quarks (up, down and strange) the CP symmetry as initially observed in the $K_S^0$ and $K_L^0$ system motivated the introduction of the Glashow-Iliopoulos-Maiani (GIM) mechanism [34], which necessitated the existence of a fourth quark, the charm. The subsequent discovery of CP violation in the neutral kaon system [3] led to the formulation of the CKM matrix and the concurrent postulation of two heavy quarks, the bottom and the top [4].

| Name | Quark content | Mass $[MeV/c^2]$ | Lifetime $[10^{-8}\ s]$ | Main decay mode |
|---|---|---|---|---|
| $K^+$ | $u\bar{s}$ | $493.677 \pm 0.016$ | $1.238 \pm 0.002$ | $\mu^+\nu_\mu$ |
| $K^-$ | $\bar{u}s$ | $493.677 \pm 0.016$ | $1.238 \pm 0.002$ | $\mu^-\bar{\nu_\mu}$ |
| $K_S^0$ | $\frac{d\bar{s}-\bar{d}s}{\sqrt{2}}$ | $497.611 \pm 0.013$ | $(8.954 \pm 0.004) \times 10^{-3}$ | $\pi^+\pi^-$ |
| $K_L^0$ | $\frac{d\bar{s}+\bar{d}s}{\sqrt{2}}$ | $497.611 \pm 0.013$ | $5.116 \pm 0.021$ | $\pi^\pm e^\mp \nu_e$ |

Table 2.1: Selected properties of kaon mass eigenstates. [13]

Given their position in the mass hierarchy of flavoured particles and relative simplicity of decay final states, kaons have been extensively studied throughout the past seven decades. With the structure of the SM firmly established, the focus in the kaon sector has shifted to measurements of rare decays, where statistically significant deviations from the SM rates and spectra would imply contribution from BSM processes.

### 2.3.1 $K \to \pi\nu\bar{\nu}$ decays

The $K \to \pi\nu\bar{\nu}$ decays are often referred to as the kaon golden modes, given the small magnitude and theoretical cleanliness of their predicted SM branching ratios. They are mediated by flavour-changing neutral currents, processes highly suppressed within the SM due to both the structure of the CKM matrix and the GIM mechanism, with leading contributions from $Z^0$ penguin diagrams and a sizeable contributions from $W$ box diagrams, demonstrated in Figure 2.3.

The small size of theoretical uncertainty on the expected branching ratios, $\mathfrak{B}$, is due to the inclusion of next-to-leading-order (NLO) QCD corrections to the top quark contributions [35], next-to-next-to-leading-order (NNLO) QCD corrections to the charm contribution [36] and NLO electroweak corrections to both top and charm contributions [37] [38], as well as the treatment of isospin breaking and non-perturbative effects [39] [40]. The uncertainties are dominated by external contributions from

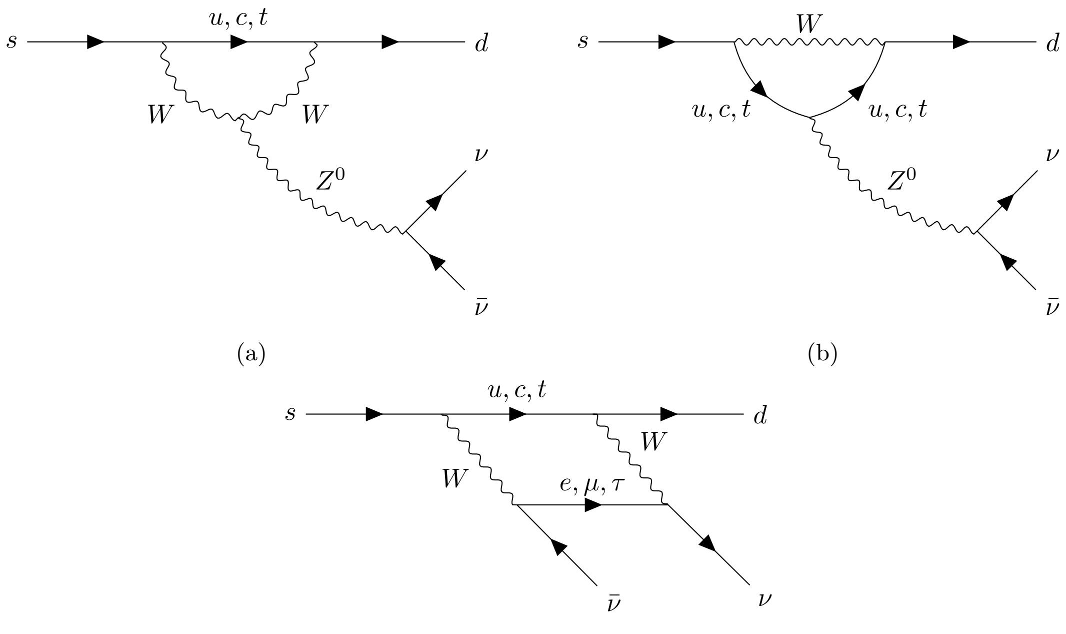

(a)

(b)

(c)

Figure 2.3: Leading order Feynman diagrams for the $K \to \pi\nu\bar{\nu}$ decays.

CKM matrix parameters. Using $|V_{us}|$, $|V_{cb}|$, $|V_{ub}|$ and $\gamma = \arg(-V^*_{ud}V_{ub}/V_{cd}V^*_{cd})$ to define the matrix yields the explicit dependencies [41]

$$\mathfrak{B}(K^+ \to \pi^+\nu\bar{\nu}) = (8.39 \pm 0.30) \times 10^{-11} \cdot \left[\frac{|V_{cb}|}{40.7 \times 10^{-3}}\right]^{2.8} \cdot \left[\frac{\gamma}{73.2^\circ}\right]^{0.74}, \tag{2.3.1}$$

$$\mathfrak{B}(K^0_L \to \pi^0\nu\bar{\nu}) = (3.36 \pm 0.05) \times 10^{-11} \cdot \left[\frac{|V_{ub}|}{3.88 \times 10^{-3}}\right]^{2} \cdot \left[\frac{|V_{cb}|}{40.7 \times 10^{-3}}\right]^{2} \cdot \left[\frac{\sin\gamma}{\sin 73.2^\circ}\right]^{2}. \tag{2.3.2}$$

Tree-level measurements can be used to extract the global averages for the four CKM parameters [42], leading to the numerical predictions of the branching ratios [43]

$$\mathfrak{B}(K^+ \to \pi^+\nu\bar{\nu}) = (8.19 \pm 0.61) \times 10^{-11}, \tag{2.3.3}$$

$$\mathfrak{B}(K^0_L \to \pi^0\nu\bar{\nu}) = (2.78 \pm 0.30) \times 10^{-11}. \tag{2.3.4}$$

The small predicted SM branching ratios of the $K \to \pi\nu\bar{\nu}$ decays make them sensitive to a variety of potential BSM contributions [44], further enhancing the importance of their precise measurements.

The neutral decay remains unobserved and is currently addressed by the KOTO collaboration [45], which was able to set the experimental upper limit at [46]

$$\mathfrak{B}(K^0_L \to \pi^0\nu\bar{\nu})^{KOTO}_{exp} < 2.1 \times 10^{-9} \text{ at } 90\% \text{ CL}. \tag{2.3.5}$$

The charged decay was measured by two experiments at the Brookhaven National Laboratory(BNL), E747 and E949, giving a combined result of

$$\mathfrak{B}(K^+ \to \pi^+\nu\bar{\nu})^{E747,E949}_{exp} = (1.73^{+1.15}_{-1.05}) \times 10^{-10} \tag{2.3.6}$$

based on the observation of 7 signal candidates in two kinematic regions [47] [48]. The NA62 experiment at CERN was designed to measure $\mathfrak{B}(K^+ \to \pi^+\nu\bar{\nu})$ with a 10% precision. Using data collected in the 2016-2018 period, a result of

$$\mathfrak{B}(K^+ \to \pi^+\nu\bar{\nu})^{NA62\,Run1}_{exp} = (10.6\,^{+4.0}_{-3.4}|_{stat} \pm 0.9_{syst}) \times 10^{-11} \tag{2.3.7}$$

was achieved from 20 signal candidates [1], with a second, ongoing data-taking campaign started in 2021.

## 2.4 $K^+ \to \mu^+\nu_\mu\mu^+\mu^-$ decay

The $K^+ \to \mu^+\nu_\mu\mu^+\mu^-$ process remains the only unmeasured of the four $K \to l\nu l'\bar{l}'$ decays, where $l, l' \in e, \mu$. The B787 experiment at BNL established the following constraint on the branching ratio [49]

$$\mathfrak{B}^{B787}_{exp}(K^+ \to \mu^+\nu_\mu\mu^+\mu^-) < 4.1 \times 10^{-7} \text{ at } 90\% \text{ CL}. \tag{2.4.1}$$

A general branching ratio, $\mathfrak{B}$, of particle P is defined as

$$\mathfrak{B}(P \to D_0) = \frac{\Gamma(P \to D_0)}{\sum\limits_n \Gamma(P \to D_n)}, \tag{2.4.2}$$

where $\Gamma(P \to D_0)$ is the partial width of the decay into final state $D_0$ and the set $n$ encompasses all the allowed decays channels of the particle. An individual decay width can be further parameterised as

$$\Gamma(P \to D_0) = \frac{1}{2m_P} \int |A(P \to D_0)|^2 d\Phi(D_0), \tag{2.4.3}$$

with $A(P \to D_0)$, the amplitude, being the matrix element describing the dynamics of the process, $\Phi(D_0)$ the allowed kinematic phase-space of the final state $D_0$ and $m_P$ the mass of the parent particle.

The most recent prediction of the $K^+ \to \mu^+\nu_\mu\mu^+\mu^-$ decay width was obtained using chiral perturbation theory, $\chi PT$. The following subsections introduce $\chi PT$ and summarise the calculation of the SM expectation for $\mathfrak{B}(K^+ \to \mu^+\nu_\mu\mu^+\mu^-)$. The final state of the $K^+ \to \mu^+\nu_\mu\mu^+\mu^-$ decay allows for investigating BSM models with new forces coupling preferentially to muons and consistent with the observed muon anomalous magnetic moment. The chapter concludes with an outline of such a BSM model and a summary of the estimated sensitivity of the $K^+ \to \mu^+\nu_\mu\mu^+\mu^-$analysis to that model. While the BSM model was not addressed as part of the analysis described in this thesis, it will be pursued as a natural extension of the work presented in Chapter 5.

### 2.4.1 Chiral Perturbation Theory

Due to asymptotic freedom of the parton (gluon and quark) fields at low energies in QCD, analytic derivation of hadronic interactions from the SM Lagrangian is not possible in the low-energy regime. Instead, one can resort to constructing an effective field theory, that is one where only a small number of degrees of freedom is kept, with the remainder of free parameters of the underlying theory integrated out and the structure of the theory itself absorbed into effective coupling constants. Chiral perturbation theory is an example of such an approach, where the remaining degrees of freedom are the masses of the three lightest quarks, $m_q,\ q \in \{u, d, s\}$, which can be parameterised using the masses if the light meson octet, $\{\pi^0, \pi^\pm, K^0, \bar{K}^0, K^\pm, \eta\}$, with the strong interaction parameterised with respect to hadronic and not partonic states.

The $\chi PT$ name derives from QCD exhibiting a perfect chiral symmetry in the limit $m_q \to 0\ \forall\, q \in \{u, d, s, c, t, b\}$. Looking at sector of the three lightest quarks, the explicit spontaneous chiral symmetry breaking occurs due to $m_q \neq 0\ \forall\ q \in \{u, d, s\}$. The effective Lagrangian, $\mathcal{L}$, is then extended to include electroweak interactions, parameterised by a set of low-energy couplings (LECs). The resulting Lagrangian gives asymptotically stable hadronic states in the low-energy regime, enabling perturbative calculations, expanding in powers of quark masses and momentum, $p$. The $p$-order of the calculation defines the number of required LECs, which cannot be computed analytically and hence are taken from empirical measurements. $\chi PT$ is valid only up to an energy scale corresponding to the breaking of this approximate symmetry, $\Lambda_X \approx 1.2\,\text{GeV}$ [50]. Detailed overviews of $\chi PT$ can be found in References [51][52][53].

### 2.4.2 Standard Model Branching Ratio

Given $\Lambda_X > m_K$, chiral perturbation theory is frequently used for numerical predictions in the kaon sector. The computation of $\mathfrak{B}_{SM}(K^+ \to \mu^+\nu_\mu\mu^+\mu^-)$ to order $p^4$, as described in Reference [10], was motivated by the availability of the relevant $\chi PT$ LECs and will be summarised here. All Greek symbols excluding $\nu$ appearing in equations of this subsection define four-vector indices from the set $\{0, 1, 2, 3\}$ that are implicitly summed over according to the Einstein summation convention.

The four-momenta involved in a $K^+ \to l\nu l'\bar{l}'$ decay can be labelled as

$$K^+(p) \to l(p_l)\nu(p_\nu)l'(p_1)\bar{l}'(p_2). \tag{2.4.4}$$

The matrix element for the process is

$$T = -iG_F eV_{us}^* \bar{\epsilon}_\rho \big\{ F_K \bar{L}^\rho - \bar{H}^{\rho\mu} l_\mu \big\}, \tag{2.4.5}$$

with

$$\begin{aligned} \bar{L}^\rho &= m_l \bar{u}(p_\nu)(1+\gamma_5)\Big\{ \frac{2p^\mu - q^\mu}{2pq - q^2} - \frac{2p_l^\mu + \not{q}\gamma^\mu}{2p_l q + q^2} \Big\} v(p_l), \\ l^\mu &= \bar{u}(p_\nu)\gamma^\mu(1-\gamma_5)v(p_l), \\ \bar{H}^{\rho\mu} &= iV_1 \epsilon^{\rho\mu\alpha\beta} q_\alpha p_\beta - A_1(qWg^{\rho\mu}) - W^\rho q^\mu) \\ &\quad - A_2(q^2 g^{\rho\mu} - q^\rho q^\mu) - A_4(qWq^\rho - q^2 W^\rho)W^\mu, \end{aligned} \tag{2.4.6}$$

where

$$\begin{aligned} A_4 &= \frac{F_K}{m_{K^+}^2 - W^2} \frac{2F_V^K(q^2) - 1}{q^2} + A_3, \\ \bar{\epsilon}^\mu &= \tfrac{e}{q^2} \bar{u}(p_2)\gamma^\mu v(p_1). \end{aligned} \tag{2.4.7}$$

The four-momenta

$$q = p_1 + p_2, \quad W = p_l + p_\nu = p - q \tag{2.4.8}$$

characterise the transfer to the dilepton ($l'\bar{l}'$) pair and the virtual W$^+$ boson respectively.

The three constants multiplying both terms of Equation 2.4.5 are the electric charge, $e$, the Fermi constant $G_F$ and the CKM matrix element $V_{us}$, underlining the electro-weak nature of the decay. The $\bar{\epsilon}^\mu$ symbol defines the polarisation vector of the virtual photon, satisfying $q_\mu \bar{\epsilon}^\mu = 0$. The outgoing states of the four leptons are described by spinors $u(p_x)$ , $v(p_x)$, which are solutions to the covariant form of Dirac equations

$$(\gamma_\mu p_x^\mu - m)u(p_x) = 0, \quad (\gamma_\mu p_x^\mu + m)v(p_x) = 0, \tag{2.4.9}$$

with the contraction $\not{q} = \gamma_\mu q^\mu$ and $\gamma^\mu$ being the Dirac gamma matrices. Spinor conjugate forms are $\bar{u}(\bar{v}) = u(v)^\dagger \gamma_0$, exploiting the hermitian conjugates $u^\dagger(v^\dagger)$. The matrix $\gamma_5$ is the product $i\gamma_0\gamma_1\gamma_2\gamma_3$, and $\epsilon^{\rho\mu\alpha\beta}$ and $g^{\rho\mu}$ are the totally antisymmetric and metric tensors, with the latter defining a contravariant four-vector as $p^\mu = g^{\mu\rho}p_\rho$. The $V_i$ and $A_i$ symbols represent the amplitudes used for the deconstruction of the vector and axial-vector weak form factors, while $F$ and $F_K$ are scaled psuedoscalar decay constants for the charged pion and kaon respectively. The electromagnetic form factor of the positively charged kaon is denoted by $F_V^K(q^2)$, with $m_{K^+}$ representing the $K^+$ mass.

Considering the physics of the process, there are three general types of diagrams contributing to the matrix element. Bremsstrahlung of the final state muon and the incoming $K^+$ are shown in Figures 2.4 a) and b) respectively and represented by first term of Equation 2.4.5, jointly referred to as the inner bremsstrahlung. Structure-dependent processes, i.e. interactions of the virtual photon with the hadronic structure of the $K^+$, are described by the second term of Equation 2.4.5 and depicted in the Figure 2.4 c).

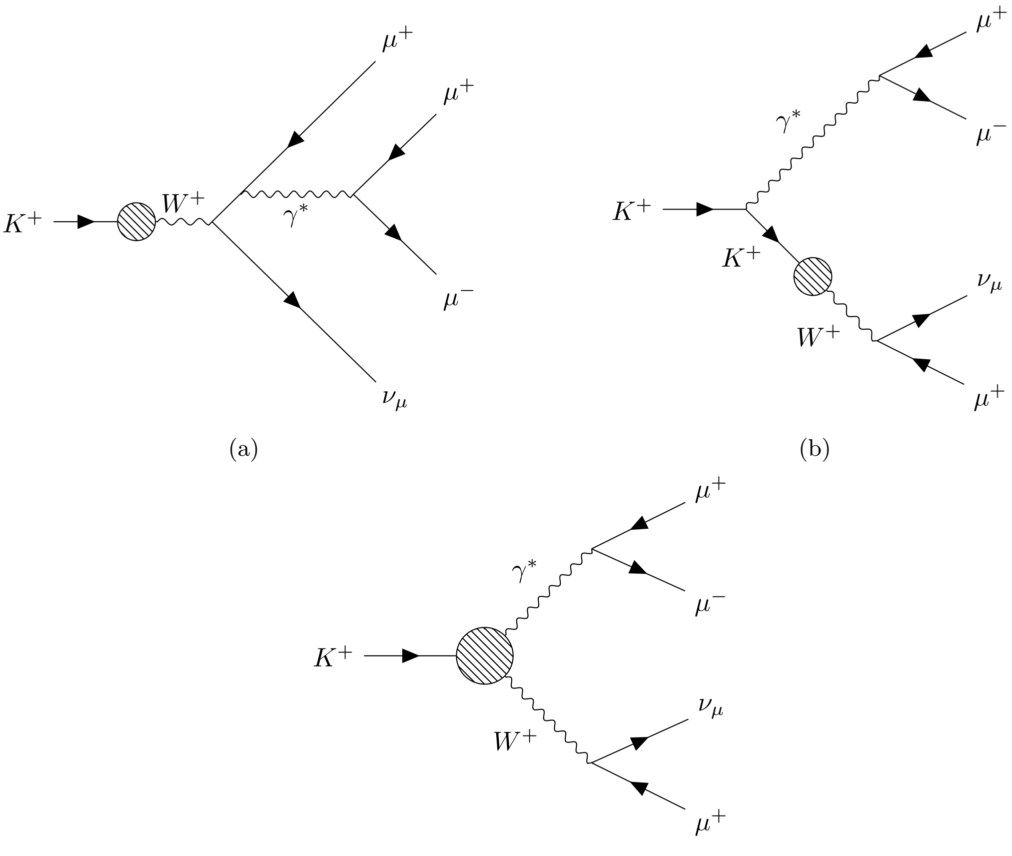

(a) (b) (c)

Figure 2.4: Three types of Feynman diagrams contributing to the $K^+ \to \mu^+\nu_\mu\mu^+\mu^-$ decay amplitude.

To leading order of $\chi PT$, all the weak form factors are set to zero, with $F_V^K(q^2) = 1$ and $F_K = F$. This results in tree-level contributions from inner bremsstrahlung only. At next-to-leading, i.e. $p^4$, order, the form factors take the form:

$$\begin{aligned} V_1 &= -\frac{1}{8\pi^2 F}, \\ A_1 &= -\frac{4}{F}(L_9^r + L_{10}^r), \\ A_2 &= -\frac{2F_K(F_V^K(q^2) - 1)}{q^2}, \\ A_3 &= 0, \end{aligned} \tag{2.4.10}$$

with $F_V^K(q^2)$ retaining the kinematic dependence and $L_9^r$, $L_{10}^r$ being coupling constants parameterising explicit local action in the Lagrangian. The form factor amplitudes $F_A$, $R$, $F_V$ used by the PDG [13] can be expressed as

$$(F_A, R, F_V) = -\frac{1}{\sqrt{2}m_{K^+}}(A_1, A_2, V_1). \tag{2.4.11}$$

In the effective theory at next-to-leading order, the electromagnetic form factor takes the form

$$\begin{aligned} F_V^K(q^2) = 1 &+ \left(\frac{4}{3}\frac{L_9^r}{F} - \frac{1}{144\pi^2 F^2}\right)q^2 \\ &- \frac{1}{48\pi^2 F^2}\sum_{i=\pi,K}\left[\frac{1}{4}(q^2 - 4m_i^2)\Big[1 - \frac{\sqrt{q^2 - 4m_i^2}}{q}\log\frac{q + \sqrt{q^2 - 4m_i^2}}{q - \sqrt{q^2 - 4m_i^2}}\Big] - m_i^2\right]. \end{aligned} \tag{2.4.12}$$

| Quantity | Value | Source |
|---|---|---|
| $\lvert V_{us}\rvert$ | 0.220 | [54] |
| $F$ | 93.2 MeV | [54] [55] |
| $F_K$ | 113.6 MeV | [54] [55] |
| $L_9^r$ | $6.9 \times 10^{-3}$ MeV | [56] |
| $L_{10}^r$ | $-5.5 \times 10^{-3}$ MeV | [56] |

Table 2.2: Values of constants used in the calculation of $\mathfrak{B}_{SM}(K^+ \to \mu^+\nu_\mu\mu^+\mu^-)$ as described in [10].

The contributions from virtual $\pi^+$ and $K^+$ loops are simplified and contained in the second and third term, involving the explicit sum over the two species. The values for the five parameters used in the described $\mathfrak{B}_{SM}(K^+ \to \mu^+\nu_\mu\mu^+\mu^-)$ calculation are shown in Table 2.2.

To account for the presence of two identical $\mu^+$ in the decay final state, terms originating from swapping $p_1 \leftrightarrow p_l$, i.e.

$$\begin{aligned} &q \to p_l + p_2, \\ &W \to q - p = p_\nu + p_1, \end{aligned} \tag{2.4.13}$$

are subtracted from Equation 2.4.5.

In the decay width calculation, as defined in Equation 2.4.3, the square of the amplitude takes the form

$$|A(K^+ \to \mu^+\nu\mu^+\mu^-)|^2 = \frac{1}{2}\sum_{spins}|T|^2, \tag{2.4.14}$$

where the sum runs over the allowed spin states of the four leptons and the factor 1/2 is due to two identical particles in the final state. Finally, a phase-space integral is performed numerically using a Monte-Carlo program, yielding the branching ratio expectation value of [10]

$$\mathfrak{B}_{SM}(K^+ \to \mu^+\nu\mu^+\mu^-) = 1.35 \times 10^{-8}, \tag{2.4.15}$$

with the uncertainty on the result not provided.

### 2.4.3 Muon-philic force carriers as a potential solution to the $(g-2)_\mu$ anomaly

Light weakly-coupled force extensions to the SM with carriers coupled preferentially to muons offer one of the remaining solutions to the observed muon $g-2$ anomaly, described in Section 2.2.4. This section will follow an article proposing a muon-philic force mediated by a scalar [11], which could be investigated with the NA62 $K^+ \to \mu^+\nu_\mu\mu^+\mu^-$ data set.

A general extension to the SM Lagrangian including a new scalar particle coupling to the muons, $\phi$ is

$$\mathfrak{L}_{ext} = \frac{1}{2}(\partial_\mu\phi)^2 - \frac{m_\phi^2}{2}\phi^2 - y_\phi\phi\bar{\mu}\mu, \tag{2.4.16}$$

where $m_\phi$ is the mass of the scalar and $y_\phi$ is the Yukawa coupling strength to the muon filed, $\mu$.

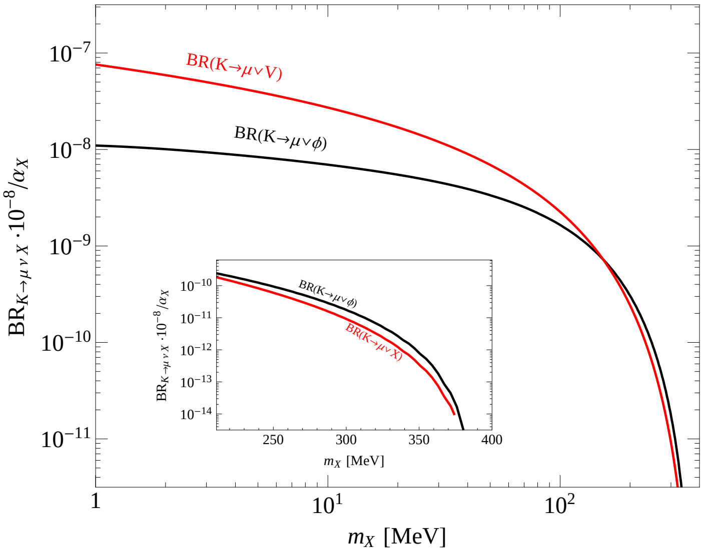

Figure 2.5: Dependence of the branching ratio of $K^+ \to \mu^+\nu_\mu X$ normalised to the coupling strength, $\alpha_\phi$, on the mass of X. The red and black lines represent vector and scalar ($\phi$) muonphilic mediators respectively. The small inset represents a region where $X \to \mu\mu$ is the dominant decay mode of the mediator. [11]

The production rate of the scalar mediator in conjunction with a $\mu^+\nu_\mu$ pair is governed by the width

$$\Gamma_{K^+\to\mu^+\nu_\mu\phi} = \frac{1}{256\pi^3 m_{K^+}^3}\int |M_\phi|^2 dm_{12}dm_{23}, \tag{2.4.17}$$

with $m_{12} = (p_\phi + p_\nu)^2$ and $m_{23} = (p_\phi + p_\mu)^2$, where $p_X$ represents the four-momentum of particle X. The squared matrix element takes the form

$$\begin{aligned}|M_\phi|^2 = \frac{\lambda_\mu^2 y_\phi^2}{2m_\mu^2(m_{23}^2 - m_\mu^2)^2}\Big[& m_K^2(m_{23}^2 + m_\mu^2)^2 \\ & - m_{23}^2\Big((m_{23}^2 + m_\mu^2)^2 + m_{12}^2(m_{23}^2 - m_\mu^2)\Big) \\ & + m_\phi^2(m_{23}^2 - m_\mu^2 m_{K^+}^2)\Big],\end{aligned} \tag{2.4.18}$$

where $\lambda_\mu = 2G_F f_K m_\mu |V_{us}| \approx 8.7\times10^{-8}$ encapsulates the relevant coupling constants as defined previously and $f_K = 160\,\mathrm{MeV}$ is the kaon decay constant. The predicted branching ratio of $K^+ \to \mu^+\nu_\mu\phi$, normalised to the coupling strength $\alpha_\phi = y_\phi^2/4\pi$, is presented as the black curve in Figure 2.5 as a function of the mass of the mediator.

The dominant decay mode of the new mediator depends on the mass of the particle. Two photons generated through a muon loop are the preferred final state for $m_\phi < 2m_\mu$, whereas for $m_\phi > 2m_\mu$, the dominant di-muon decay width can be expressed as

$$\Gamma_{\phi\to\mu^+\mu^-} = \frac{\alpha_\phi m_\phi}{2}\Big(1 - \frac{4m_\mu^2}{m_\phi^2}\Big)^{3/2}. \tag{2.4.19}$$

Given the new mediator couples exclusively with muons, the only diagram contributing to the $K^+ \to \mu^+\nu_\mu\phi(\phi \to \mu^+\mu^-)$ amplitude at leading order is that of Figure 2.6. Note that the $K^+ \to \mu^+\nu_\mu\phi$ branching ratio in the mass range dominated by the $\phi \to \mu^+\mu^-$ decay is $\lesssim 10^{-10}$ assuming $\alpha_\phi = 10^{-8}$,

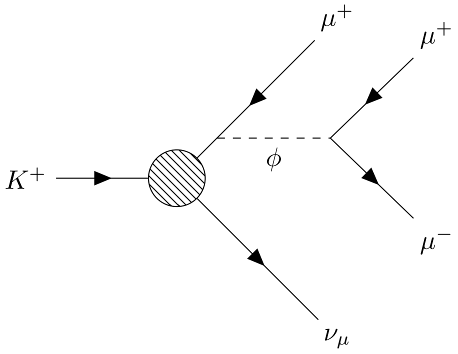

Figure 2.6: Feynman diagram for the leading contribution of a BSM scalar muon-philic force to the $K^+ \to \mu^+\nu_\mu\mu^+\mu^-$ decay.

as evident from Figure 2.5. The resulting contribution to $\mathfrak{B}(K^+ \to \mu^+\nu\mu^+\mu^-)$ would be on a sub-percent level of the SM value of Equation 2.4.15. Hence $\mathfrak{B}(K^+ \to \mu^+\nu\mu^+\mu^-)$ is not a suitable observable to investigate the presence of the muon-philic scalar mediator.

Given the low expected yield of the BSM contribution as compared to the SM rate, the search for the new physics effects should be performed as a peak search in the spectrum of the invariant mass of the $\mu^+\mu^-$ track pair, corresponding to $m_\phi$ if the correct positive muon is selected. The reach of the NA62 experiment into the $(m_\phi, \alpha_\phi)$ phase-space was estimated in [11] using the following assumptions. The accepeptance of both the BSM signal, $K^+ \to \mu^+\nu_\mu\phi(\phi \to \mu^+\mu^-)$, and SM background, the $K^+ \to \mu^+\nu_\mu\mu^+\mu^-$decay, is taken as 5%. Other background sources arising from misidentification of pions as muons and pion decays in flight are neglected due to expected sub-leading contributions. The sidebands of a particular $m_\phi$ hypothesis are used to provide a data-driven background estimate. Granularity along the scalar mass dimension is determined by the momentum resolution of the NA62 experiment, here taken as $\delta p_\mu/p_\mu = 0.4\%$ for a $p_\mu = 20\,\mathrm{GeV}/c$ muon track. Assuming statistical effects will dominate the overall uncertainty and the collection of $10^{13}$ positively charged kaon decays within the sensitive region of the NA62 detector, one obtains the $(m_\phi, \alpha_\phi)$ phase-space reach of Figure 2.7, where the $K^+ \to \mu^+\nu_\mu\mu^+\mu^-$ 90% CL exclusion contour is labelled $K \to 3\mu\not{E}$. The green band of Figure 2.7 covering the $(g-2)_\mu$-anomaly-allowed region is based on an average excluding the most recent result, with a central value consistent with Equation 2.2.4 but with significantly larger uncertainty. The inclusion of the latest measurement performed by the Muon $g-2$ Collaboration [30] would yield a band narrower by factor ~ 3 and fully contained within the one shown in Figure 2.7. The plot also includes a red line labelled $K \to \mu\not{E}$, depicting the $(m_\phi, \alpha_\phi)$ phase-space reach at 90% CL for a search involving $\phi$ decay into an invisible final state on NA62 data under assumptions detailed in Reference [11].

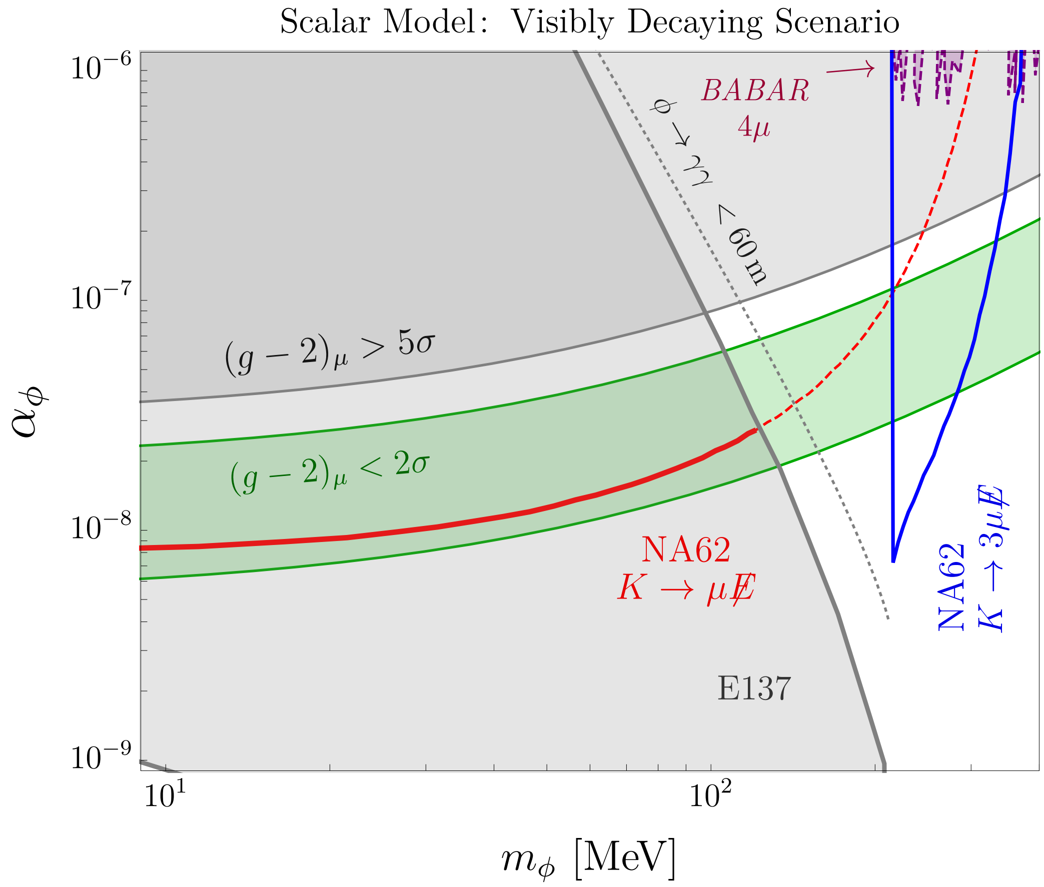

Figure 2.7: Projection of the NA62 reach into parameter space for a muon-philic scalar force mediated by a $\phi$ particle. The light green band accommodates the $(g-2)_\mu$ anomaly as measured prior to results from the Fermilab Muon $g-2$ Experiment [57]. The experimental constraints from the E137 [58] and BABAR [59] Collaborations are included. The grey dashed line denotes a limit on the lifetime of the mediator such that the particle can give an invisible signal in the NA62 apparatus. The $K \to \mu \not{E}$ red line and $K \to 3\mu \not{E}$ blue line denote the reach of searches with one and three muon tracks respectively. [11]

## Chapter 3

# The NA62 Experiment at CERN

The NA62 Experiment is located in the TCC8 and ECN3 experimental halls at the CERN North Area, as shown in Figure 3.1. The experiment was conceived with the aim of measuring the very rare charged kaon decay $K^+ \to \pi^+\nu\bar{\nu}$ to a 10% relative precision, using a kaon decay-in-flight technique and protons delivered by CERN's Super Proton Synchrotron (SPS).

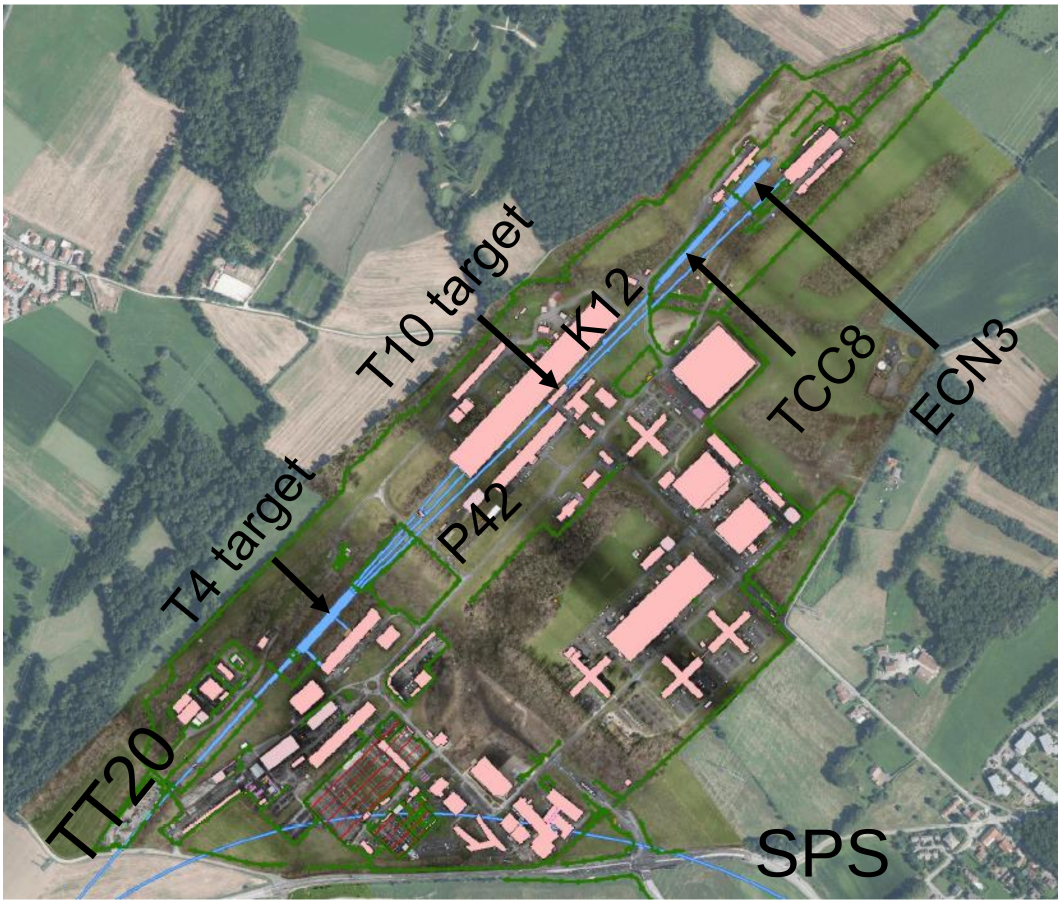

Figure 3.1: Aerial view of the CERN Prevessin site, known as the North Area, produced with the CERN Geographic Information System [60]. CERN overground buildings are marked in pink, with underground tunnels and caverns in blue. Elements of the particle delivery system to the NA62 Experiment (accelerators, transfer lines, targets) and the experimental caverns used by NA62 are marked in black.

| Final state | BR[%] | Suppression mechanism |
|---|---|---|
| $\mu^+\nu_\mu$ | $63.56 \pm 0.11$ | PID & kinematics |
| $\pi^+\pi^0$ | $20.67 \pm 0.08$ | Photon veto & kinematics |
| $\pi^+\pi^+\pi^-$ | $5.583 \pm 0.024$ | Track multiplcity & kinematics |
| $\pi^0 e^+\nu_e$ | $5.07 \pm 0.04$ | PID & photon veto |
| $\pi^0\mu^+\nu_\mu$ | $3.352 \pm 0.033$ | PID & photon veto |
| $\pi^+\pi^0\pi^0$ | $1.760 \pm 0.023$ | Photon veto & kinematics |

Table 3.1: Six main decay modes of the positively charged kaon together with their branching ratios and strategies for their suppression within the NA62 Experiment. Numerical values taken from [13].

The beam line and detector of NA62 were designed together to enable the measurement given the elusive nature of the decay in question, with only a positively charged pion track in the final state and missing energy-momentum to account for the presence of the neutrino-anti-neutrino pair. Such a signature can be obtained from any charged kaon decay involving a positive pion in the event of the other daughter particles escaping detection, as well as through a similar mechanism with additional misidentification of a positive muon or positron as a pion. All of the six main decay modes of the $K^+$, listed in Table 3.1, are potential sources of background for the $K^+ \to \pi^+\nu\bar{\nu}$ channel. Mitigating significant background contamination necessitates excellent kinematic resolution for both parent kaon and daughter particles, efficient particle identification (PID) and a hermetic photon veto to suppress the $K^+ \to \pi^+\pi^0(\pi^0 \to \gamma\gamma)$ process. Target precision of the $K^+ \to \pi^+\nu\bar{\nu}$ measurement and the SM prediction for branching ration of the signal mode being $O(10^{-10})$ require the collection of $O(10^{13})$ kaon decays within the acceptance of the detector. To achieve this goal on a few years' timescale, delivering a beam of high intensity is necessary. Consequently, timing resolution of $O(100\,\mathrm{ps})$ and high trigger efficiency were added to the design requirements.

The NA62 Experiment collected $K^+ \to \pi^+\nu\bar{\nu}$ data in 2016, 2017 and 2018, jointly referred to as Run1. Data-taking recommenced in 2021 and is planned to last until at least 2025, with this second period referred to as Run2.

To fulfill the technical requirements, the approaches described further in this chapter were adapted, with beam line specifications followed by details of the detector design, then trigger and data acquisition (TDAQ) system, as implmented for Run1. The chapter concludes with an overview of the NA62 software framework, used for simulation, data reconstruction and analysis, together with the methodology and an up-to-date result of the $K^+ \to \pi^+\nu\bar{\nu}$ analysis.

## 3.1 Beam line

To produce an intense hadron beam containing charged kaons, the NA62 Experiment relies on the CERN accelerator complex for the delivery of protons. The protons are extracted from the SPS in $\sim$3 s spills, each delivering $\sim 3.3 \times 10^{12}$ protons, transferred through the TT20 line, diverted through the T4 target, and propagated through the P42 line, all shown in Figure 3.1. The 400 GeV protons then impinge on the T10 target, a beryllium cylinder of 2 mm diameter and 400 mm length, to produce a secondary hadron beam named K12, which passes through experimental halls TCC8 and ECN3 of the North Area [61]. The target material, together with the central momentum of 75 GeV/$c$ of the secondary beam were chosen to maximise the production of kaons with respect to protons and other

| Particle species | $p$ | $K^+$ | $\pi^+$ | $\mu^+$ | Total |
|---|---|---|---|---|---|
| Beam fraction [%] | 23 | 6 | 70 | <1 | 100 |
| Instantaneous intensity [MHz] | 175 | 45 | 525 | $\approx 5$ | 750 |

Table 3.2: Beam composition and instantaneous particle rates per species at nominal intensity of the K12 beam line. Values taken from [62].

hadron components, as shown in Table 3.2 including nominal instantaneous particle rates.

The experimental right-handed coordinate system is defined by the direction of the beam, taken as the z-axis so that particles travel in the positive z-direction, and the vertical y-axis pointing upwards. The position of the T10 target serves as the origin of the experimental coordinate system.

The secondary hadron beam propagates through the beam line shown in Figure 3.2, with the conventional division into upstream and downstream parts delimited by the position of the third station of the GigaTracker, i.e. 102.4 m downstream of the T10 target. The beam initially passes through a large-acceptance copper collimator, then is focused in the $(x, y)$ plane by three quadrupole magnets (Q1, Q2, Q3). Subsequently, secondary hadrons encounter the first achromat (A1), composed of four dipole magnets and responsible for selecting the central momentum of 75 GeV/$c$ with a 1% root-mean-square (RMS) acceptance. The first two magnets displace the beam along the horizontal direction. The beam then propagates through graduated holes of a set of two movable beam-dump units (TAX1 and TAX2), used to absorb particles outside the desired momentum and direction range. Between the two units, a set of tungsten plates of total length of 50 mm is inserted, with the depth optimised to allow maximal positron energy loss from bremsstrahlung while minimising hadron scattering. The first achromat concludes with two dipole magnets, returning the centre of the beam to its original direction along the z-axis. The beam is then re-focused and collimated in both x and y directions by a set of quadrupole magnets interspersed with collimators, removing the remainder of particles scattered by the tungsten plates. Secondary particles pass through a set of dipole magnets, labelled B3 in Figure 3.2, which impart a vertical magnetic field causing the de-focused positive and negative muons to be swept away. The correction for a potential deviation due to the muon sweepers is provided by a pair of dipole magnets (TRIM2 and TRIM3).

The beam particles are then prepared for entry into the first detector system, the KTAG, located about 70 m downstream of the T10 target. Parallelisation of beam hadrons and minimising their radial dispersion is handled by a pair of quadrupole magnets (Q7, Q8) followed by two collimators (C4, C5). Two pairs of filament scintillator counters (FISCs), one oriented along the x and the other along the y directions, enable the measurement of transverse beam profiles. One module of each pair is positioned in front of and the other behind the KTAG, with the FISCs used both for beam tuning and quality monitoring during data-taking.

Subsequently, beam particles are focused one final time by a pair of quadrupole magnets (Q9, Q10), before entering the second achromat (A2) housing the three-station magnetic beam spectrometer, the GigaTracker (GTK). The achromat is composed of four dipole magnets, with the first pair imparting a vertical parallel displacement of −60 mm and the other returning the beam to the original direction. Between the two magnet pairs, the particles encounter a toroidally magnetized iron collimator, known as a scraper magnet (SCR1), responsible for defocusing and removing the muon beam

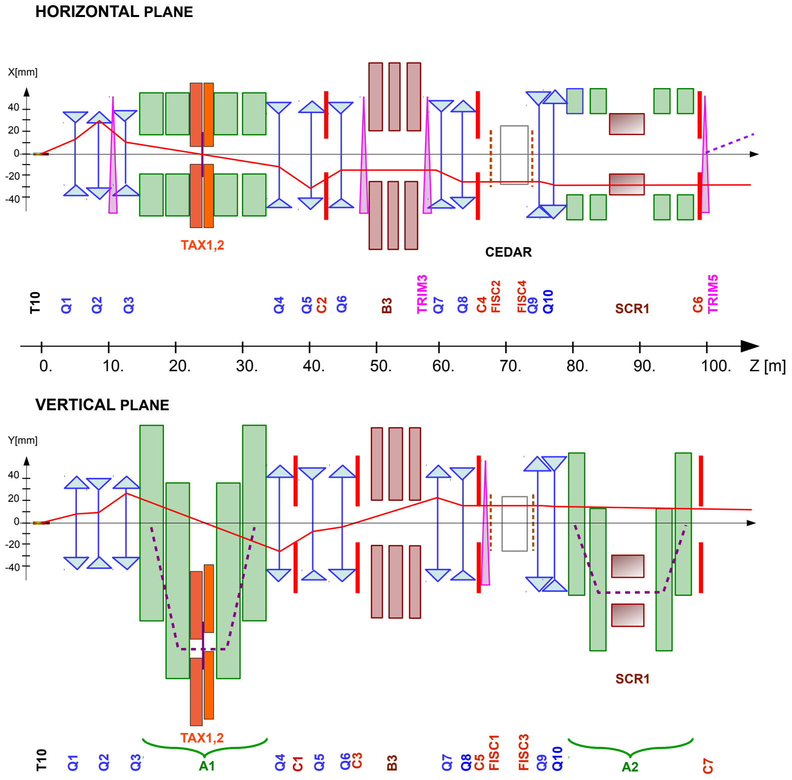

(a) Vertical and horizontal views of the upstream section of the K12 beam line, spanning the T10 target to the TRIM5 magnet. Trajectory of a beam particle emitted from the T10 target along in the positive z-direction is shown as the dashed line. The red line marks the trajectory of a secondary hadron emitted from the target at the indicated angle.

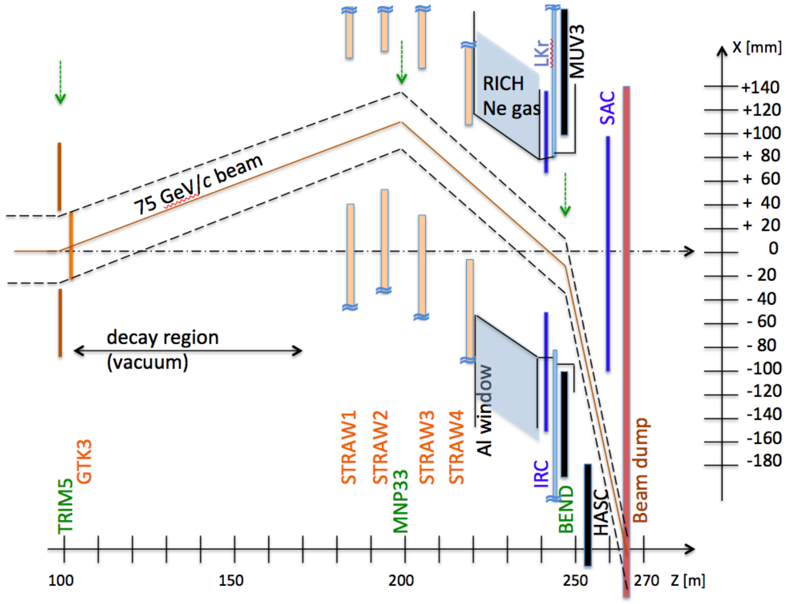

(b) Horizontal view of the downstream section of the K12 beam line, spanning the TRIM5 magnet to the beam dump. The solid yellow line denotes the nominal trajectory of the K12 beam, with the dashed lines marking the width of the beam profile.

Figure 3.2: Schematics of the K12 beam line, containing the secondary hadron beam used by the NA62 experiment. The detector and beam line components are labelled. [62]

component. After exiting the achromat, the beam is subject to the effects of the last two collimators (C6, C7), defining the final angular acceptance of the beam and discarding any particles outside of it, such as products of upstream decays. During the 2018 data-taking campaign, a fixed iron collimator (TCX) replaced C6 and C7, offering improved suppression of particles originating from decays in the upstream region, owing to its significantly larger transverse size and depth.

The beam particles are then subject to a deflection originating from a dipole magnet (TRIM5) positioned immediately downstream of the last GTK station. The $90\,\mathrm{MeV}/c$ magnetic kick to $75\,\mathrm{GeV}/c$ particles results in a $1.2\,\mathrm{mrad}$ deflection in the x-plane, with the beam entering a long vacuum tank housing the fiducial region for kaon decays (later referred to as FV). In the downstream section of the beam line, as shown in Figure 3.2b), beam components travel in a straight line and through the central holes of the first two downstream spectrometer stations (STRAW1, STRAW2). The particles are subject to a $270\,\mathrm{MeV}/c$ magnetic kick from the MNP33 magnet, resulting in a deflection of $-3.6\,\mathrm{mrad}$ in the $(x, z)$ plane countering the effect of the TRIM5 magnet. The beam then continues past the central holes of the final two spectrometer stations (STRAW3, STRAW4). The MNP33 deflection results in beam particles hitting the centre of the $(x, y)$ plane at a z-position $2.8\,\mathrm{m}$ downstream of the front face of the electromagnetic calorimeter, the LKr.

The large vacuum tank housing the FV and the downstream spectrometer terminates behind STRAW4, with the beam particles crossing a thin aluminum window and entering an evacuated beam pipe, which allows them to pass through the centres of the downstream detector systems. The beam pipe closely follows the direction of the beam, accounting for its divergence, and minimises the amount of downstream detector signals originating from beam components. Two FISCs are present at the point where the beam crosses the z-axis, verifying its shape before a final magnetic deflection. The magnetic kick is provided by a dipole magnet (BEND) and directs the beam at $-13.2\,\mathrm{mrad}$ in the $(x, z)$ plane, towards the beam dump. Before being absorbed by the iron dump surrounded by concrete, beam components exit the evacuated beam pipe and pass through a wire chamber with analogue readout and an ionisation chamber. These two instruments allow a final measurement of the beam profile and a live per-spill monitoring of the number of protons delivered on the T10 target.

## 3.2 Detector

The detector of the NA62 Experiment aims to enable a decay-in-flight measurement of the $K^+ \to \pi^+ \nu \bar{\nu}$ decay, with the general requirements outlined in the beginning of this chapter. The elusive nature of the signal mode and the high beam intensity, leading to a high detector rates, require precise quantitative descriptions of both the parent kaon and the daughter pion, together with a hermetic veto for photons and high efficiency of detection of any additional charged particles. Beam particle momenta and directions are measured by the upstream spectrometer, the GTK, with the kaon indentified and timestamped by the KTAG system. All the remaining detector systems of the NA62 detector, as shown in Figure 3.3, are designed to identify and quantify signal from decays originating in the FV and other particles arriving from the upstream.

This section describes the detector systems of NA62 in their Run1 configurations, with more detail available in reference [62]. Systems pertinent to the $K^+ \to \mu^+ \nu_\mu \mu^+ \mu^-$ analysis are covered in greater detail.

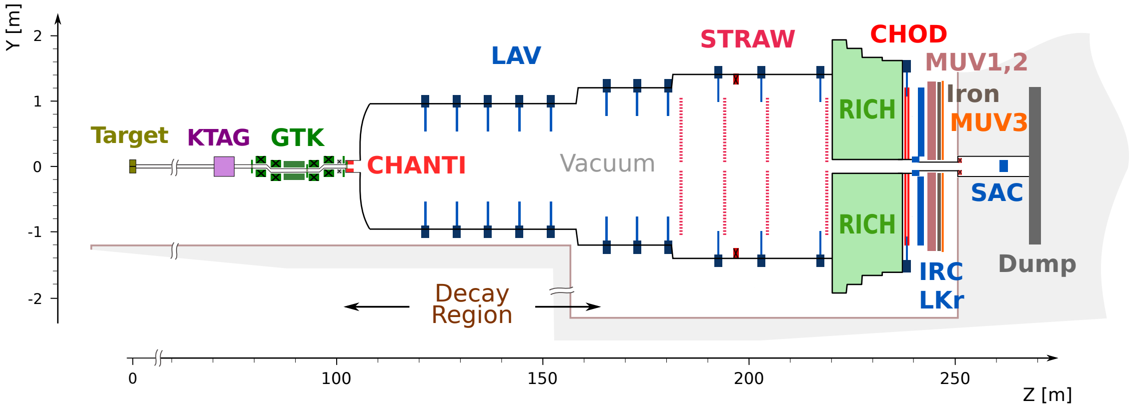

Figure 3.3: Schematic of the NA62 detector in its 2017 and early 2018 configuration, as viewed from the side. The object labelled "CHOD" describes the position of both NA48-CHOD and CHOD. [62]

### 3.2.1 KTAG

The unseparated hadron beam of NA62 contains only 6% of positively charged kaons. To enable the measurement of their decays, in particular matching the upstream spectrometer tracks produced by all charged beam particles to downstream signatures, and reject beam particle interactions with vacuum tank gas, the kaon crossing time must be obtained with a precision of 100 ps. This task is performed by a differential Cherenkov detector with a bespoke photon readout system, the KTAG. The system is designed to minimise material thickness in the path of the beam, which defines the amount of scattering due to the detector, maximise the efficiency of kaon detection and ensure a small contamination arising from beam pions. To satisfy the requirements at the expected 45 MHz kaon rate, a standard nitrogen-filled ChErenkov Differential counter with Achromatic Ring focus (CEDAR) [63], designed for identification of high energy particles in secondary SPS beams, was complemented with a state-of-the-art purpose-built photon readout [64].

Differential Cherenkov counters exploit the Cherenkov effect, where charged particles travelling through a medium at a speed larger than the speed of light in that medium emit photons at an angle $\theta_C$ with respect to their direction. For particles of velocity $v = \beta c$, photons can be focused on a plane with an effective focal length $f$, leading to a light ring of radius

$$R_C = f \times \theta_C = f \times \cos^{-1}\left(\frac{1}{n\beta}\right), \tag{3.2.1}$$

with $n$ being the refractive index of the medium. In CEDARs, the radius at which photons are extracted from the vessel through eight quartz windows, as shown in the light propagation schematic of Figure 3.4, is fixed. Given the fixed central momentum of the beam, $p$, a particle species of mass $m$ is characterised by a velocity

$$\beta = \left(1 + \frac{m^2}{p^2}\right)^{-1/2}. \tag{3.2.2}$$

The desired species, i.e. kaons, can be selected by choice of gas medium and number density, $\rho$ defining the refractive index, with the dependence

$$(n-1) \propto \rho \propto P/T, \tag{3.2.3}$$

where $P$ and $T$ are the pressure and temperature of a gas contained in a fixed volume.

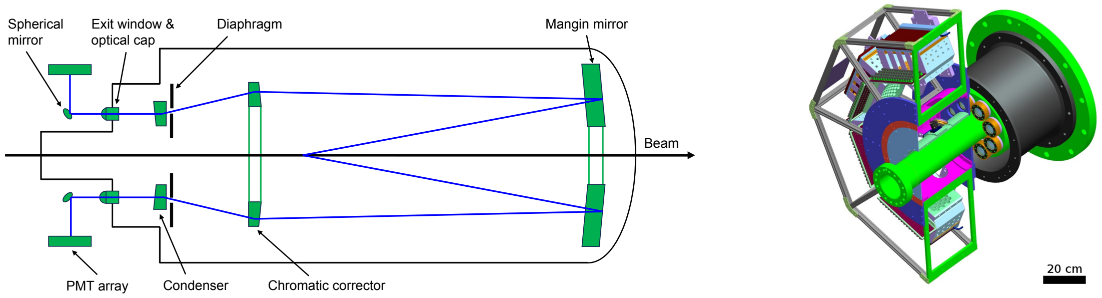

Figure 3.4: Left: Schematic diagram of light propagation in the CEDAR vessel. [65] Right: Mechanical design showing one half of the KTAG detector readout module. [64]

In a CEDAR vessel, well insulated by design, the refractive index is hence determined by the gas pressure. The NA62 CEDAR was filled nitrogen at pressure of 1.73 bar during Run1.

To minimise pion contamination of the kaon signal, with radial separation $\delta R(K-\pi) \approx 2\,\mathrm{mm}$, the width of the transmitted light ring can be constrained by using a motorised diaphragm. The width of the light ring is dominated by beam divergence, with a significant contribution from chromatic dispersion and minor ones from scattering and refractive index inhomogeneity [63]. The impact of the first phenomenon is mitigated by precise beam steering to achieve <100 mrad divergence and detector alignment using a pair motors, independently parallelising the optical axis in the $(x, z)$ and $(y, z)$ planes. Chromatic dispersion is tackled by the usage of correctors fixed inside the CEDAR vessel, as shown in Figure 3.4. Overall, the individual light ring width is kept well below the kaon-pion radial separation, with the diaphragm operated at an aperture of ∼1.5 mm.

After exiting the CEDAR vessel through one of the eight thin, uniformly spaced quarts windows, the photons are reflected radially outwards by a spherical mirror towards a light box, as shown in Figure 3.4. Each of the eight light boxes, often referred to as sectors or octants, consists of an aluminum plate with cone-section-shaped and Mylar-lined holes leading to 48 photomultipliers(PMs), with the single channel resolution of $\sigma_t(PMT) = 300\,\mathrm{ps}$. The large number of PMs per octant was chosen to achieve the required time resolution of <100 ps, since a kaon crossing time resolution, $\sigma_t(KTAG)$ is taken as the average of over $N_\gamma$ detected photons, so that

$$\sigma_t(KTAG) = \sigma_t(PMT)/\sqrt{N_\gamma}. \tag{3.2.4}$$

A more detailed description of the light box geometry is available in [64].

The KTAG performance in NA62 Run1 was characterised by observing an average of 20 Cherenkov photons per kaon candidate, i.e. one constructed from coincident signals in at least five octants of the detector. The time resolution of the detector in that period can hence be calculated from Equation 3.2.4 as ∼70 ps. The average efficiency of kaon identification in Run1 is 98%.

### 3.2.2 Beam spectrometer - GTK

The Gigatracker (GTK) is a beam spectrometer positioned around the A2 magnetic achromat of the K12 beam line inside the evacuated beam pipe [66]. In the Run1 configuration, it consists of three stations, with the layout presented in Figure 3.5: GTK1 before the first dipole magnet pair, GTK2 in

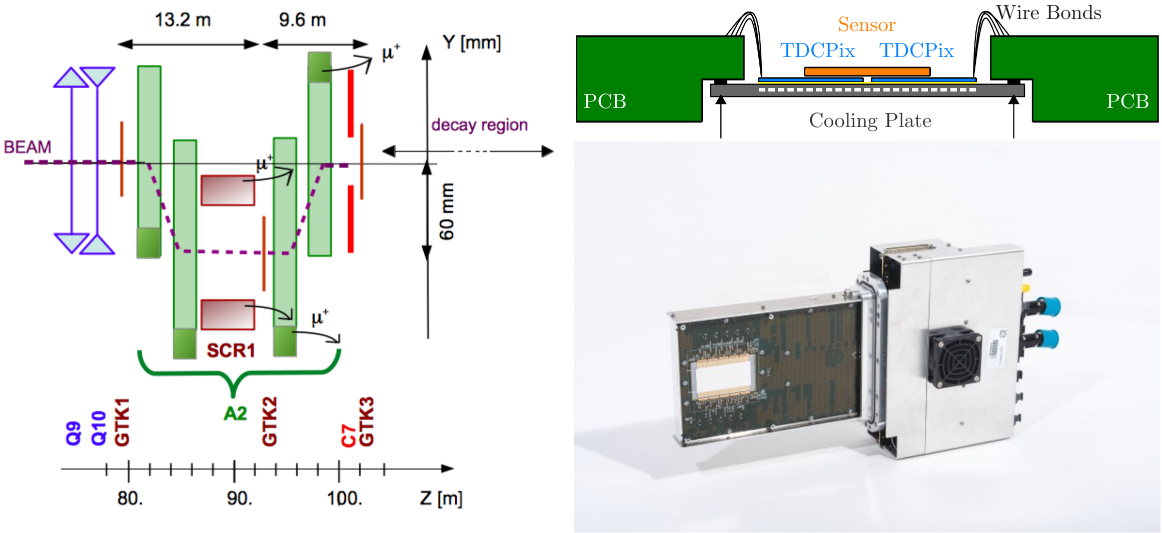

Figure 3.5: Left: Schematic of the GTK beam spectrometer. The dashed line follows the trajectory of a K12 beam particle travelling at the central momentum of 75 GeV/$c$ from left to right. Right top: Sketch of a single GTK station. The beam would traverse the module from top to bottom. Right bottom: picture of a fully assembled GTK station, viewed from the sensor side. [62]

the section where the beam particles travel at a vertical displacement of $-60$ mm and GTK3 downstream of the achromat and the following TRIM5 kicker magnet. Precise measurement of positions at each of the three stations allows to reconstruct the beam particle momentum magnitudes under the magnetic deflection, as well as their direction.

Recording signal from all charged hadron beam components, the GTK is exposed to the highest hit rate of all the NA62 detector systems (up to 1.5 MHz/mm$^2$ [66]), necessitating excellent time resolution and radiation hardness. To achieve these goals, hybrid silicon pixel technology was employed, each station comprising of a sensor, on-detector read-out and cooling layers in the path of the beam, see Figure 3.5. The cooling system, maintaining the modules at $-15\,^\circ$C, was designed to allow continuous operation of the detector under full intensity for 100 days without significant performance loss [67]. The design thickness of a single station under 0.5% $X_0$, with the sensor layer only 200 µm thick, was chosen to minimise both multiple Coulomb scattering of beam particles interacting with the detector and the amount of background from interactions in GTK3.

To achieve a target momentum resolution of $\sigma_p/p = 0.2\%$ given the vertical spatial dispersion of the beam of 0.6 mm at GTK2, a $300 \times 300\,\mu\text{m}^2$ pixel size was chosen. A matrix of $40 \times 45$ pixels is read out by an application-specific integrated circuit (ASIC) [68], with two rows of five such modules comprising a single station of active area $62.8 \times 27\,\text{mm}^2$. The detector geometry provides a 0.16 µrad angular resolution in the $(x, z)$ and $(y, z)$ planes. The usage of a time-over-threshold technique with multiple corrections, including the effects of time-walk, gives a single pixel time resolution of 150 ps.

### 3.2.3 CHANTI

The CHarged ANTI-coincidence detector (CHANTI) [69] is positioned just downstream of the final GTK station and was designed to detect charged particles scattering in GTK3, also being sensitive to upstream kaon decays and beam halo muons originating from the K12 beam line. It comprises six stations housed in a vacuum vessel shared with GTK3, with the spacing approximately doubling

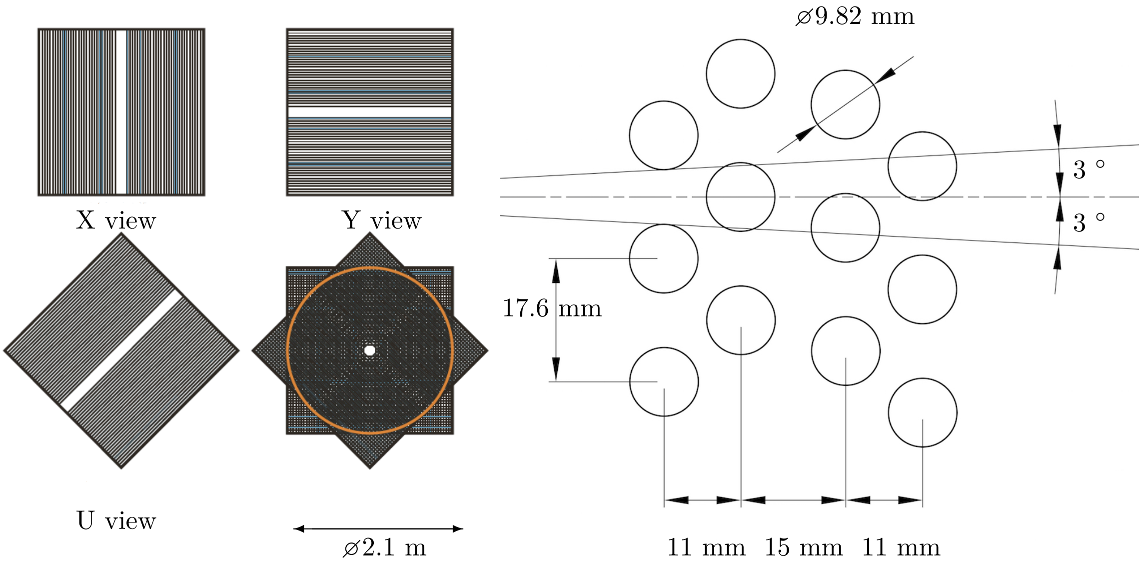

Figure 3.6: Left: Three of the four views, i.e. layers of equally-oriented straws, present in a single STRAW detector station. A superposition of the four views gives hermetic coverage spanning a 2.1 m circle with a beam-hole in the middle for a free passage of the beam. Right: Positioning of straw tubes within a single STRAW detector view optimised to ensure sufficient overlap for a particle to cross at least two straws. [62]

between subsequent module pairs. Two orthogonally-oriented layers of scintillator bars of area $300 \times 300\,\mathrm{mm}^2$ with a beam hole in the middle make up a single station. This geometry allows for a hermetic coverage in the angular range of 49 mrad to 1.34 rad. The scintillator bars are of triangular shape, 3.3 cm wide at the base with a central wavelength-shifting optical fibre propagating the light signal to a silicon photo-multiplier (SiPM) for each bar. The detector system was measured to be 99% efficient [69], with the observed position and time resolutions of ~2.5 mm and ~0.8 ns [62], respectively, critical for space-time matching and minimisation of the impact of accidental activity.

### 3.2.4 STRAW

The STRAW is a magnetic spectrometer designed to measure momenta and directions of decay products of the K12 kaons. The spectrometer consists of four stations, two placed in front of and two downstream of the MNP33 magnet, as shown in Figures 3.2 and 3.3. An integrated magnetic field of 0.9 T m supplies a deflection which allows for a measurement of momentum. To satisfy the low scattering and precision requirements, the chosen approach was a bespoke system of thin gas-filled straw tubes inserted directly into the main vacuum vessel of NA62, immediately downstream of the target kaon decay region. Each station is composed of four views of 2160 mm-long and 9.8 mm-diameter straws, aligned orthogonally in pairs in $(X, Y)$ and $(U, V)$ directions, with the latter rotated by 45° with respect to the experimental coordinate system, see Figure 3.6. Central straws from each view are removed to allow for the passage of the undecayed beam particles, as visible in Figure 3.2. Tracks produced in kaon decays in the generalised NA62 acceptance will span the angular range ±3°, motivating the relative staggering of the two pairs of tube layers within a view. Such redundancy guarantees at least two straw crossings per charged particle track in each view, as shown in Figure 3.6.

A single straw tube is made of a thin layer of polyethylene terephthalate (PET), covered by 50 nm of copper and 20 nm of gold on the inside. The tubes are filled with a gas mixture composed of 70%

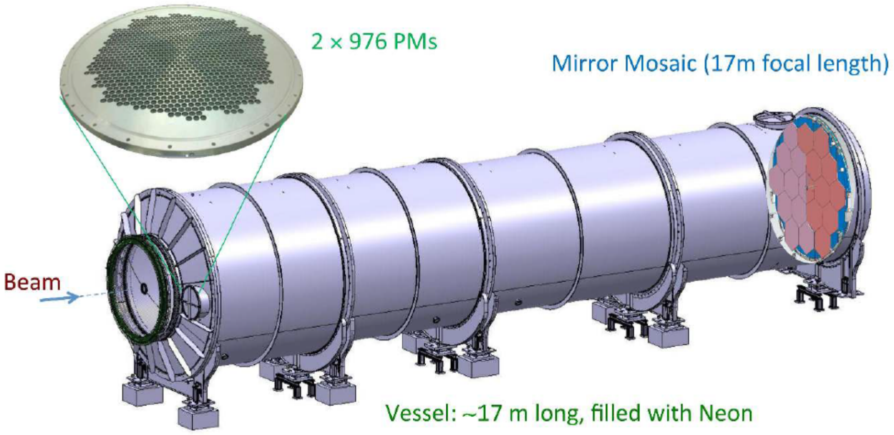

Figure 3.7: Schematic view of the RICH detector vessel, with indicated beam direction, layout of the mirror mosaic at the downstream end and photo-multiplier arrays on the upstream flange. [62]

argon and 30% $CO_2$, and contain a 30 µm thick tungsten anode wire running on the symmetry axis of the cylinder. A charged particle passing through a tube creates electron-ion pairs. The duration of the electrical pulse generated on the anode defines the distance of particle impact point from the central wire, further improving the point position resolution. Small dimensions of individual straws allow to achieve a light system, totalling 1.8% $X_0$.

The novel design allowed to achieve the target momentum resolution of the spectrometer of

$$\frac{\sigma_p}{p} = 0.30\% \oplus 0.005\% \times p, \qquad (3.2.5)$$

where the particle momentum, $p$ has units of GeV/$c$. The one-dimensional angular resolution of the system decreases from 60 µrad at 10 GeV/$c$ to 20 µrad at 50 GeV/$c$.

### 3.2.5 RICH

The Ring Imaging CHerenkov (RICH) detector of NA62 was designed to allow for pion and muon separation in the (15 to 35) GeV/$c$ momentum range, as necessary for the $K^+ \to \pi^+\nu\bar{\nu}$ analysis. Furthermore, the system was required to provide a sub-100 ps timing information, compatible with the performance of the upstream KTAG-GTK system.

The target Cherenkov threshold for the detector was set for a 12.5 GeV/$c$ pion to ensure full efficiency at the lower momentum limit, leading to the required refractive index $n$ such that $(n-1) = 62 \times 10^{-6}$. This motivated the choice of neon as the radiative medium, as it nearly exactly matches the requirement at room temperature and atmospheric pressure. The RICH vessel, a 17 m long cylinder with diameter decreasing from 4.2 m upstream to 3.2 m downstream, is located downstream of the NA62 vacuum tank. A thin evacuated aluminum tube running along the centre of the vessel separates the beam from the active detector area. Cherenkov photons from charged kaon daughters with momentum exceeding the detector threshold are incident on the downstream end, housing an array of spherical mirrors, shown in Figure 3.7. The array consists of 18 hexagonal and 2 half-hexagonal mirrors of 350 mm side, separated along the vertical into two groups reflecting the light to the left and right of the active area respectively. The orientation of each mirror is controlled though a pair of remotely-controlled piezoelectric actuators, allowing for quick alignment to validate detector per-

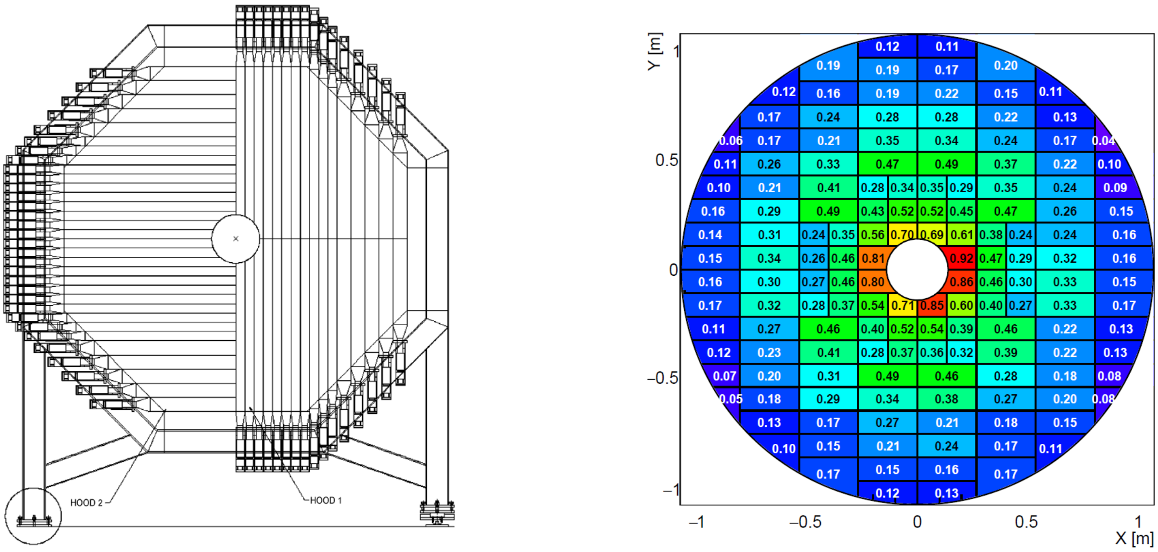

Figure 3.8: Left: Schematic of the NA48-CHOD, showing the two orthogonally-aligned layers of scintillator slabs, with readout photo-multiplier tubes at their ends and the support structure. Right: tile layout and per-tile hit rate in MHz at nominal NA62 intensity for the CHOD. [62]

formance. The photons travel upstream, towards two arrays of PMs situated symmetrically on the outer flange of the upstream end of the vessel. The granularity of the readout assemblies significantly contributes to the angular resolution of the detector. 976 PMs per array were instrumented, with the active area enhanced through the use of Mylar-covered Winston Cones [70].

The detector performance was measured on 2017 data yielding a pion identification efficiency of 83% and a muon contamination of 0.2% [71]. A sample of $K \to \pi^0 e^+ \nu_e$ events from 2017 data was used to quantify the RICH timing resolution as 70 ps [72].

### 3.2.6 Charged particle hodoscopes

The NA62 experiment uses two independent scintillator detector systems positioned between the RICH and LKr, the NA48-CHOD inherited from the NA48 experiment [73], and the CHOD custom-built for NA62. Both detectors are used primarily for the provision of fast information on the presence of charged particles in the radial range (145 to 1070) mm downstream of the RICH for triggering purposes, with the lower and upper limits defined by the shapes of the IRC calorimeter and the LAV12 station respectively (see Section 3.2.8). The hodoscopes provide timing information for charged particles of all momenta, serving as the only timing system for particle outside the RICH operational range. Both detectors have a central hole, allowing the beam pipe to transmit the undecayed K12 beam components without interactions.

#### 3.2.6.1 NA48-CHOD

The NA48-CHOD is placed between the RICH and the LAV12 station. It consists of two diagonally-oriented layers of 20 mm thick scintillator slabs made of BC408, with the material choice motivated by a fast decay time. The slabs vary in both length and width, ranging from $65 \times 1210\,\mathrm{mm}^2$ for the innermost, to $99 \times 600\,\mathrm{mm}^2$ for the outermost, as shown in Figure 3.8. Light generated by charged particles passing through the NA48-CHOD is collected by photo-multiplier tubes (PMTs), one at the outer end of each slab, optically connected by a Plexiglas light guide. The position of the particle impact point is obtained from the coincidence of signal in the vertical and horizontal layers, with the two layer system helping to suppress noise and back-scatter from the LKr calorimeter. The NA48-CHOD is read out with time-over-threshold discriminators developed for the LAV detector, achieving a single-particle time resolution of ∼200 ps [62]. The total system thickness is 0.10 $X_0$.

#### 3.2.6.2 CHOD

The other charged particle hodoscope of NA62, the CHOD, is positioned between the LAV12 and the LKr calorimeter. It comprises 152 scintillator tiles of 108 mm height and 30 mm depth. The tiles are vertically spaced by 107 mm, possible thanks to placing alternating rows on opposite sides of a thin (3 mm) central support foil. The resultant 1 mm vertical overlap minimises inefficiency caused by particles crossing at tile edges. The tiles have two base widths: 134 and 268 mm, with the former for instrumenting the higher rate area closer to the beam and edge tiles shaped to extend exactly to an outer radius of 1070 mm. The geometry is a result of optimisation of single tile rates, with the layout and expected rates in MHz at nominal NA62 intensity shown in the right panel of Figure 3.8. Each tile is read out by a pair of silicon PMs, optical contact with the scintillator material provided by wavelength-shifting fibers, with outputs further shaped by constant fraction discriminators (CFDs) [74] for improved trigger time resolution. The efficiency of the CHOD was measured on 2016 data as 98.6%, with a single-particle time resolution of 1.01 ns [75].

### 3.2.7 Liquid krypton calorimeter - LKr

The main electromagnetic calorimeter used in the NA62 setup is the Liquid Krypton calorimeter (LKr) inherited from the NA48 experiment [73]. It serves two main purposes: providing a photon veto in the intermediate forward radial region, as defined with respect to the z-axis, and allowing for particle identification in conjunction with kinematic information from the STRAW spectrometer. To cope with the high particle rate in NA62, a new readout system was designed for the LKr [76].

The calorimeter is a quasi-homogeneous ionization chamber, filled with liquid krypton kept at 120 K by a purpose-built cryogenic system. The active material was chosen for radiation hardness, with a filtration plant allowing for purity tests being a part of the cryogenic setup. The calorimeter vessel has an octagonal front face, covering the area of a circle of 1280 mm radius, with a central hole accommodating the beam pipe. The vessel has a depth of 1.27 m, corresponding to 27 $X_0$, chosen to ensure full containment (>99%) of electromagnetic showers up to 50 GeV. Readout is provided through a set of thin Cu-Be electrodes of 20 mm width and 1.27 m length. The lateral spacing between individual ribbons is 10 mm, as shown in Figure 3.9, leading to a cell transverse size of $20 \times 20\,\mathrm{mm}^2$. Such high granularity allows for good position resolution of energy deposits, given the active medium Moliere radius of 47 mm.

The expected energy resolution of the LKr in the NA62 configuration based on simulation is [62]

$$\frac{\sigma_E}{E} = \frac{4.8\%}{\sqrt{E}} \oplus \frac{11\%}{E} \oplus 0.9\%, \tag{3.2.6}$$

with a slight deterioration as compared to the performance within the NA48 experiment [78] arising from additional upstream material and a higher detector rate. The detector photon-veto capability satisfies the NA62 requirements of $10^{-3}$ at $E_\gamma$>1 GeV and $10^{-5}$ at $E_\gamma$>10 GeV [62].

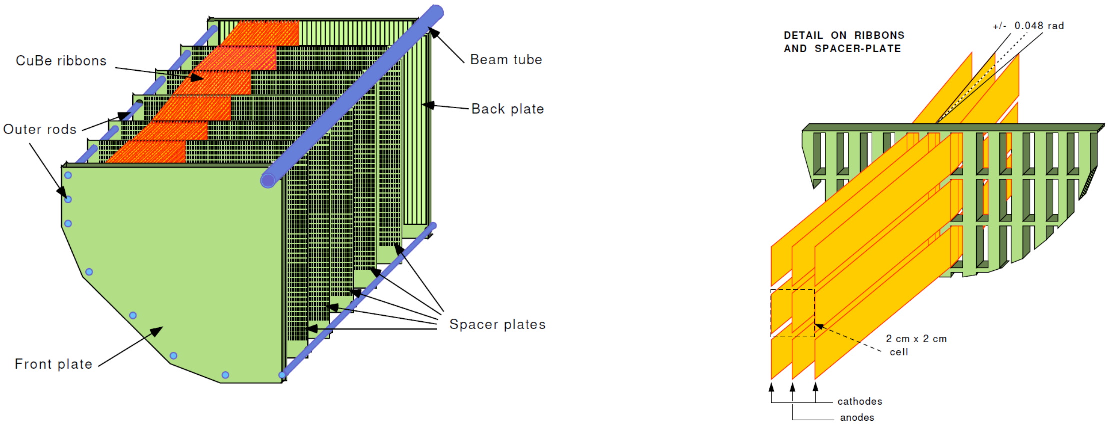

Figure 3.9: Left: schematic view of a quarter of the LKr calorimeter. Right: detail of the calorimeter cell structure. [77]

### 3.2.8 Other photon vetoes

The photon-veto requirements of NA62 are defined by the elusive experimental signature of the $K^+ \to \pi^+\nu\bar{\nu}$ decay, in particular the fact that the $K^+ \to \pi^+\pi^0(\pi^0 \to \gamma\gamma)$ process can mimic the signal mode should the photons go undetected. To enable the decay-in-flight measurement, a hermetic photon veto covering the angular range (0 to 50) mrad is achieved by employing four different calorimetric systems, as outlined in Table 3.3.

#### 3.2.8.1 Large Angle Veto - LAV

The Large Angle Veto (LAV) system [79] is designed to veto photons emitted at an angles of (8.5 to 50) mrad from the z-axis and consists of 11 stations (LAV1- LAV11) operating in the vacuum tank housing the decay volume and a single station (LAV12) placed between the two charged particle hodoscopes. As shown in Figure 3.3, the active area of each station is a ring in the $(x, y)$ plane, with a fixed radial length but varying inner radii and thicknesses. Given the low energy of photons from $\pi^0$ decays emitted at angles covered by the LAV, the detector must have an inefficiency of $< 10^{-4}$ for $E_\gamma$>200 MeV. The large transverse size of the detector active area and the station positions make it sensitive to beam halo particles, i.e. ones originating from the upstream area but not the K12 beam. To ensure the halo particles do not contribute through accidentals, a time resolution of $\sim$1 ns is required.

At the stage of designing the NA62 detector, modules from the barrel of the electromagnetic calorimeter of the OPAL experiment [80] became available for recycling. Upon testing, they were observed to satisfy the performance requirements, offering substantial savings on construction costs. The individual modules are lead-glass blocks, with 75% of PbO, 370 mm long and of square cross

| Coverage [mrad] | Detector name | Modules |
|---|---|---|
| 8.5 - 50 | LAV | 12 |
| 1.0 - 8.5 | LKr | 1 |
| 0 - 1 | SAV | SAC + IRC |

Table 3.3: The NA62 photon veto systems, with their radial coverage and number of modules.

(a) First LAV station.

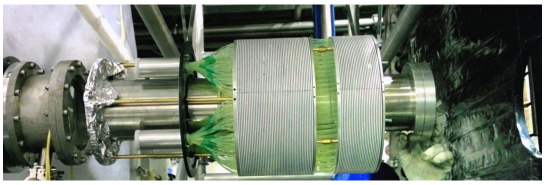

(b) IRC installed on the K12 beam line.

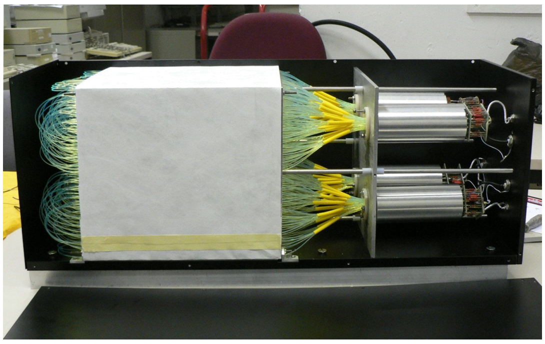

(c) SAC before installation.

Figure 3.10: Pictures of the LAV1 station, IRC and SAC detectors. [62]

section varying from $100 \times 100$ to $110 \times 110\,\mathrm{mm}^2$ on opposite ends. Electromagnetic showers induced in the glass are detected from the Cherenkov light generated by their charged components. Each block is read out by a single large-diameter PM, optically connected to the larger-area end by a light guide. Each station comprises a few layers of rings of lead-glass blocks, with the PMs facing outward, as shown in Figure 3.10 a). As the ring radius increases, the spacing between the wider ends of the blocks reduces, which together with the staggered ring layout allows for fewer layers to achieve the same effective depth for stations further downstream. The geometry results in most incident particles traversing at least $27\,X_0$ of the lead glass. Custom front-end electronics for the detector were designed incorporating the time-over-threshold method to achieve the required time resolution [81].

#### 3.2.8.2 Small Angle Veto - SAV

The Small Angle Veto (SAV) system comprises two calorimeters responsible for vetoing photons emitted between 1 mrad and beam direction. Both are shashlyk calorimeters, with plastic scintillator active regions interspersed by lead plates. Given the low angles of acceptance, the calorimeters are only subject to photons from beam kaon decays with energy $E_\gamma > 5\,\mathrm{GeV}$, requiring an inefficiency $< 10^{-4}$ above this threshold.

The Intermediate Ring Calorimeter (IRC) covers the higher end of the SAV angular acceptance, being an eccentric cylinder positioned just upstream of the LKr. The radial coverage extends to 290 mm, with a central bore of diameter 120 mm with its central axis shifted by 12 mm along the x-dimension to account for the beam direction, see Figure 3.10 b). The calorimeter comprises two modules, of 25 and 45 ring-shaped layers upstream and downstream respectively, with a layer containing a lead plate followed by a scintillator one, both 15 mm thick, totalling $19\,X_0$ for the detector. The scintillator rings are optically separated into quadrants, with light from each quadrant propagated to a single PM by a wavelength-shifting fibre.

The Small Angle Calorimeter (SAC) is a square-cross section detector centered around the z-axis, positioned just before the beam dump and after the final K12 BEND magnet, as shown in Figure 3.2.

It was designed to tag photons emitted at low angles down to the direction of the beam after the MNP33 deflection. The calorimeter consists of 70 layers of $205 \times 205\,\mathrm{mm}^2$ cross-section, each layer being a succession of a 1.5 mm lead plate and a 1.5 mm plastic scintillator plate. Holes bored out in the layers allow for the passage of a wavelengths-shifting fibres coupling the scintillating material to four PMs placed on the downstream end, as shown in Figure 3.10 c). As the scintillating plates are not transversely separated, the SAC is effectively a single-channel detector, with a total depth of $19\,X_0$.

### 3.2.9 Hadronic calorimeters - MUV1 and MUV2

The hadronic calorimeter of NA62 is composed of two detectors, MUV1 and MUV2, positioned in this order downstream of the LKr as shown in Figure 3.3. The MUV2 detector is a refurbished front module of the hadronic calorimeter of the NA48 experiment [73], while MUV1 was constructed specifically for NA62. Both detectors are sampling calorimeters of interspersed iron and scintillator layers. The hadronic calorimeter complements the LKr in providing particle identification information based on energy deposits in the total system.

The MUV1 was designed to provide higher granularity than its refurbished NA48 counterpart. It comprises 24 iron plates of 26.8 mm thickness interspersed by 23 layers of 9 mm thick scintillator strips alternately aligned along the horizontal and vertical, with one more of the former. The transverse dimensions of the layers are $2700 \times 2600\,\mathrm{mm}^2$, with the exclusion of the front and back metal plates, the increased size of which serves to support the structure and cover the readout fibres. The scintillator strips are 60 mm wide, as optimised for pion and muon separation capabilities and cost considerations, and 2620 mm long. Strips in the central region are shortened and split in two to accommodate the beam pipe and the increased hit rates. Wavelength-shifting fibres from full-length strips of the same transverse position (but different depth) lead the light signal to one PM from each strip side. The shorter strips are grouped similarly with readout only from one end, leading to a total of 176 channels.

The MUV2 detector follows a similar layout, with 24 iron plates of 25 mm thickness interleaved with 23 layers of scintillator strips. The MUV2 strips have the transverse dimensions $1300 \times 119\,\mathrm{mm}^2$, with 4.5 mm depth and the layers alternately aligned as for the MUV1. With the strip length spanning half the detector size, the central strips have their ends shaped to allow for the passage of the beam pipe. Strips of the same transverse orientation are optically coupled through Plexiglas wave-guides to a PM. With the geometry constraining the readout to one end of the strips and roughly double the strip width of MUV1, the MUV2 has 88 readout channels.

The total system, as presented from simulation in Figure 3.11, has a thickness of $7.8\,X_0$. Careful calibration of both parts of the hadronic calorimeter allows to achieve the energy resolution of

$$\frac{\sigma_E}{E} = 0.115 \oplus \frac{0.38}{\sqrt{E}} \oplus \frac{1.37}{E}, \tag{3.2.7}$$

where energy has the units of GeV, as measured on 2015 NA62 data [62]. Combination of MUV1, MUV2 and LKr energy deposits enables a significant improvement in this metric.

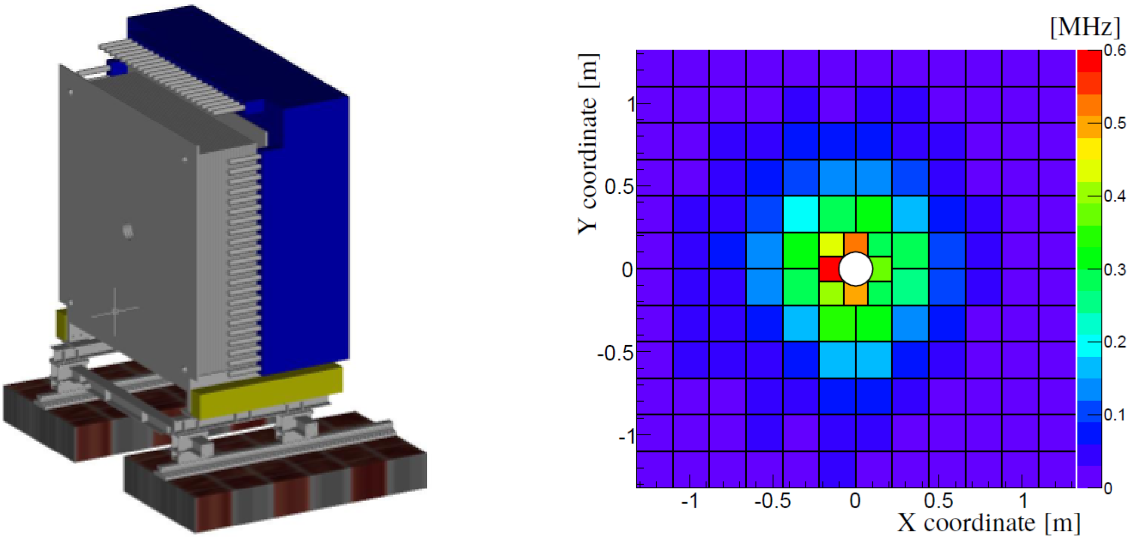

Figure 3.11: Left: Simulated geometry of the MUV1 and MUV2 detectors, left to right. [82] Right: Geometry of the MUV3 detector, with simulated per-tile rate at nominal NA62 beam intensity in MHz. [62]

### 3.2.10 Fast muon veto - MUV3

The MUV3 detector was designed to provide fast information on the presence of muons in the downstream detector, mainly for triggering purposes in case of the $K^+ \to \pi^+ \nu \bar{\nu}$ analysis. It is positioned immediately downstream of a 800 mm thick iron wall, placed just downstream of MUV2. While pions, electrons and positrons originating from beam kaon decays will be absorbed in the NA62 calorimeters and the iron wall, muons can traverse those systems being minimum ionising particles (MIPs). Muon identification, allowing for veto or positive decision at trigger level as well as at the analysis stage, is hence performed by checking for hits in the MUV3 detector.

MUV3 is effectively a charged particle hodoscope, of $2640 \times 2640\,\text{mm}^2$ transverse dimensions and 50 mm tile thickness. The detector geometry, shown in the right panel of Figure 3.11, was chosen to allow association with STRAW spectrometer tracks at analysis level and satisfy the timing requirement of the trigger system, while maintaining sensible per-tile illumination. Majority of the MUV3 tiles (referred to as “outer”) have the transverse dimension of a square with a 220 mm side, leading to a $12 \times 12$ matrix. In the central region spanning $440 \times 440\,\text{mm}^2$ around the beam direction, the beam pipe is accommodated by a 8 smaller tiles (referred to as “inner”), with their edges shaped to tightly enclose the vacuum pipe. Each tile is wrapped in Mylar on its upstream end and sides, to ensure no cross-talk, with the back enclosed in a light-tight box. At the end of each box rest two 2-inch-diameter PMs, with signal from them passed on to CFDs [74] to reduce the time jitter. Muons traversing the PM front window can generate Cherenkov light, with a probability of $\approx 8\%$, leading to a signal arriving 2.5 ns before the scintillation light. The potential time bias from this effect is partially mitigated by using two PMs per tile. As visible from the right panel of Figure 3.11, the MUV3 has a few hot tiles adjacent to the beam hole, which often motivates the use of only outer tiles both for trigger and analysis purposes to avoid the impact of accidental hits. The efficiency of the MUV3 for $>15\,\text{GeV}/c$ muons was measured as $>99.5\%$ on 2015 data, with a single-tile time resolution of $\sim 0.5$ ns [62].

### 3.2.11 MUV0 and HASC

Two additional veto detectors are employed to measure the low momentum $\pi^-$ and high momentum $\pi^+$ originating from $K^+ \to \pi^+\pi^+\pi^-$ ($K_{3\pi}$) decays which fall beyond the geometric acceptance of the downstream spectrometer. Decays with kinematics involving both such particles, if undetected, give a signature consistent with the target $K^+ \to \pi^+\nu\bar{\nu}$ mode.

The MUV0 is a lateral veto positioned to the positive-x side of the downstream RICH flange and covering an area of $1.4 \times 1.4\,\mathrm{m}^2$ with two layers of scintillator tiles. The tiles are grouped into nine super-cells and read out with PMs. $K_{3\pi}$ decays can produce $<10\,\mathrm{GeV}/c$ negative pions receiving a magnetic deflection in the downstream spectrometer opposite to that of the beam, leading to them escaping the STRAW acceptance. The MUV0 was positioned to intercept such pions.

The HASC detector is a hadronic sampling calorimeter positioned downstream of the last BEND magnet of the K12 beam line and shifted into the negative x-values, see Figure‘ 3.2. It is composed of 9 reused modules of a prototype Projectile Spectator Detector [83] developed for the NA61 experiment, with each module having 60 layers of alternating 16 mm lead and 4 mm scintillator plates. The modules are arranged into a $3 \times 3$ matrix, covering a $300 \times 300\,\mathrm{mm}^2$ area, and read out by 360 SiPMs. A $\pi^+$ of momentum $>50\,\mathrm{GeV}/c$ from a $K_{3\pi}$ decay can escape through the central holes of STRAW stations and receive a deflection by a different angle than the K12 beam from the last BEND magnet. The HASC was designed to indicate the presence of such pions.

### 3.2.12 Detector development

The NA62 detector is subject constant development based on the recorded data. Two examples of such changes during Run1 are the introduction of the additional veto detectors described in Section 3.2.11 in 2016 and the improved TCX collimator installed in 2018.

Prior to the start of Run2, two further systems were introduced [84], the VetoCounter and the ANTI-0. The former is a scintillator-tile detector made of two station placed upstream of and one downstream of the final collimator. It was designed to mitigate the “upstream background” of the $K^+ \to \pi^+\nu\bar{\nu}$ analysis due to $K^+$ decays between GTK2 and the final collimator. The latter, ANTI-0, is described in detail in Chapter 4. A new FELIX-based [85] readout system was successfully commissioned for the VetoCounter in 2022 [86]. Changes to detector configuration for Run2 also included the addition of a fourth GTK station, GTK0, neighbouring GTK1, and a second stations of the HASC, placed on the opposite side of the K12 beam line.

A new bespoke hydrogen-filled CEDAR detector, the CEDAR-H [65], was constructed and tested at CERN in 2022 and successfully commissioned as part of the NA62 detector in 2023. The use of hydrogen as a radiator medium reduces the amount of material in the path of the beam due to the KTAG by $\sim$81% as compared to the nitrogen-filled variant, significantly decreasing the amount of beam scattering. The new bespoke optics allow for a an improved single kaon identification efficiency of 99.7% with a time resolution of 66 ps [65], both improving over the nitrogen-filled CEDAR.

## 3.3 Trigger and Data Acquisition System

The high intensity nature of the NA62 experiment necessitates the use of a fast and efficient data acquisition system. The elusive nature and extremely low branching ratio of the target $K^+ \to \pi^+\nu\bar{\nu}$ mode (see Equation 2.3.3) requires a highly selective yet efficient main trigger line, as well as complimentary data sets for control and calibration of the individual detectors. To meet all the requirements, a CERN-developed Timing, Trigger and Control (TTC) system [87] , delivering a centralised uniform clock signal of $\sim$40 MHz frequency from a high-precision low-jitter clock was employed. The clock is decoupled from that of the accelerator complex, as the active data-taking phases of the experiment are defined by the spill duration of the SPS of $\sim$3 s, with variable breaks in between of at least $\sim$12 s. The signal generated in the NA62 detector due to particles generated from a single SPS spill is a standard unit of NA62 data, a “burst”, including events selected by all the applied trigger streams. Synchronisation between detector readout electronics is ensured by sending a common start-of-burst signal to all sub-systems, followed by an end-of-burst one a fixed number of clock cycles away, ensuring uniform timing during particle delivery. Outside of a burst, the systems can independently perform clean-up tasks. A fixed number of no more than 1500 bursts due to consecutive SPS spills constitutes a single “run” (unrelated to the the Run1 and Run2 data-collection periods), a larger unit NA62 data providing sufficient statistics to assess per-system detector performance. Runs are further grouped into “samples”, representing sets of data collected under similar conditions pertaining to detector and beam setup or data quality.

The output data rate of O(10 MHz) makes operating a completely trigger-less approach unfeasible, hence the experiment adopted a two-level approach, comprising a L0 hardware and L1 software triggers (the latter often referred to as HLT for High Level Trigger). The L0 system [88] relies on fast information from a subset of detectors, see a schematic of the NA62 TDAQ system in Figure 3.12. The RICH, NA48-CHOD, CHOD, LKr and MUV3 each generate a set of L0 primitives, i.e. binary flags containing a decision on some predetermined conditions, such as whether a predetermined number or combination of signals were generated in the system. The L0 primitives are delivered from the detectors to the L0 trigger processor (L0TP) [89], which evaluates if any from a set of pre-defined trigger conditions (masks) are satisfied. In the event of a positive decision, a request is propagated to all detectors used at L1 stage (KTAG, STRAW, LAV) to send data to the PC farm together with the L0 ones, forming a L1 event. If a set of L1 algorithms chosen for a given L0 mask gives a positive decision, data from the remaining detectors (hadronic calorimeters and the GTK) is sent to merger computers, which group it together with the L1 event and save to disk. Each trigger line, comprising a L0 mask and the associated L1 algorithms, can be run at an integer downscaling, $D$, where only one in every $D$ positive decisions at L0TP level results in sending the L1 request. This approach enables efficient use of the available bandwidth of the NA62 TDAQ system, allowing for collection of $K^+ \to \pi^+\nu\bar{\nu}$ data, as well as sets for calibration, performance studies and a variety of other pursuits in the kaon sector: precision measurements, exotics and BSM searches. Each trigger stage reduces the data rate by a factor of $\approx$ 10, leading to a $\sim$100 kHz final output rate. The existing infrastructure allows for parallel operation of multiple L0 masks, with possible extensions in terms of additional detectors or multi-detector algorithms at L1. A detailed overview and performance of the NA62 trigger system as operated in 2018 can be found in [90].

Given similar time resolutions of a majority of the L0 detectors, as well as the requested setup flexibility, a common readout board based on the LHCb TELL1 [91], called TEL62 [92] was developed

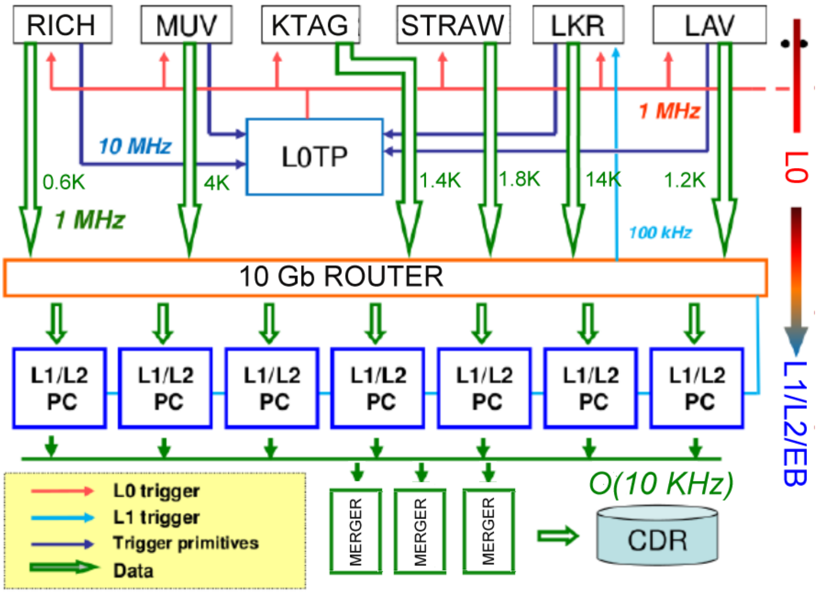

Figure 3.12: Schematic drawing showing the data flow and rates from a subset of NA62 detectors. [62]

for NA62, providing improved storage, computing power and inter-communication capabilities. Each TEL62 houses four custom built TDCB modules [93], providing time-to-digital conversion for up to 128 channels at ∼100 ps precision. The list of systems read out by TEL62 boards comprises KTAG, CHANTI, LAV, RICH, NA48-CHOD, CHOD and MUV3. For the GTK, the on-detector readout approach necessitates the use of custom chips, called TDCpix [68], as visible in Figure 3.5. Data from each of the 10 sensors for each GTK station is handled by a single chip. The STRAW detector, while sharing the efficiency requirement with TEL62 detectors, has a worse time resolution by design, hence an alternative solution was deemed appropriate on cost grounds. At the front-end, groups of 8 tubes are read out through a single CARIOCA chip [94], designed by the LHCb Collaboration. Data from 32 such chips is then propagated to a bespoke STRAW Readout Board (SRB), with 8 of these serving a single STRAW station. A custom board, Calorimeter Readout MOdule (CREAM) [95], was developed for the LKr calorimeter. Within NA62, the CREAM system is used to process signal from the IRC, LKr, MUV1, MUV2 and SAC calorimeters.

## 3.4 Software framework

The NA62 software framework (na62fw) [96], is a complete software toolkit for the reconstruction, simulation and analysis of data collected by the NA62 experiment, written mostly in the C++ programming language. The framework has a modular layout and incorporates scripts allowing automated processing of real and simulated data, with the individual elements described below.

### 3.4.1 NA62MC

The NA62MC is a module of the na62fw responsible for the simulation of particle decays within the NA62 setup and the associated detector response using Monte-Carlo methods. The NA62 beam and particle interactions with the beam line elements up to the KTAG detector are handled using the TURTLE [97] or BDSim [98] packages. The resultant beam characteristics are then passed on to a Geant4-simulated [99] version of the NA62 detector. The Geant4 toolkit is highly configurable, allowing the usage of various packages for simulation of the whole range of relevant physical processes, as well as for detailed geometric and physical-property definitions of the used materials. In case of NA62MC, custom $K^+$ decay generators based on most up-to-date theoretical calculations are employed to guarantee the accuracy of emulated processes. The physics of particle interactions within individual detector systems can be specified independently, to maximise computational efficiency given the required precision and limited resources. For example, for the charged particle hodoscopes of NA62, photon-by-photon light propagation within scintillator tiles is abandoned in favour of the total energy deposit per tile as generated by the passage of a single charged particle. The geometry simulation of the NA62 detector involves not only the active detector regions but also magnets, collimators and relevant support structures, with details of all vessels, to account for the possible effects of particle interactions with those volumes. The NA62MC was recently updated to allow flexibility in terms of the subset of detectors simulated, as well as their position and orientation. The run-time implementation of this mechanism allows for simulating data corresponding to detector setup for different data-taking periods. The Geant4 functionality allows to not only record the detector response due to passage of simulated particles but also track the true simulated positions and interactions, in which the emulated particles were involved.

NA62 data is simulated within NA62MC in samples made up of one type of kaon decay, with the beam kaon forced to decay in a particular z-position range by undergoing a specific process, for instance the $K^+ \to \pi^+\nu\bar{\nu}$. The relative probability of particle decay within the requested range is driven by the kinematics, with the most often used range spanning (102.5 to 180) m, corresponding to the detector FV. Such an approach allows for resource-efficient combination of relevant decays for analysis purposes. For simulated data, the $K^+$ decay defines the reference time for an event, contrary to real data, where trigger time is used, as provided by a chosen reference detector, in most cases the RICH.

### 3.4.2 NA62Reconstruction

The NA62Reconstruction module is responsible for converting raw data coming from individual detector systems, and their multiple stations where relevant, into candidates, i.e. objects representing physical attributes of the particle generating the signal. To facilitate the use of real and simulated data at analysis stage, NA62Reconstruction processes both to give the same output format. Real raw data, given prior signal manipulation by the front-end electronics and by definition subject to real resolution effects, is decoded and the read-out channel, i.e. link propagating the data throughout the physical part of the TDAQ system, is converted to geometric channels ID, often chosen to enable the quick identification of position within the system. In the case of simulated data (referred to as MC), the information must be “digitised” to allow for processing by the same chain as the real one. MC digitisation involves inverse conversion from geometric to readout channel ID, as well as emulating the effects of front-end electronics and physical signal propagation. To take the CHOD as an example, simulation of the CFDs present in the readout chain is performed by rejecting energy deposits below a certain threshold, dead-time is accounted for by rejecting hits closely following another and the hit time receives as randomised contributions from a zero-centered Gaussian with the width defined by the measured resolution. Once the two streams (real and MC data) are brought to the same state, data reconstruction begins. This process involves combining hits from individual channels in space and time to form candidates, with the complexity and information provided varying significantly between detectors, each running a separate algorithm. Looking at the CHOD again, hits from the two readout channels of a single tile within a configurable time window can be combined into a candidate, giving the classification of loose (one hit) and tight (two hit) candidates, with time of the latter defined as the average between hits. For systems boasting several thousand channels and non-trivial geometry, such as the magnetic spectrometers, the LKr or the RICH, complex algorithms, involving software level data-driven corrections, are implemented. The per-system reconstruction algorithms within NA62Reconstruction also fill a range of low-level monitoring histograms, such as channel illumination or timing relative to a fixed reference. These are used for online validation of correct operation of detectors during NA62 data-taking.

Given the high intensity of the NA62 kaon beam, MC-simulated data involving decays of a single kaon per event does not accurately represent the experimental conditions. To account for the presence of additional detector activity due to both beam halo particles and other in-time decays, an overlay system was developed. Instantaneous beam intensity values are sampled for each simulated event from a distribution obtained from a reference run and based on them, a suitable number of "overlay" events is injected uniformly into the $\pm 200\,\mathrm{ns}$ time window around the reference time. The type of each individual event is selected randomly from a set representing the NA62 hadron beam, most often giving non-decaying beam particles, like pions, protons or kaons, and the beam halo, mostly comprised of muons generated in upstream decays or interactions with the K12 beam line elements. In the event that a kaon which would decay is chosen, the mode is randomly selected from the six main ones with relative probability driven by the branching ratios. The position of the overlaid decay is sampled from the distribution defined by the kaon lifetime and beam momentum. All these steps are taken for simulated data only before applying the reconstruction methods, allowing to accurately model the high-intensity environment of the NA62 experiment.

### 3.4.3 NA62Analysis

The NA62Analysis module is a ROOT-based [100] software framework, written and maintained as part of the na62fw, simplifying the access to NA62 data-propagation classes. It was intended for users and contains central methods automatically providing requested detector information and opportunities to execute target code at levels compatible with the structure of NA62 data, together with simple handles for extracting modified data from the framework. NA62Analysis also houses a number of analytical tools, such as a vertex fitter for STRAW tracks optionally including a kaon track from the GTK or the builder of "downstream tracks" - objects composed of STRAW tracks geometrically associated with information from other downstream systems obtained from independently optimised methods. The components further include a set of single-detector and universal calibration analyzers, allowing for software-level corrections positively impacting detector performance, such as timing and energy scaling. Methods to evaluate the performance of an individual system on a chosen subset of events, including the above corrections, are also provided to allow for verification of efficiency and timing performance of both the detector system as a whole and individual channels. Finally, the NA62Analysis hosts a set of standard event selections for important decay modes such as $K_{3\pi}$ and $K^+ \to \pi^+\pi^0$, which are critical benchmarks of total experiment performance given their relevance to the target $K^+ \to \pi^+\nu\bar{\nu}$ analysis. The uniform structural design of all the tools outlined above enables automatic execution as part of the NA62 data-processing chain, giving prompt and easy user-level access to key performance metrics of the experiment.

### 3.4.4 NA62Tools

The NA62Tools part of the na62fw contains code allowing communication between the other three modules of the framework and some standard configuration for the other modules. In particular, the definitions of classes for data propagation between NA62MC, NA62Reconstruction and NA62Analysis are housed within NA62Tools. With the large volume of data generated by the experiment and substantial amount of simulated data required to carry out analyses, the reconstruction-level data is saved in ''slim" format, with any redundant variables removed. NA62Tools contains the methods for conversion between full and slim data formats, as well as central classes allowing access to geometry of a number of detectors, for example the MUV3, where tile positions can easily be deduced from geometric tile ID.

## 3.5 $K^+ \to \pi^+\nu\bar{\nu}$ Analysis

A 10% precision measurement of the $K^+ \to \pi^+\nu\bar{\nu}$ decay is the main goal of the NA62 Experiment. This section summarises the analysis approach and result for Run1 data only, fully described in Reference [1].

The experimental signature of the $K^+ \to \pi^+\nu\bar{\nu}$ process is an upstream $K^+$ and a downstream $\pi^+$, characterised by four momenta $P_K$ and $P_\pi$ respectively. The key kinematic quantity enabling differentiation of this decay from others under the experimental constraints is the squared missing mass,

$$m^2_{miss}(K-\pi) = (P_K - P_\pi)^2, \tag{3.5.1}$$

which is expected to peak at zero given the observed limits on neutrino masses are below the kinematic resolution of NA62. Given the presence of two neutrinos in the final state, the signal spectrum in $m^2_{miss}(K-\pi)$ is not a narrow peak. The simplicity of the experimental signature, i.e. a single positively charged track identified as pion, can be mimicked by all kaon decays with a $\pi^+$ in the final state should the other final state particles escape detection or a by single-track decay, such as $K^+ \to \mu^+\nu_\mu$ ($K_{\mu 2}$) or $K^+ \to e^+\nu_e$, in case of misidentification. Another potential background involves both misidentification of a positive track and lack of reconstruction of the remaining daughters. Signal regions for the analysis are defined in a two-dimensional space of $m^2_{miss}$ and $p_\pi$, the pion momentum, based on the shapes generated by three key background modes, which are the three main decay modes of the $K^+$: $K_{\mu 2}$, $K^+ \to \pi^+\pi^0$ ($K_{2\pi}$) and $K^+ \to \pi^+\pi^+\pi^-$ ($K_{3\pi}$). The shapes generated by the three key background modes and the analysis signal regions are shown in Figure 3.13. Region 1 spans

$$\begin{aligned} &m^2_{miss}(1) \in [0, 0.010]\ \mathrm{GeV}^2/c^4, \\ &p_\pi(1) \in [15, 35]\ \mathrm{GeV}/c, \end{aligned} \tag{3.5.2}$$

with the upper $m^2_{miss}$ limit driven by the $K_{2\pi}$ peak, while the lower $m^2_{miss}$ one and the highest allowed pion momentum are defined by the $K_{\mu 2}$ band. Region 2 is limited only along $m^2_{miss}$ dimension, by the $K_{2\pi}$ peak and the $K_{3\pi}$ distribution tails from below and above respectively, so that

$$\begin{aligned} &m^2_{miss}(2) \in [0.026, 0.068]\ \mathrm{GeV}^2/c^4, \\ &p_\pi(2) \in [15, 45]\ \mathrm{GeV}/c, \end{aligned} \tag{3.5.3}$$

exploiting the whole kinematic range of pion momenta. Data collected in 2016, 2017 and the first

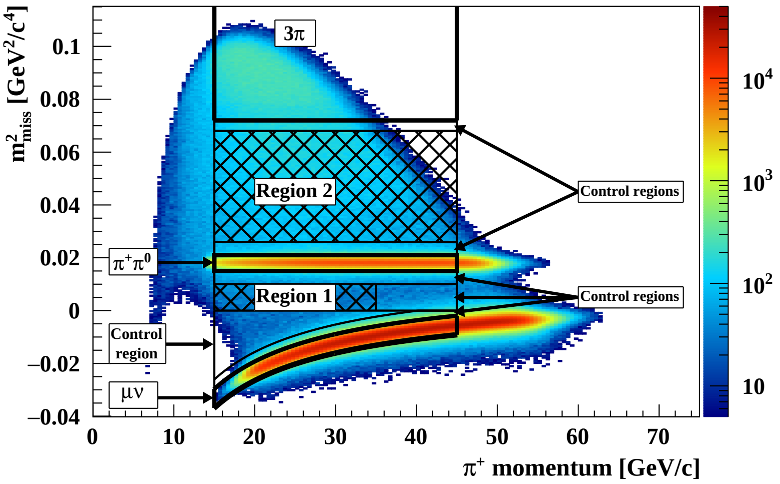

Figure 3.13: Reconstructed spectrum of $m^2_{miss}$ versus $p_\pi$ obtained without the application of $\pi^+$ PID and photon rejection from for minimum-bias events. Charged kaon and pion masses are assumed for the upstream and downstream particles respectively. Shaded contours shown are signal regions 1 and 2 (hatched areas). Thick-black lines delineate background regions for three most prominent decay modes: $K_{\mu 2}$, $K_{2\pi}$ and $K_{3\pi}$, marked as $\mu\nu$, $\pi^+\pi^0$ and $3\pi$ respectively. All of the control regions separating the signal and background ones are also labelled. [1]

∼20% of 2018 (before installation of the TCX collimator) is integrated over the momentum range, giving three separate categories. The remainder of 2018 data is split by momentum range with bins spanning 5 GeV/$c$, resulting in additional six categories. The selection is optimised independently for each of the nine categories to maximise signal sensitivity, while keeping the signal region blinded.

The analysis relies on extracting the target branching ratio based on two key quantities: the single event sensitivity (SES) and the expected numbers of background events per signal category. The SES is defined as

$$SES = \frac{1}{N_{K^+} \cdot A_{\pi\nu\bar{\nu}} \cdot \epsilon_{RV} \cdot \epsilon^{\pi\nu\bar{\nu}}_{trig}} = \frac{\mathfrak{B}(K^+ \to \pi^+\pi^0) \cdot A_{\pi\pi}}{N_{\pi\pi} \cdot D \cdot A_{\pi\nu\bar{\nu}} \cdot \epsilon_{RV} \cdot \epsilon^{\pi\nu\bar{\nu}}_{trig}}, \tag{3.5.4}$$

where $N_{K^+}$ is the observed number of kaon decays in the FV computed from $K_{2\pi}$ decays, $A_{\pi\nu\bar{\nu}}$ is the acceptance of the signal mode computed from simulated data with form factors extracted from the $K^+ \to \pi^0 e^+ \nu$ process, $1 - \epsilon_{RV}$ is the total signal inefficiency arising from the use of multiple detectors in veto mode, measured on $K_{\mu 2}$ data, and $\epsilon^{\pi\nu\bar{\nu}}_{trig}$ is the efficiency of the trigger stream used to collect signal mode data. The number of kaon decays in the FV is taken from data collected with a minimum-bias trigger of downscaling $D$, where $N_{\pi\pi}$ and $A_{\pi\pi}$ are the number of observed $K_{2\pi}$ events and the acceptance of this mode computed from simulation.

The signal and normalisation selections share a similar signature, leading to the adoption of a similar set of requirements to minimise systematic effects. For both modes, a single downstream particle is requested, falling withing the acceptance and having space-time compatible associations from the RICH, NA48-CHOD, CHOD and LKr. The track is identified as a pion based on the lack of in-time MUV3 associations, a boosted decision tree (BDT) verdict made on a set of calorimetric variables and either a species PID probability or particle mass fit from associated RICH data. The upstream kaon is identified from information provided by the GTK and KTAG, taking into account the timing compatibility between both the two and the downstream RICH time, the closest distance of approach (CDA) to the downstream STRAW track, as well as additional activity in the GTK. For a matched kaon - pion candidate pair one employs either another BDT or a set of cuts based on the position of the reconstructed decay vertex and directions of the upstream and downstream particles, followed by a request of no in-time CHANTI activity to suppress interactions in GTK3 and upstream decays. The normalisation events are chosen from the phase-space region of

$$\begin{aligned} &m^2_{miss}(Norm) \in [0.010, 0.026] \text{ GeV}^2/c^4, \\ &p_\pi(Norm) \in [15, 45] \text{ GeV}/c, \end{aligned} \tag{3.5.5}$$

where the first dimension covers ±8-times the variable resolution. The signal selection requests an in-time photon and charged particle veto, based on information from both the electromagnetic calorimeters, downstream spectrometer, charged particle hodoscopes, RICH and additional veto detectors.

The backgrounds to the $K^+ \to \pi^+\nu\bar{\nu}$ process can come from two distinct categories, either other $K^+$ decays occurring in the FV with some kaon daughters not reconstructed, or from upstream events, where the observed pion track is due to an upstream decay of a beam kaon or interaction of a beam pion with the upstream material. The former category is quantified from a combination of data-driven and simulation-based methods, where the expected contamination of the signal or control regions is computed from the contributions to the phase-space regions dominated by background decays in question and the kinematic fraction of events falling into the signal region. The four most prominent modes evaluated with this method are $K_{2\pi}$, $K_{\mu2}$, $K_{3\pi}$ and $K^+ \to \pi^+\pi^-e^+\nu$. Due to limited data statistics in the relevant trigger stream, the preferred purely data-driven methodology is applied only to the first two processes. For the third, a mixture of data and simulation are used and the last one is evaluated by simulation only. The upstream background event contribution is modeled with a completely data-driven approach. An upstream sample in bins of time difference between GTK and KTAG, $\Delta T$, is constructed by reversing the CDA condition, requesting failed kaon-pion matching and taking events falling into the two signal regions. The probability of such events to be mistagged is computed from generated events in the $(CDA, \Delta T)$ plane per $\Delta T$ bin. The sum over all bins provides the total upstream estimate.

Prior to unblinding the signal regions, the background estimation procedure is verified on the control regions as defined in Figure 3.13. The numerical estimates together with the associated errors were found to be fully compatible with data in those regions of the phase-space, yielding a total expected background contamination of [1]

$$N^{exp}_{background} = 7.03\,^{+1.05}_{-0.82} \tag{3.5.6}$$

for the sum of the two signal regions over all 2016-2018 data, with the uncertainty dominated by the statistical power of the upstream estimate. Upon unblinding, 17 signal candidates were observed in 2018, presented in Figure 3.14, adding up to 20 total with the inclusion in 2016 and 2017. The single event sensitivity corresponding to the whole period is [1]

$$SES = (0.839 \pm 0.053_{\text{Syst}}) \times 10^{-11}, \tag{3.5.7}$$

with a negligible statistical uncertainty. The systematic uncertainty receives sizeable contributions from correlation of L0 and L1 trigger efficiency measurements, the uncertainty in measuring the L1

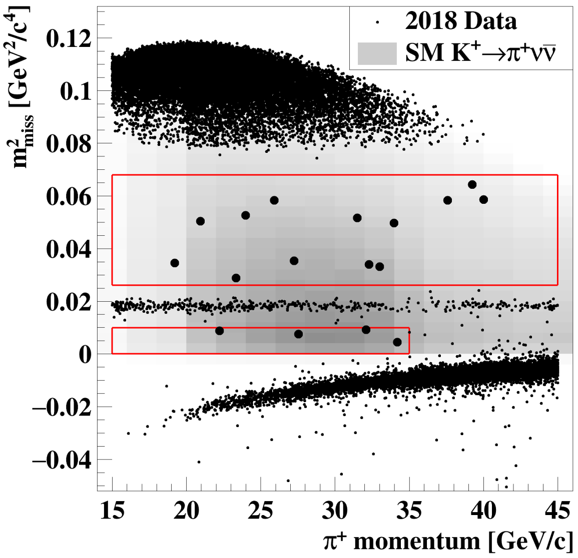

Figure 3.14: Distribution of $K^+ \to \pi^+ \nu\bar{\nu}$ candidate events as obtained from 2018 NA62 data on the $(m^2_{miss}, p_\pi)$ plane. Signal regions are delimited by red rectangles, with the gray shading showing the predicted variation in SM acceptance. Points outside the red rectangles demonstrate the amount of data collected in control and background regions. [1]

efficiency and the random veto efficiency measurement.

The target branching ratio is quantified by performing a binned maximum log-likelihood fit given the observed number of data candidates in each of the nine categories. The target parameter is the global $K^+ \to \pi^+ \nu\bar{\nu}$ branching ratio, with the nuisance parameters of total expected background count and single event sensitivity with associated uncertainties, evaluated independently for each category. The numerical value of [1]

$$\mathfrak{B}(K^+ \to \pi^+ \nu\bar{\nu}) = (10.6\,^{+4.0}_{-3.4}|_{\mathrm{Stat}} \pm 0.9_{\mathrm{Syst}}) \times 10^{-11}, \tag{3.5.8}$$

is obtained, with the first uncertainty term due to the Poisson statistics of the number of expected background and observed signal events, and the second due to the systematic uncertainties in estimating both quantities. The result is the most precise to date, with the observation of signal having a 3.4 standard deviation significance. The NA62 Run2 started in 2021 promises a significant reduction in the dominant statistical uncertainty.

# Chapter 4

# The ANTI-0 Detector

The ANTI-0 detector [101] was introduced to the NA62 Experiment prior to the Run2 data-taking campaign. The ANTI-0 is positioned between the CHANTI detector and the large vacuum tank housing the FV, as shown in Figure 4.1 depicting an early prototype. This chapter covers the motivation for ANTI-0 introduction, detector and readout design, as well as the software package developed by the author for simulation and reconstruction of data from the system. The software is complemented by analysis-level tools used for correlating signals from the ANTI-0 detector and those from other systems, and online validation of detector performance. The chapter concludes with a description of ANTI-0 data quality in the 2021-2023 data-taking periods.

## 4.1 Motivation and requirements

The ANTI-0 was designed to tag, i.e. indicate the presence of, particles originating from upstream of the evacuated decay vessel with trajectories inconsistent with the K12 beam. A STRAW track produced by an upstream particle falling within the acceptance of downstream PID detectors gives the same experimental signature as a product of a K12 beam particle decay. The presence of such tracks is a potential source of background for physics analyses as well as a contribution to the bandwidth used by trigger lines targeting multi-track decays, which are implemented with a downscaling $> 1$.

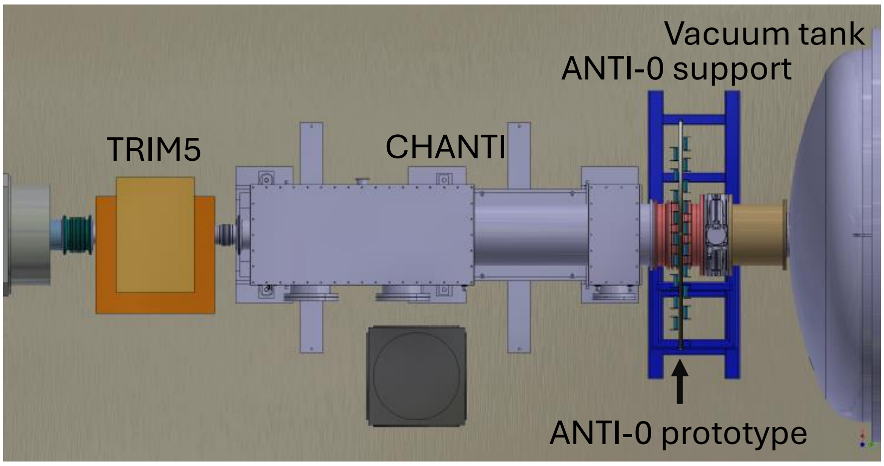

Figure 4.1: Schematic view from the top of the position of ANTI-0. The detector and support structure shown correspond to early prototypes, consistent with the final design in terms of placement and geometry. [102]

Upstream particles entering the decay vessel outside of the design beam acceptance can originate from beam particle decays upstream of the FV, interactions with the material of the beam line or from a combination of the two processes. The K12 beam composition (see Table 3.2) together with the dominant decay modes of $\pi^+$ and $K^+$ into a $\mu^+\nu_\mu$ pair give a substantial upstream muon component. A study of experimental scalers with the T10 target in and out and the TAX collimators open and closed [103] shows that nearly half of the muon rate seen by the MUV3 detector under nominal beam intensity is due to upstream muons [102].

The NA62 experiment can be operated in “dump mode”, with the T10 target removed and TAX collimators closed to fully absorb the proton beam, in search for exotic long-lived particles [104]. For such particles decaying into a variety of final states the ANTI-0 is crucial for identification of upstream background, as signatures of non-muonic final states can arise from inelastic interactions of upstream muons with the vessel or downstream systems. The NA62 experiment aims to collect “dump mode” data for about at least a week in every year of operation, with the set obtained in 2021 already investigated for the presence of a Dark Photon [105] [106].

With the ANTI-0 position determined by its desired function, four other key requirements were considered during detector design: high efficiency, complete coverage of the sensitive area, time resolution of $\sim$300 ps and radiation hardness. The first two ensure no upstream particles enter the decay vessel undetected, the third allows for in-time veto with resolution comparable to that of downstream detectors, and the last is required to withstand the expected high irradiation given the detectors position. To allow for potential implementation into the NA62 trigger system, the detector should be fast, TEL62-compatible and offer suitable granularity in the transverse plane to mitigate the impact of accidental activity.

## 4.2 Detector and readout design

This section contains the description of the ANTI-0 detector, contextualising the work done to simulate the detector and evaluate the quality of data collected by the system, with details of detector design available in Reference [101].

To satisfy the requirements outlined in the previous section, a segmented charged particle hodoscope was constructed, covering the radial range up to 1080 mm in the (x,y) plane and with a central hole allowing for the beam pipe. The ANTI-0 consists of 280 identical counter tiles, positioned on opposite sides of a 5 mm thick central support sheet made from aluminum. The detector is split into two parts, top and bottom as shown in Figure 4.2, to enable installation around the fixed beam pipe. Additional aluminum sheets covering the transverse span of the detector are placed on the open faces of the support frame to ensure the system is light-tight.

To satisfy the hermiticity requirement, the counters are arranged in a chessboard pattern, with vertical and horizontal neighbours placed on opposite sides of the support sheet and overlapping by 4 mm, as shown in the left panel of Figure 4.3. The active area of a counter is a $124 \times 124\,\mathrm{mm}^2$ rectangle with the corners removed, giving the separation between centers of neighbouring tiles of 120 mm. Individual tiles are 10 mm thick scintillation plates made of polystyrene doped with 2% PTP and 0.02% POPOP, see Reference [108] for material properties.

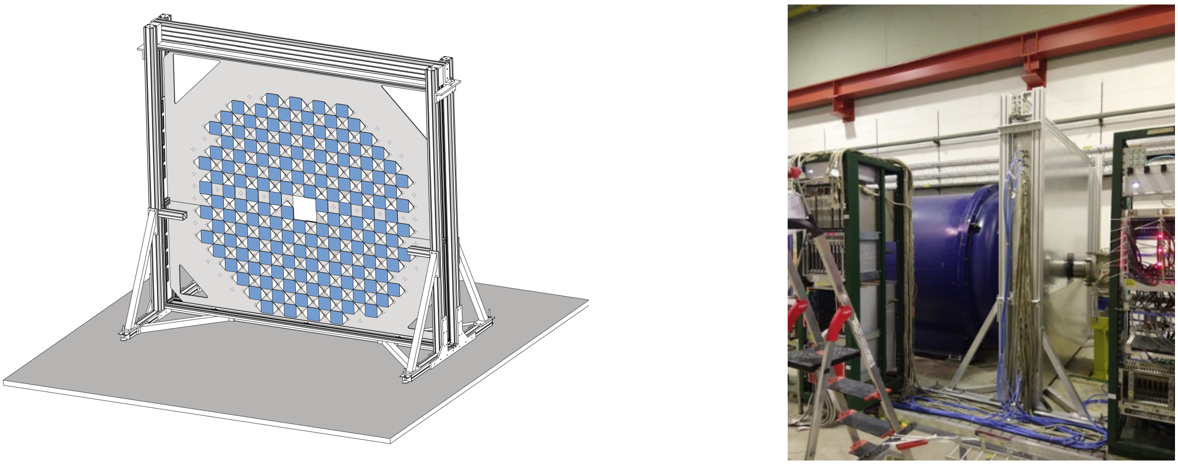

Figure 4.2: Left: A schematic of the ANTI-0 detector showing the support frame, central sheet and counters. Note the horizontal line just below the mid-point of the detector delimiting the top and bottom parts. [101] Right: Picture of the ANTI-0 as installed in TCC8, with the blue decay vessel to the left and beam pipe to the right. [107]

Time resolution studies of scintillating counter prototypes for the NA62 CHOD detector showed an improved performance of direct light collection in contrast to readout through wavelength-shifting fibres [109], hence the former approach was pursued for the ANTI-0. Silicon photomultipliers (SiPMs) of S14160-6050HS type are used for the ANTI-0 and optically coupled to the scintillating material through Plexiglas lightguides and optical grease. Individual tiles are wrapped in Tyvek to ensure light-tightness. Monte-Carlo studies in Geant4 [99] were conducted to select the optimal length of lightguides and number of SiPMs per counter. Average signal arrival time as a function of both signal amplitude and particle crossing position were more uniform for 40 mm lightguides than for the 20 mm alternative, with the maximum length limited by tile spacing. The cases of one, two and four SiPMs per counter placed near the corners of the lightguides (as shown in the right panel of Figure 4.3) were investigated, with the sum of signal amplitudes and average time of signal arrival being the most uniform for the highest number. A lateral spacing of 60 mm between the two SiPMs on the same side of the tile (group A/B) was chosen for light collection uniformity, completing the counter design.

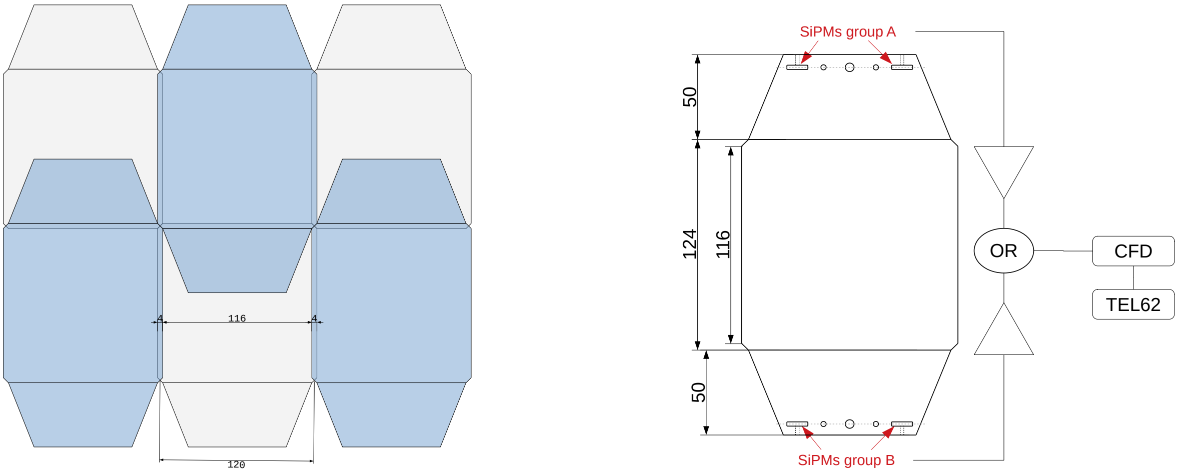

Figure 4.3: Left: Spacing of individual ANTI-0 counters, with the blue and grey units placed on opposite sides of the main support sheet. Right: schematic of an individual counter, including the readout architecture. [101]

The SiPMs from the same group, as labelled in the right panel of Figure 4.3, are connected in series, with the signal from each group amplified by a factor of ≈30. Pulses from the two groups are summed by an analogue ’OR’ and passed to a CFD module [74], used to optimise the time resolution, giving one readout channel per ANTI-0 tile. The CFD output from each tile is read by a TEL62 channel, allowing for easy integration with the existing NA62 data acquisition infrastructure.

While the majority of the counters are oriented horizontally, i.e. having the lightguides on the left and the right, as shown in the left panel of Figure 4.2, the beam-pipe hole requires at least the four counters placed to the sides of it to be oriented vertically. This is only possible with an additional displacement along the z-axis, given the size of the lightguides precludes two positioned orthogonally occupying a single gap between counters on one side of the central sheet. Additional displacement along the z-axis was also implemented for the top row of the bottom part of the detector and bottom row of the top part to aid with installation, with the two parts delimited by a horizontal line in the left panel of Figure 4.2. In the top (bottom) row of the bottom (top) part of the ANTI-0 tiles are moved by a further 4(15) mm away from the central sheet. The four counters to the sides of the beam pipe hole oriented vertically (with geometric ID 121, 123, 421 and 423, see Section 4.3.1), must be displaced by a further 15 mm.

Prior to detector assembly, a study of the timing capabilities of the counters was performed using cosmic rays. Four counters were stacked in a light-tight box, with the outer two serving as trigger for recording the passage of particles through the inner tiles with an oscilloscope. A Gaussian fit to the obtained distribution for the time difference between the inner two tiles gave a single counter resolution of [101]

$$\sigma_t = 220 \text{ ps}, \tag{4.2.1}$$

with the assumption of identical tiles.

The detector was assembled and connected to power and readout systems in early 2021 prior the the start of NA62 Run2. The right panel of Figure 4.2 shows the ANTI-0 detector after installation, with one of the two outer sheets visible, as well as the power and readout modules of the ANTI-0 placed in an electronics rack. The readout channels of the detector were grouped in geometric sectors according to expected hit rates at the NA62 nominal beam intensity [101], to ensure compliance with the rate capabilities of the TDCB modules of TEL62 boards.

## 4.3 Software package

The software package for the ANTI-0 was developed within the na62fw by the author of this thesis, expanding on the existing universal methods for data manipulation and propagation in the framework. The software package enables MC simulation of data, reconstruction of both real and simulated data and online data-quality validation, with the class structure defined by design of the framework. The NA62Analysis module contains standardised tools for coarse time alignment of all channels from a single TDCB module and fine one for individual channels, as well as a crucial “analyzer” responsible for geometrically matching the downstream spectrometer (STRAW) tracks to ANTI-0 activity, called *SpectrometerANTI0Association*. The output of the latter can be used for offline validation of detector performance, packaged into another analyzer, called *ANTI0Efficiency*.

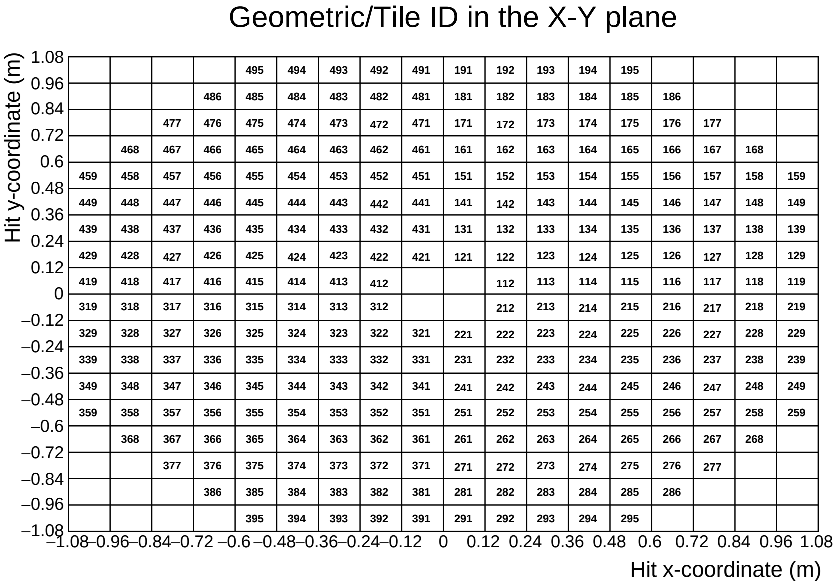

| | | | | | | | | | | | | | | | | | |
|---|---|---|---|---|---|---|---|---|---|---|---|---|---|---|---|---|---|
| | | | | 495 | 494 | 493 | 492 | 491 | 191 | 192 | 193 | 194 | 195 | | | | |
| | | | 486 | 485 | 484 | 483 | 482 | 481 | 181 | 182 | 183 | 184 | 185 | 186 | | | |
| | | 477 | 476 | 475 | 474 | 473 | 472 | 471 | 171 | 172 | 173 | 174 | 175 | 176 | 177 | | |
| | 468 | 467 | 466 | 465 | 464 | 463 | 462 | 461 | 161 | 162 | 163 | 164 | 165 | 166 | 167 | 168 | |
| 459 | 458 | 457 | 456 | 455 | 454 | 453 | 452 | 451 | 151 | 152 | 153 | 154 | 155 | 156 | 157 | 158 | 159 |
| 449 | 448 | 447 | 446 | 445 | 444 | 443 | 442 | 441 | 141 | 142 | 143 | 144 | 145 | 146 | 147 | 148 | 149 |
| 439 | 438 | 437 | 436 | 435 | 434 | 433 | 432 | 431 | 131 | 132 | 133 | 134 | 135 | 136 | 137 | 138 | 139 |
| 429 | 428 | 427 | 426 | 425 | 424 | 423 | 422 | 421 | 121 | 122 | 123 | 124 | 125 | 126 | 127 | 128 | 129 |
| 419 | 418 | 417 | 416 | 415 | 414 | 413 | 412 | | | 112 | 113 | 114 | 115 | 116 | 117 | 118 | 119 |
| 319 | 318 | 317 | 316 | 315 | 314 | 313 | 312 | | | 212 | 213 | 214 | 215 | 216 | 217 | 218 | 219 |
| 329 | 328 | 327 | 326 | 325 | 324 | 323 | 322 | 321 | 221 | 222 | 223 | 224 | 225 | 226 | 227 | 228 | 229 |
| 339 | 338 | 337 | 336 | 335 | 334 | 333 | 332 | 331 | 231 | 232 | 233 | 234 | 235 | 236 | 237 | 238 | 239 |
| 349 | 348 | 347 | 346 | 345 | 344 | 343 | 342 | 341 | 241 | 242 | 243 | 244 | 245 | 246 | 247 | 248 | 249 |
| 359 | 358 | 357 | 356 | 355 | 354 | 353 | 352 | 351 | 251 | 252 | 253 | 254 | 255 | 256 | 257 | 258 | 259 |
| | 368 | 367 | 366 | 365 | 364 | 363 | 362 | 361 | 261 | 262 | 263 | 264 | 265 | 266 | 267 | 268 | |
| | | 377 | 376 | 375 | 374 | 373 | 372 | 371 | 271 | 272 | 273 | 274 | 275 | 276 | 277 | | |
| | | | 386 | 385 | 384 | 383 | 382 | 381 | 281 | 282 | 283 | 284 | 285 | 286 | | | |
| | | | | 395 | 394 | 393 | 392 | 391 | 291 | 292 | 293 | 294 | 295 | | | | |

Figure 4.4: Geometric ID of ANTI-0 tiles as defined in the $(x, y)$ plane of the detector. The simplified counter dimensions of $120 \times 120\,\mathrm{mm}^2$ do not account for overlaps.

### 4.3.1 ANTI-0 simulation

As described in Section 3.4.1, the NA62MC module utilises the existing Geant4 [99] capabilities for simulating matter-particle interactions. Hence, the simulation of the ANTI-0 detector relies on an accurate description of the geometry of the detector as well as the usage of the correct materials and the provision of data storage classes for values extracted from central methods.

Following the approach taken for CHOD and MUV3 detectors, to minimise computing time, light generation and propagation within the ANTI-0 counters is not simulated. Instead, when a particle crosses the active part of each counter, i.e. the scintillator material, the deposited energy is calculated by Geant4 and saved. This quantity, together with the simulated time of particle passage, the position and geometric ID of the crossed counter and an integer index uniquely identifying the incident particle define an MC "hit", an object stored for later software processing. The saved particle crossing time is the true simulated value, with resolution effects due to readout electronics emulated at the digitisation stage (see Section 4.3.2). Individual hits are stored in an object of the "event" class, one of which is generated for each simulated top-level particle, most often a $K^+$. The geometric ID of an ANTI-0 counter is defined according to the equation

$$GeoID = 100 \times N_{Quad} + 10 \times N_{Row} + N_{Col}, \tag{4.3.1}$$

where the $N_{Quad}$, $N_{Row}$ and $N_{Col}$ are the quadrant, row and column numbers respectively. The quadrant numbers span $1, 2, 3, 4$, covering the $(x, y)$ plane quadrants starting from $x > 0$ and $y > 0$ and going clockwise. The rows and columns are counted from the center of the detector outwards within each quadrant, with the former counted along the vertical and the latter along the horizontal. This approach yields the pattern shown in Figure 4.4.

Given lack of light propagation simulation within ANTI-0 counters in NA62MC, simulation of the SiPMs and on-tile electronics was deemed unnecessary due to their small size. Instead, the focus was

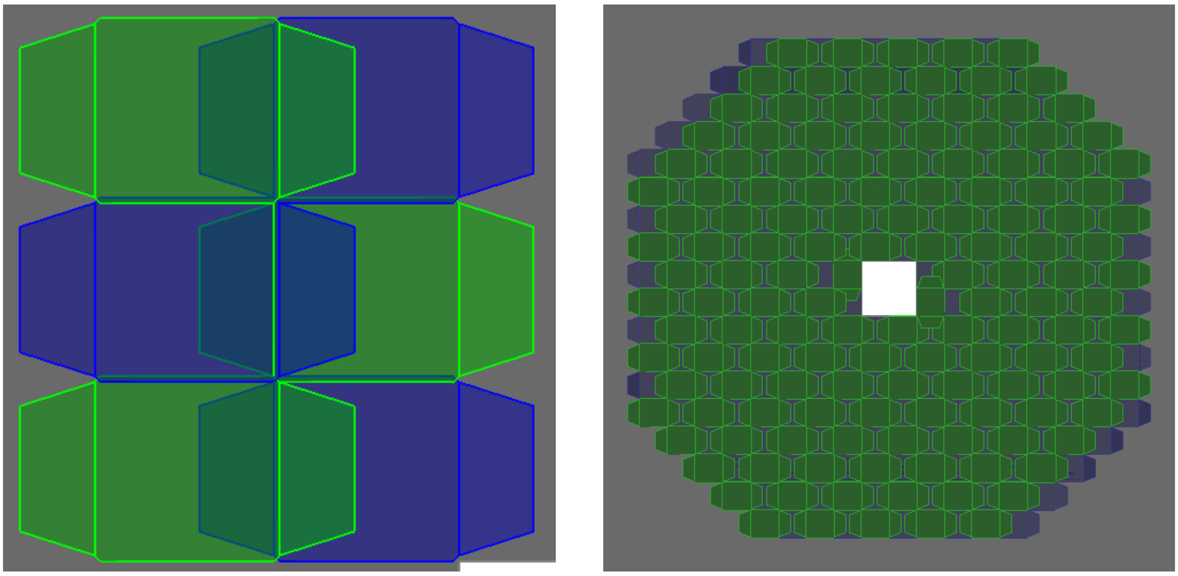

Figure 4.5: Visualisations of a small subset of ANTI-0 counters on the central support sheet (left) and the whole detector right). Both graphics were produced using NA62MC, with green tiles placed in front of the central sheet and blue ones behind.

placed on ensuring the correct geometry of the scintillator material and the inclusion of both lightguides and all three aluminum sheets (central support and two covers). This is critical to accurately model the scattering of upstream particles by the ANTI-0, which affects the particle properties as measured by the downstream detectors. The resultant visualisation of a small subset of simulated tiles is shown in the left panel of Figure 4.5, clearly showing the overlaps between neighbours on opposite sides of the support sheet, and the separation between scintillator and lightguide material of each tile. The choice of elements to be included in the simulation was motivated by the components that can be traversed by particles incident on the ANTI-0 and generate a signal in one of the counters, hence the frame supporting the detector shown in the right panel of Figure 4.2 was neglected. The geometry of the whole simulated detector as viewed from the direction of the incoming beam can be seen in the right panel of Figure 4.5.

### 4.3.2 ANTI-0 in NA62Reconstruction

As a simple charged-particle hodoscope with one readout channel per counter, the reconstruction algorithm of the ANTI-0 detector relies on central utilities contained within NA62Reconstruction, see Section 3.4.2. To enable identical processing of MC-generated and real data, the former must first be “digitised”, i.e. converted to the format of the latter with front-end electronics and readout chain effects emulated.

The digitisation algorithm used for the ANTI-0 is a four-step process, outlined below in order of application.

1. MC-level “hit” objects with a simulated energy deposit lower than a preset threshold are rejected to account for a minimum sensitivity of the physical readout chain. The threshold value is set at 1 MeV by scaling that used for the CHOD, another charged-particle hodoscope with a similar composition of the scintillator material (POPOP concentration of 0.3%), by the ratio of counter

thicknesses of 1/3.

2. The remaining hits are sorted in time for each counter separately, to allow for emulation of the readout dead time, $t_{Dead}$. For a CFD output signal of duration 17 ns, the ANTI-0 channel dead time is 47 ns [107] and time ordered hits within $t_{Dead}$ of previous one in the same counter are discarded.

3. The MC-generated time for the particle crossing, $t_{MC}$, is converted to include the effect of readout electronics and individual channel resolution, $t_{Digi}$. In particular,

$$t_{Digi} = t_{MC} + t_{fine} - t_{ToF} + t_{corr} + t_{channel\ T0} + \delta t|_{res}, \tag{4.3.2}$$

   where $t_{fine}$ and $t_{ToF}$ are the "fine" time of the event in units as defined by the clock period of the NA62 TDAQ system and the time of flight correction calculated based on detector z-position and assuming particles travel with velocity $c$ respectively. The $t_{corr}$ term includes corrections for modulation of the event "fine" time, drift of the trigger time and a central shift in time of all detector channels. To allow for independent alignment of individual channels, the $t_{channel\ T0}$ term is calculated from data as the mean of a Gaussian fit to the profile of channel time with respect to the event KTAG time. The per-channel correction is calculated for counters as identified by their readout number, i.e. the number of the slot of the TEL62 board responsible for processing ANTI-0 data, necessitating a mapping between geometric and readout ID. A map is provided in the form of a text file, which is handled by central na62fw utilities through a detector-specific "RawDecoder" class object. Finally, $\delta t|_{res}$ mimics the time resolution of a counter by injecting a random contribution sampled from a Gaussian of zero mean and width defined by Equation 4.2.1

4. The resultant $t_{Digi}$ is converted to an integer multiple of the TDAQ clock period and a check is made whether it falls within a pre-defined readout window comprising a fixed number of readout slots of clock period length.

Should the final condition be satisfied, a "digi" class object is created and added to the event, comprising the counter number and corrected particle crossing time.

For real data, "digi" objects within each event are created using central software infrastructure for processing data read out with TEL62 boards. The per-run timing corrections as applied to MC data through the $t_{corr}$ and $t_{channel\ T0}$ terms of Equation 4.3.2 are calculated after the first reconstruction round and are implemented automatically at later stages. Conversion between original readout and "digi"-level geometric counter ID is also handled by central methods.

The conversion of "digi" class objects to "candidates", i.e. final outputs of the reconstruction process, progresses through the common methods for real and simulated data. A "candidate" object includes a time value and geometric channel number, together with the position of the counter. To ensure efficient data storage, reconstructed data is stored in a "slim" format, made up of a subset of independent and irrecoverable variables for each detector system. The "slim candidates" for the ANTI-0 only include the timing and geometric ID information, with counter position automatically recomputed from the latter when reading the data for further processing.

Given the the lack of inter-dependence between different detectors under reconstruction, histograms monitoring the procedure allow for a quick low-level check of detector performance on a per-burst basis.

In the case of the ANTI-0, channel occupancy and time alignment are key diagnostic quantities. The former can be investigated in one dimension as a function of either geometric or readout ID, with both profiles including zero-population bins by design, or in two dimensions as a function of counter position, offering an insight into particle rates at the detector plane and geometric correlations between potential issues. Time alignment of the detector as a whole is verified by plotting time of all candidates with respect the KTAG event time, with per-channel corrections implemented from text files stored on the TDAQ system. While fine alignment is non-critical for systems not included in any trigger lines, a large offset for a subset of channels can result in data corruption due to a fixed number of readout slots defining the time boundaries of an NA62 event.

### 4.3.3 SpectrometerANTI0Association tool

To fulfill the design purpose of the ANTI-0 detector, i.e. identify particles coming from the upstream of the decay region and leaving an experimental signature in the acceptance of the NA62 detector, an algorithm matching downstream spectrometer (STRAW) tracks to ANTI-0 candidates is necessary. Only a small fraction of particles generating signal in the ANTI-0 are reconstructed as good quality STRAW tracks, as evident from the solid angle acceptance of the two systems with respect to the position of the T10 target and other potential sources of upstream particles within the K12 beam line. Consequently, using the whole detector as a veto would lead to significant selection inefficiencies due to accidental activity.

A general tool, *SpectrometerANTI0Association*, was created to enable simple yet configurable analysis-stage verification of whether a STRAW track has matching activity in the ANTI-0. The analyzer performs a spatial association between extrapolated spectrometer track positions and ANTI-0 candidates, without constraints in the time domain. The process of setting the bounds for a geometric association, which necessitates an understanding of all the relevant resolution effects, together with the algorithm itself are detailed in this section. The output of the association routine is appended to the "DownstreamTrack" class, designed to contain all signals due to the passage of a single charged particle through the detectors positioned downstream of the last station of the GTK, i.e. from CHANTI onwards.

In the absence of material between the STRAW and ANTI-0 detectors, the resolution on extrapolated track positions to the plane of the latter would depend only on the intrinsic angular and one-dimensional position resolutions of the former, parameterised as [62]

$$\begin{aligned} \sigma_{\Theta}(STRAW) &= \left(1 + \tfrac{50\ \mathrm{GeV}/c}{p}\right) \times 10^{-5}\ \mathrm{rad}, \\ \sigma_{x(y)}(STRAW) &= 130\ \mathrm{nm}, \end{aligned} \tag{4.3.3}$$

for a particle travelling with momentum $p$. In the na62fw, the propagation of tracks within the FV automatically accounts for the residual magnetic field due to the MNP33 spectrometer magnet, allowing this effect to be neglected at association stage. The effect of an angular normal distribution of width $\theta$ on position resolution as projected to a plane separated by a baseline $b$ from the projection origin is

$$\sigma_{x(y)} = sin(\theta) \times b. \tag{4.3.4}$$

Given the geometry of the NA62 detector, the maximum angle between a STRAW track and beam direction is $O(10^{-2})$ rad, allowing for the approximation

$$\sigma_{x(y)} \approx \theta \times b. \tag{4.3.5}$$

Hence, the angular and position terms describing the STRAW resolution can be combined. Equation 4.3.4 shows the proportionality between baseline length and position resolution, which motivated considering the ANTI-0 as a single plane as tile separation along the z-direction is three orders of magnitude smaller than the separation between the spectrometer and the detector.

Given the transverse radius of the ANTI-0 of ∼1 m and the detector position just upstream of the end cap of the decay vessel, there is a multitude of possible trajectories connecting the first STRAW chamber and the ANTI-0 based on the material intercepted on the way, see Figure 3.3 for a visual aid. The trajectory generating a signature akin to kaon decays within the decay vessel involves tracks crossing the beam axis and not intercepting any of the first eight LAV stations. A study conducted within na62fw utilising 3 million muons generated with the BDSim [98] halo simulation showed that $(70.0 \pm 1.1)\%$ of spectrometer-reconstructed muons fall into this category. Such particles, apart from the momentum-independent effect of STRAW resolution, are subject to multiple small angle scattering from traversing the decay vessel end cap. Other lines connecting the ANTI-0 and STRAW involve crossing either the active or passive material of the LAV stations, the decay vessel outer wall in the section of smaller diameter, the vertically oriented annulus connecting the two parts of the decay vessel and combinations thereof. Tracks traversing the last two objects are neglected, given the geometric discrepancy between them and beam kaon decay products. The remaining trajectories involve crossing a subset of the first eight LAV stations.

The effect of scattering of a beam of particles of charge magnitude $z$ in units of elementary charge, $e$, Lorentz factor $\beta$ and momentum $p$ traversing a medium of thickness $x$ in units of radiation length, $X_0$ can be approximated as a normal distribution of width $\Theta_0$, where [110]

$$\Theta_0(p) = \frac{13.6\ \text{MeV}}{\beta c p} z\sqrt{x}(1 + 0.038\ln{(xz^2/\beta^2)})\ \text{rad}. \tag{4.3.6}$$

For muon momenta over $5\,\text{GeV}/c$, typical for analysis-level tracks in NA62, one can approximate $\beta \approx 1$. By design, particles incident on any of the LAV stations will cross at least $27\,X_0$ of material, leading to significantly stronger scattering than that originating from crossing the thin decay vessel end cap. The impact is further exacerbated by a much longer baseline separating the source from the ANTI-0 plane, leading to the impossibility of backward projection of the precise trajectory of a track past the final point of contact with a LAV station. Hence, tracks are classified as having hit some of the LAV stations or not by extrapolation to the back face of all stations and the fronts of the boundary stations LAV5 and LAV8. If a particle position on the plane in question is less than three times the STRAW resolution away from the radial span of the LAV module, it is considered as having hit the LAV station.

The overall expected position resolution for STRAW tracks of the most prominent type, i.e. those firmly outside the acceptance of the LAV stations, is

$$\sigma_{x(y)}(\mathit{predicted}) = \Big(0.92 + \frac{39.5\ \text{GeV}/c}{p}\Big)\ \text{mm}, \tag{4.3.7}$$

where the momentum-independent STRAW resolution and scattering terms are added in quadrature

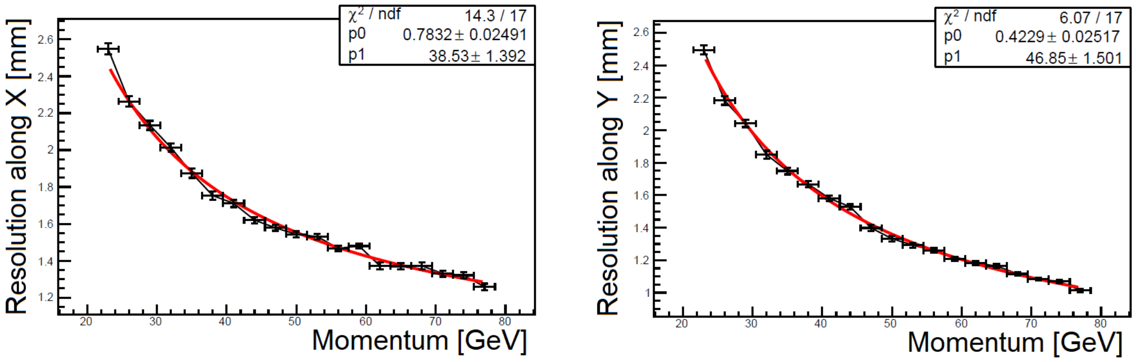

Figure 4.6: One-dimensional position resolutions of STRAW tracks not intercepting any of the LAV stations extrapolated to the plane of ANTI-0, as obtained by fitting the spectra of difference between true and reconstructed x- and y-positions in bins of momentum. Data used to generate the plots was simulated within NA62MC using a custom source of $\mu^+$ particles. Red lines show fits of the expected momentum-dependent model, with obtained parameter values presented in the legend.

under the assumption of no correlation. This model can be verified using MC-simulated data and utilising the existing functionality of saving particle positions at designated z-planes, often referred to as "true" information. Given a limited available sample of upstream particle events, a custom MC sample was produced. To cover all the possible trajectories involved in the STRAW-ANTI-0 matching, a large number of $\mu^+$ events was generated, with the particles injected uniformly from a plane covering the whole transverse profile of the ANTI-0, sampled from a uniform momentum distribution of (20 to 80) GeV/$c$ and a normal angular dispersion characterised by the width of 0.2 mrad. The differences between one-dimensional position along x and y-directions separately, $\delta_{x(y)}$ were extracted from the simulation,

$$\delta_{x(y)} = x(y)_{track} - x(y)_{true}, \tag{4.3.8}$$

where the "track" and "true" labels denote fully reconstructed and simulated values respectively. Profiles of $\delta_{x(y)}$ obtained in reconstructed track momentum, $p$, bins were fitted with Gaussian distributions. An initial fit on the entire observed range of scattering angles was used to limit the range of the second one to twice the initial width from the fitted centre. The fitted widths from the second iteration, together with a central value of the momentum bin in question were used to fill graphs for the x- and y-direction independently, as shown in Figure 4.6. Each graph was then fitted by a function of the same form as Equation 4.3.7, yielding the results for the orthogonal resolutions

$$\begin{aligned} \sigma_x(MC\,measured) &= \left([0.783 \pm 0.025] + \tfrac{[38.5\pm1.4]\ \mathrm{GeV}/c}{p}\right)\,\mathrm{mm} \\ \sigma_y(MC\,measured) &= \left([0.423 \pm 0.025] + \tfrac{[46.9\pm1.5]\ \mathrm{GeV}/c}{p}\right)\,\mathrm{mm}. \end{aligned} \tag{4.3.9}$$

The momentum independent terms of Equation 4.3.9 are not consistent with the prediction of Equation 4.3.7, given the the small fit uncertainties and the low $\chi^2/N_{DoF}$ values shown in Figure 4.6 implying an accurate model. The result obtained for the momentum-dependent term along the x-direction agrees with the prediction, while along the y-direction is significantly higher. For a typical analysis-level track of momentum of ∼20 GeV/$c$, the second term dominates. The discrepancies between the constant and momentum-dependent terms in Equation 4.3.9 for the two dimensions counterbalance one another, yielding 10% agreement for the two models for track momenta below 45 GeV/$c$. Hence, a simple average between the two spatial dimensions is taken for the formula defining STRAW-ANTI-0 matching resolution in a direction orthogonal to the z axis, $\sigma_r$, giving

$$\sigma_r = \left(0.60 + \frac{42.7\ \mathrm{GeV}/c}{p}\right)\ \mathrm{mm}. \tag{4.3.10}$$

With the resolution of the back projection of spectrometer tracks onto the ANTI-0 plane established, an ANTI-0 candidate is considered as geometrically compatible with the track if the projection to candidate distance, $D$ satisfies

$$D < 3 \times SR, \tag{4.3.11}$$

with $SR$ being the search radius defined from Equation 4.3.10 for tracks classified as not hitting any of the first eight LAV stations. The factor of 3 was chosen as a compromise between two competing phenomena: efficiency and impact of accidental activity.

While the tracks not intercepting LAV stations between ANTI-0 and STRAW are of primary importance for physics analyses in standard operating conditions, they illuminate only the inner part of the detector. Consequently, one must also implement an approach for particle trajectories crossing the LAV stations to allow for "dump mode" searches and verify the efficiency of outer ANTI-0 counters. The first approach to the problem relied on classification of tracks based on how many LAV stations they are back-projected through. The brief study performed to ascertain the fraction of upstream particle events not undergoing any scattering in the LAVs was also used to verify the accuracy of tagging which stations were traversed. The conclusion reinforced the expectation of impossibility of back projection past the last intercepted station, as mistagging was significant for all subcategories. Furthermore, no particular subset of crossed LAV stations was significantly more prevalent. As a result, all of the particle trajectories intercepting any LAV stations are considered jointly, with an analysis-level flag implemented to notify the user of whether a track satisfies this condition. The search radius for such trajectories, $SR_{LAV}$, was determined empirically with the use of the *ANTI0Efficiency* tool described in the following section. Two approaches were considered: a fixed value of 120 mm corresponding to the width of a single counter and a purely momentum-dependent form. The former proposition leads to checks being conducted in a fixed number of counters neighbouring the crossing point and gave a clear trend of increasing efficiency as a function of track momentum, as expected from the multiple small-angle scattering formula (Equation 4.3.6). The latter approach was hence chosen, with the numerical value of the parameter selected to achieve an efficiency of $>99.9\%$ in the momentum range (20 to 80) GeV/$c$, giving

$$SR_{LAV} = \frac{7500\ \mathrm{GeV}/c}{p}\ \mathrm{mm}. \tag{4.3.12}$$

Consequently, the maximum allowed projection to candidate distance for an average analysis level track is $\sim$1 m, leading to most of the detector being checked. This result served as a counter argument to utilising ANTI-0 information in the NA62 trigger system, as at L0 a significant effect is expected due to accidentals when the detector is used in veto mode.

### 4.3.4 ANTI0Efficiency tool

Quick and reliable methods for monitoring detector efficiency are a key requirement of ensuring stable data quality for long collection campaigns. The *ANTI0Efficiency* analyzer was designed for both near-online verification of the ANTI-0 performance as part of the NA62 "online monitor" system and to allow for categorisation of data by quality after the full reconstruction process. The output of the routine is also used to validate re-reconstruction of the data with improved software, whether on the side of na62fw or the software packages it relies on.

The analyser validates the performance of the *SpectrometerANTI0Association* algorithm on a subset of particle tracks selected to match the experimental signature of an upstream muon. The data chosen for this task comes from two minimum-bias trigger streams, requiring either a large number of RICH cells generating signal or a hit in the CHOD detector at hardware L0 level and no other conditions at the software level. Such a signature points to a presence of at least one charged particle incident on the downstream PID detectors. Each STRAW track within the event is then subject to the following set of requirements. First, the reconstructed track momentum must be in the range (5 to 100) GeV/$c$, with the bottom limit set by kaon decay kinematics and NA62 geometry, and the upper configurable at runtime to allow for higher momenta in beam dump mode. Only good quality spectrometer tracks, defined as having a value of $\chi^2 < 20$ from the STRAW reconstruction algorithm, are considered. The track must be within the geometric acceptance of the ANTI-0 detector, defined by the back projection onto the ANTI-0 plane. If a track is found to be less than a search radius value away from the boundaries of the simplified shape of the detector, i.e. with the step pattern in the corners replaced by a simple line running along the diagonal of counter active areas, it is not considered further. The lack of this requirement would inevitably lead to a lower measured efficiency of tiles on the outer edge of the detector, given the typical value of the search radius. When not considering dump mode data, the tracks are required to be geometrically inconsistent with a kaon decay occurring in the designated volume of the vacuum vessel, broadly defined as a cylinder spanning

$$Z \in (102, 183)\ \mathrm{m} \quad \text{and} \quad R < 50\ \mathrm{mm} \tag{4.3.13}$$

around the direction of the beam. The particle trajectory must be in the acceptance of the NA48-CHOD, LKR and MUV3 systems, to allow for later PID checks. Additionally, the track should be constructed from hits in all four STRAW stations. Track time, $t_{track}$ is defined as the time of a NA48-CHOD association and a CHOD association in the absence of the former, with the track rejected if neither is present. A timing cut of

$$|t_{track} - t_{trigger}| < 10\ \mathrm{ns} \tag{4.3.14}$$

is imposed, where $t_{trigger}$ is the trigger time, to ensure no readout window effects from all involved systems.

The candidate track must receive a positive muon identification verdict comprising two parts. The ratio of LKr energy deposit and reconstructed momentum must be consistent with a minimum-ionising-particle, so that

$$E_{LKr}/p_{STRAW} < 0.2, \tag{4.3.15}$$

where the LKr energy comes from a cluster up to 50 mm away from the track projected impact point and within 10 ns of $t_{track}$. The track is further required to have a MUV3 geometric association within 3 ns of $t_{track}$. Lastly, no KTAG candidates made of up $> 4$ sectors can be present within 2 ns of the track time, to ensure an early upstream origin of the track in question.

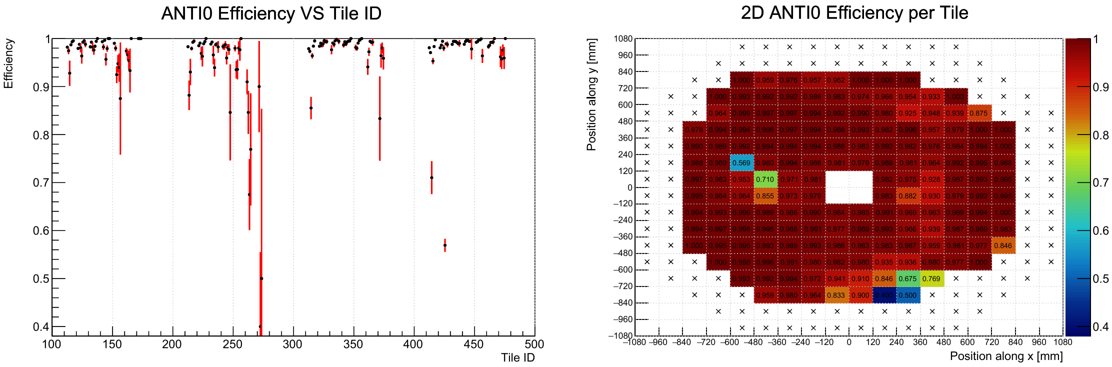

Figure 4.7: Plots produced by the *ANTI0Efficiency* analyser from run 14090 NA62 data collected in 2024. Left: per-counter efficiency as a function of geometric tile ID. Right: per-counter efficiency as a function of tile position on the ANTI-0 plane. Bins marked with ‘X’ contain counters, the efficiency of which cannot be determined due to large search radii of tracks pointing towards them. Tile positions can be correlated with geometric ID using Figure 4.4.

A geometric tile ID is then defined based on the extrapolated position of the track in the ANTI-0 plane, with overlaps neglected in favour of a simplified $120 \times 120\,\text{mm}^2$ square counter geometry. An expected hit is then scored for the counter and momentum in question. If any geometric ANTI-0 associations are present for the selected track, the one closest in time is chosen. Timing of the ANTI-0 response is checked with respect to the track time, requiring 10 ns agreement. This quantity is also monitored through a histogram separately for the NA48-CHOD and CHOD times, allowing later checks of ANTI-0 timing performance. The matched hit is finally scored for the counter and momentum as defined by the STRAW track projection impact point, irrespective of the counter of origin of the association. Note that the tracks classified as not having intercepted any of the LAV stations have search radii below 20 mm (per Equation 4.3.10), so that only direct hits or ones from neighbouring tiles in case of an impact point close to the tile edge satisfy the association criterion. For trajectories intercepting the LAV stations, the allowed search radii range from 225 mm to a few meters, corresponding to checking for signal in all eight neighbouring tiles and the whole detector, respectively. Consequently, neighbouring tiles contribute to the measured efficiency of each other, especially in the case of tracks classified as having passed through some of the LAV stations. This phenomenon allows an indirect measurement of the efficiency of tiles at the outer edge of the detector. The distances between the centers of those tiles and the detector outer edge are always smaller than the search radii of tracks extrapolated to them, preventing a direct measurement of their efficiency.

The *ANTI0Efficiency* analyser is run in two stages, where the first iteration determines the number of expected and matched hits, while the other computes the efficiencies, produces a PDF report containing a selection of plots and generates a list of “bad” bursts according to a criterion specified below. The uncertainties on all efficiency values, $\eta$, are computed from from the binomial formula for $N$ attempts, namely

$$\sigma_\eta = \sqrt{\eta(1-\eta)/N}. \tag{4.3.16}$$

The second stage of the analyzer is applied for every collected run. Apart from monitoring efficiency as a function of tile ID and position on the ANTI-0 plane, checks against burst number and timestamp value within the event are also performed. In the former case, the overall detector efficiency for each burst is computed and compared against a threshold value of

$$\eta_{threshold} = 0.95 \tag{4.3.17}$$

to determine whether the burst should be labelled as “bad” for the ANTI-0. A record of all systems with poor data quality in each burst is kept in per-run text files, with analysis-level functionality allowing to neglect bad bursts from a chosen set of systems. The check against the timestamp, i.e. the time within a burst, is performed to see the potential impact of inter-spill intensity fluctuations.

Typical histograms of per-counter ANTI-0 efficiency, as taken from the full processing of run 14090 (collected in 2024), are shown in Figure 4.7. Note the outer tiles marked with ‘X’ in the right panel of the figure, representing the counters where efficiency cannot be calculated due to the extrapolated impact points being less than $SR$ away from the detector edge for all considered tracks. The shape of the empty outer ring is not symmetrical around the centre of the detector, indirectly describing the upstream halo. The two regions of $< 0.9$ efficiency in the right panel of Figure 4.7 can be correlated with points on the left panel through the mapping contained in Figure 4.4, which shows the cluster to the bottom right of the detector is most likely an artifact of low statistics. The feature to the left of the beam pipe hole is a known effect of low efficiency of the tile with geometric ID 425 [111].

## 4.4 Data quality throughout 2021 - 2023

For short-term data quality verification, the output of the *ANTI0Efficiency* analyser is monitored on a per-run basis, with the analyser being a part of the standard NA62 processing routine. Longer period verification was performed by the author (serving as the data-quality responsible of the system) after the conclusion of a yearly data collection campaign and periodically within it, ensuring stable detector performance.

Data shown in this chapter was obtained by manipulating the run-level output of *ANTI0Efficiency*. In particular, all efficiency values were recomputed from the sums of expected and matched hits, with errors determined from Equation 4.3.16. To assess the timing performance of the detector, one-dimensional spectra of the difference between NA48-CHOD track times and the closest-in-time ANTI-0 association were fitted with a Gaussian distribution in the range $(-10 \text{ to } 10)\,\text{ns}$, with the resultant width taken as the relative resolution of the systems, provided the presence of at least 1000 entries in the histogram.

### 4.4.1 Data quality in 2021

The 2021 NA62 data-collection campaign began in July, with the first run with quality sufficient for physics analyses collected in the second half of August. The experimental apparatus was switched back on after a three-year break, with newly added components, including the ANTI-0, as described in Section 3.2.12.

The efficiency of the ANTI-0 detector as a function of run number for 2021 data designated as analysis quality is shown in the top panel of Figure 4.8. Three periods with distinct trends can be observed: the initial decrease in performance until run 10900, a block of more stable yet much lower efficiency up to run 11050 and steady design performance from run 11090 onwards. The first feature

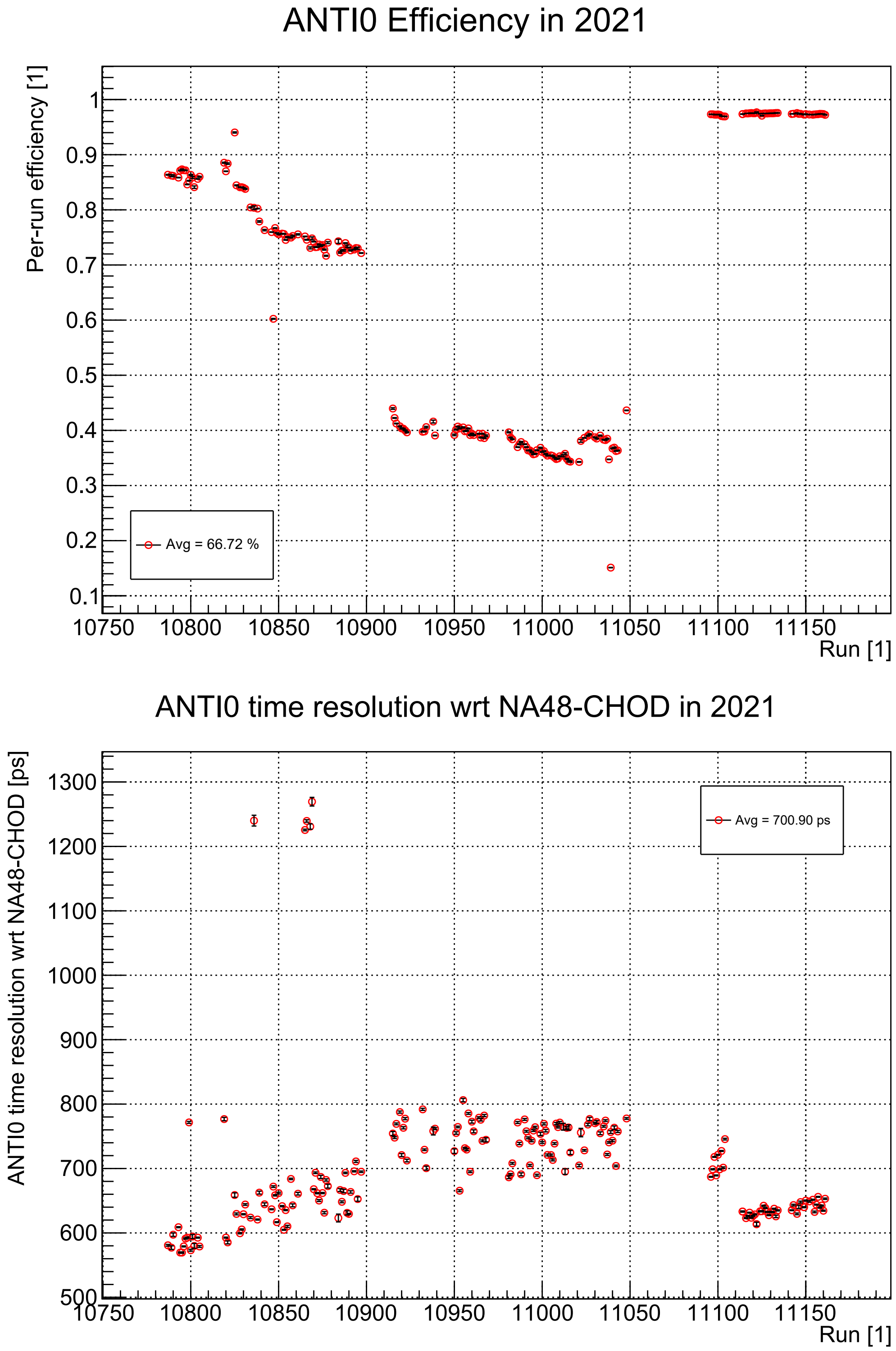

Figure 4.8: Average per-run efficiency (top) and time resolution (bottom) of the ANTI-0 detector in 2021. The latter was computed from ANTI-0 candidates associated with downstream tracks, which have a NA48-CHOD time.The yearly averages presented in the insets were calculated as weighted means, including per-run uncertainties.

| Sample | First Run | Last Run | $N_{Bursts}$ [$10^3$] | ANTI-0 bad burst fraction [%] |
|---|---|---|---|---|
| A | 11096 | 11161 | 42 | 0.97 |
| B | 11000 | 11048 | 27 | 100 |
| C | 10915 | 10999 | 34 | 100 |
| D | 10885 | 10897 | 6.6 | 100 |
| E | 10787 | 10884 | 35 | 100 |

Table 4.1: Bad bursts of the ANTI-0 detector per NA62 data sample for all samples collected in 2021.

corresponds to a period of significant TDAQ instability and variation in instantaneous beam intensity. The period following run 10910 sees a step-like drop in efficiency, which is correlated to lowering the bias voltage of all SiPMs by $-0.5\,\mathrm{V}$ and increasing the voltage supplied to all amplifiers from $6.8\,\mathrm{V}$ to $7.5\,\mathrm{V}$. This action was a part of detector commissioning, with the operational parameters varied to see the impact on detector performance. The subsequent gap spanning runs 11050 to 11090 covers a period of dump mode data collection. The small increase in efficiency visible around run 11030 corresponds to an intervention on 6 of the 18 CFD modules reading out the detector. The procedure of adjusting the CFD threshold and walk used in the devices was completed during dump mode operation. The final period of stable and high efficiency from run 11090 onwards depicts the true capability of the ANTI-0, with fine-tuned operational parameters.

The timing capability of the detector with respect to the NA48-CHOD, together with its variation throughout the year, is shown in the bottom panel of Figure 4.8. The distinct periods observed in ANTI-0 efficiency are reflected in the timing performance. The resolution width increases in the first period, and stabilises in the second and third one. The decrease observed around run 11105 is correlated to updating the online timing corrections for all ANTI-0 channels based on data from run 11100. Note that the outlier points of the top and bottom panels of Figure 4.8 are distinct, pointing towards independent causes of temporary inefficiency and poor timing performance. Overall, the measured time resolution of ANTI-0 associations produced by the *SpectrometerANTI0Association* algorithm with respect to the NA48-CHOD is significantly worse than that obtained for individual counters prior to installation (Equation 4.2.1), even accounting for the reference detector resolution of ∼200 ps. While the fitting procedure applied to *ANTI0Efficiency* output was not optimised, individual fits describe the resolution to ∼10%. Hence the origin of the observed time resolution discrepancy remains to be investigated.

The performance of the ANTI-0 detector as parameterised by fraction of "bad" bursts in each of the 2021 data samples is summarised in Table 4.1. Note that the samples are labelled anti-chronologically, with 2021E comprising the first runs collected in 2021. All bursts collected for samples B to E are designated as bad, reflecting the ANTI-0 efficiency trend of the top panel of Figure 4.8. In the period characterised by design performance (sample 2021A), only ∼1% of bursts do not meet the data quality criterion.

### 4.4.2 Data quality in 2022

The per-run efficiency of the ANTI-0 detector for all physics-quality runs collected in 2022 is shown in the top panel of Figure 4.9. Four data-taking periods with a significant deviation from the stable detector efficiency of ∼98% can be identified. The first one spans runs (11 840 to 11 992) , with the

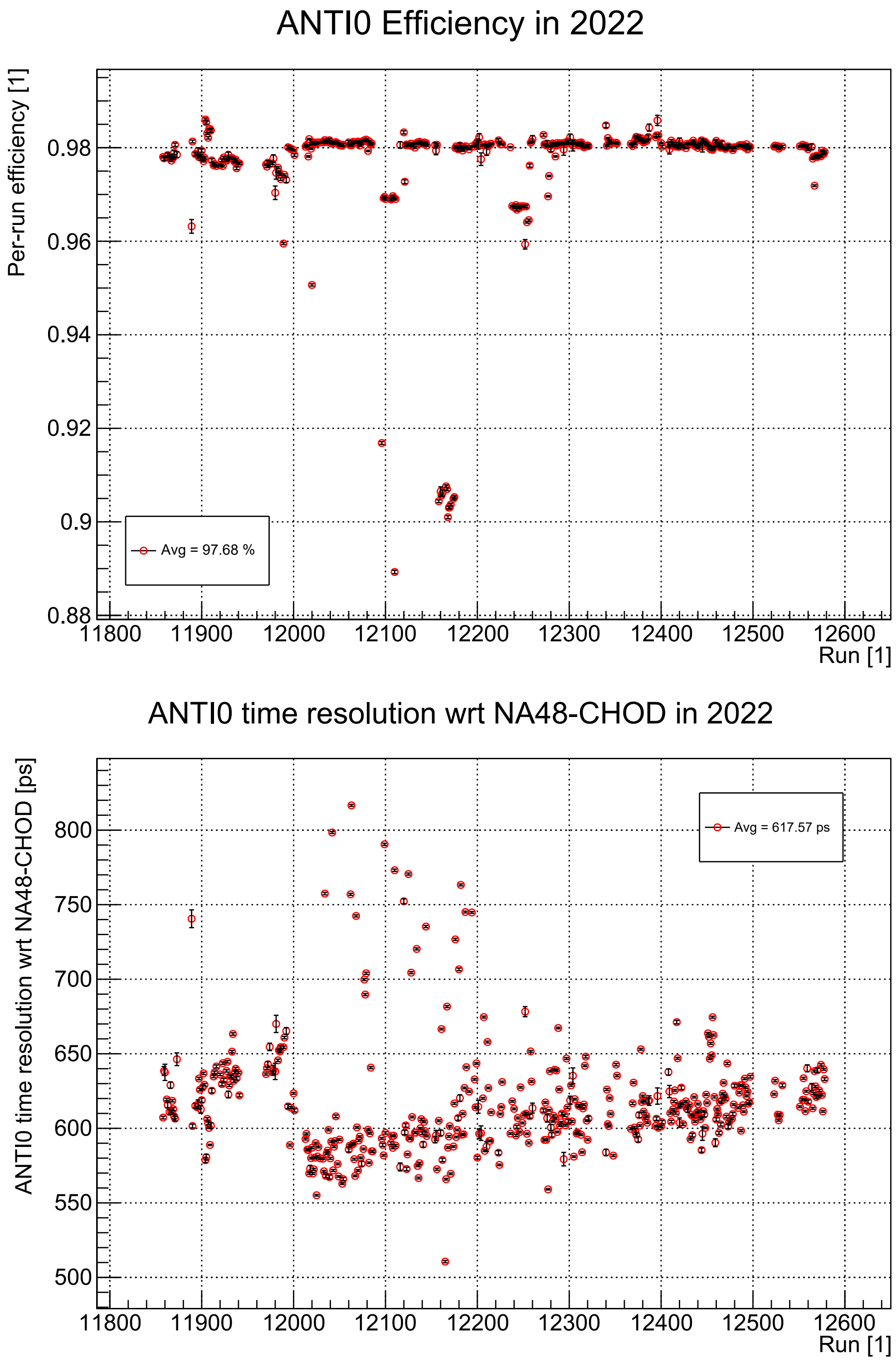

Figure 4.9: Average per-run efficiency (top) and time resolution (bottom) of the ANTI-0 detector in 2022. The latter was computed from ANTI-0 candidates associated with downstream tracks, which have a NA48-CHOD time. The yearly averages presented in the insets were calculated as weighted means, including per-run uncertainties.

| Sample | First Run | Last Run | $N_{Bursts}$ [$10^3$] | ANTI-0 bad burst fraction [%] |
|---|---|---|---|---|
| A | 11858 | 12001 | 49 | 0.60 |
| B | 12013 | 12162 | 108 | 4.62 |
| C | 12165 | 12321 | 110 | 10.40 |
| D | 12340 | 12463 | 78 | 0.19 |
| E | 12464 | 12578 | 58 | 0.26 |

Table 4.2: Bad bursts of the ANTI-0 detector per NA62 data sample for all samples collected in 2022.

initial period affected by general TDAQ and beam quality instabilities during calibration of all detector systems. The end of the period coincides with an increase of the bias voltage supplied to ANTI-0 SiPMs by 0.5 V. The second medium-term decrease in ANTI-0 efficiency occurred for runs (12 095 to 12 115). It was caused by a failure of one of low voltage cards powering the pre-amplifiers, resulting in a loss of signal from a fraction of channels. The third period of reduced ANTI-0 efficiency, characterised by the largest steady drop of the year, covers runs (12 157 to 12 175), as visible in the top panel of Figure 4.9. The underlying issue was the repeated tripping of a group of ANTI-0 channels due to mid-burst current spikes in the SiPMs. The trip thresholds for the affected channels were increased to reflect the rising dark current caused by radiation exposure. Another efficiency drop of the same physical origin occurring for runs (12 240 to 12 260) motivated a further increase of the trip thresholds of all ANTI-0 channels.

The per-run timing performance of the ANTI-0 in 2022, quantified through the resolution relative to NA48-CHOD, is shown in the bottom panel of Figure 4.9. The measured performance agrees with that observed in 2021, with only a single deviation from the general trend of worsening resolution due to ageing, potentially caused by radiation exposure. The step-like change occurring around run 12000 corresponds to the increase in SiPM bias voltages described in the previous paragraph. Note that the yearly rate of worsening timing performance (a few tens of ps) has no impact on the quality of data from analysis perspective, where the timing window size is typically a few ns.

The performance of the ANTI-0 as parameterised by fraction of “bad” bursts in each of the 2022 data samples is summarised in Table 4.2. The observed pattern is caused by the final three lower efficiency periods visible in the top panel of Figure 4.9, with one contained in sample 2021B and two in 2021C. The stability of ANTI-0 performance in 2022 is demonstrated by the sub-percent fraction of bad bursts observed in the absence of hardware issues.

### 4.4.3 Data quality in 2023

The per-run efficiency and timing resolution of the ANTI-0 detector for all physics-quality runs collected in 2023 is shown in the top and bottom panels of Figure 4.10 respectively. The 2023 data-collection campaign was characterised by stable performance of the detector. The gap spanning runs (13 416 to 13 471) corresponds to dump mode operation, with a single kaon run taken in the middle to provide calibration data for a subset of detector systems. The nominal NA62 beam intensity was reduced by factor 1/3 from run 13523, as motivated by studies of $K^+ \to \pi^+\nu\bar{\nu}$ and $K^+ \to \pi^+\pi^0$ candidate event yields as a function of beam intensity [112]. While no associated change in timing performance of the ANTI-0 was observed, the per-run efficiency of the detector improved to ∼98.3%.

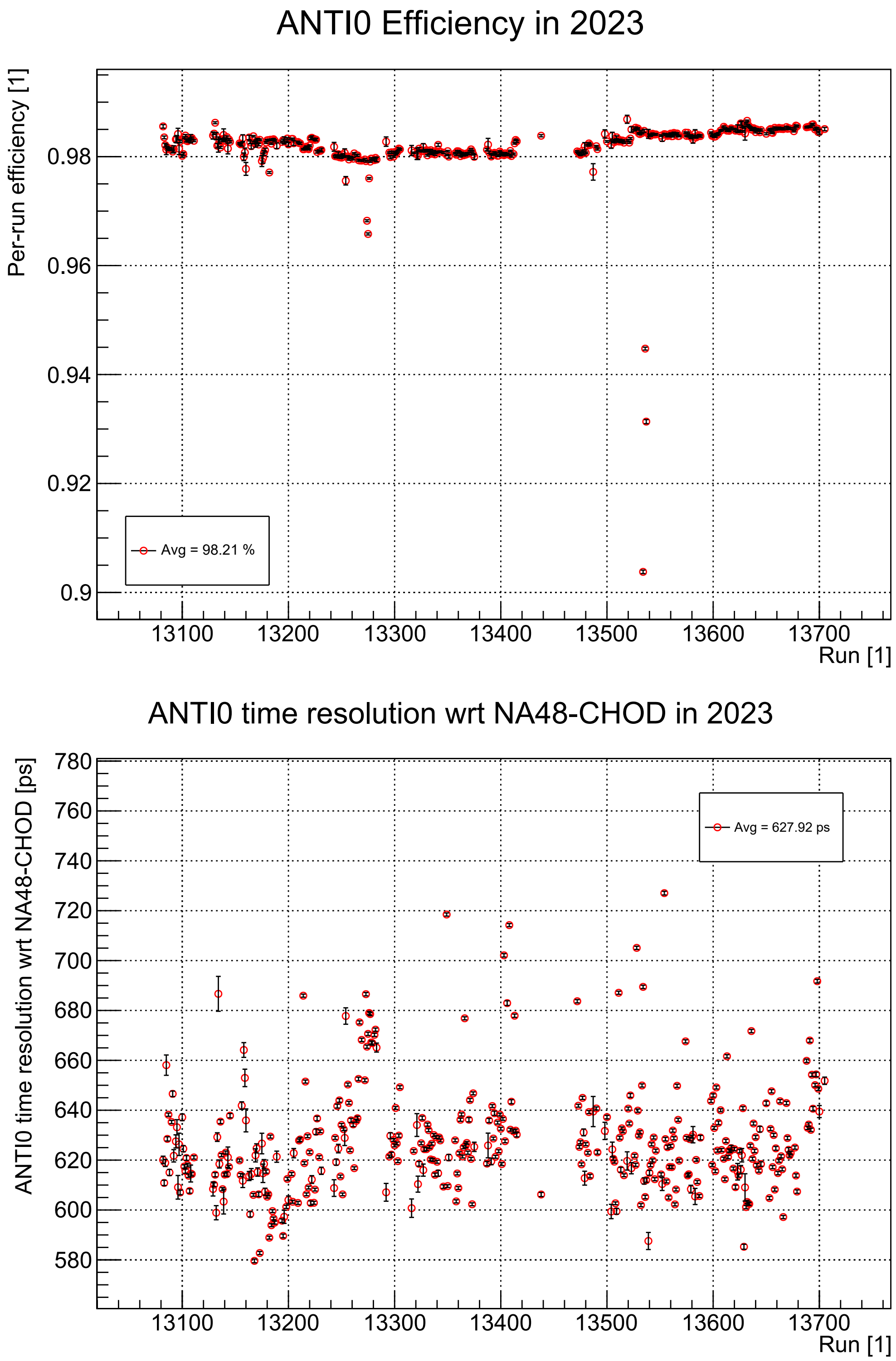

Figure 4.10: Average per-run efficiency (top) and time resolution (bottom) of the ANTI-0 detector in 2023. The latter was computed from ANTI-0 candidates associated with downstream tracks, which have a NA48-CHOD time. The yearly averages presented in the insets were calculated as weighted means, including per-run uncertainties.

| Sample | First Run | Last Run | $N_{Bursts}$ $[10^3]$ | ANTI-0 bad burst fraction [%] |
|---|---|---|---|---|
| A | 13082 | 13205 | 60 | 0.77 |
| B | 13206 | 13283 | 58 | 0.22 |
| C | 13284 | 13415 | 90 | 0.11 |
| D | 13438 | 13522 | 24 | 0.08 |
| E | 13523 | 13621 | 88 | 2.25 |
| F | 13623 | 13705 | 68 | 0.07 |

Table 4.3: Bad bursts of the ANTI-0 detector per NA62 data sample for all samples collected in 2023.

The performance of the ANTI-0 as parameterised by fraction of "bad" bursts in each of the 2023 data samples is summarised in Table 4.3. Only sample 2021E contains a bad burst fraction >1%. Overall, data collected in 2023 showcases the long-term ANTI-0 performance with efficiency exceeding 98% and a time resolution with respect to the NA48-CHOD of 630 ps. Subtracting the NA48-CHOD resolution contribution of 200 ps, time resolution of the ANTI-0 is calculated to be 600 ps.

# Chapter 5

# The $K^+ \to \mu^+\nu_\mu\mu^+\mu^-$ Analysis

This chapter contains the description of work conducted to measure the branching ratio of the $K^+ \to \mu^+\nu_\mu\mu^+\mu^-$ decay on NA62 data collected in 2017 and 2018. The analysis strategy, data sample and employed event selections are outlined, together with the techniques used for background modelling. The chapter includes a discussion of the most relevant systematic effects and concludes with the resultant measurement of the branching ratio $\mathfrak{B}(K^+ \to \mu^+\nu_\mu\mu^+\mu^-)$ together with an error budget.

## 5.1 Strategy

The target of the analysis is a measurement of the branching fraction of the $K^+ \to \mu^+\nu_\mu\mu^+\mu^-$ ($K_{\mu\nu\mu\mu}$) decay by using the $K^+ \to \pi^+\mu^+\mu^-$ ($K_{\pi\mu\mu}$) decay to quantify the number of $K^+$ decays in the FV, i.e. as a normalisation channel. This approach is motivated by two key arguments. Firstly, the signal and normalisation channels share a similar experimental signature with a single incoming $K^+$ and three tracks in the downstream region, at least two of which are due to muons. Secondly, data pertinent to both decays is collected with the same trigger stream at the NA62 Experiment. These two features allow for a partial cancellation of systematic effects due to offline selection and the trigger system. The immediate consequence of using $K_{\pi\mu\mu}$ as the normalisation channel is the external uncertainty coming from the branching fraction of the decay (later referred to as $\mathfrak{B}_{\pi\mu\mu}$), recently measured as [2]

$$\mathfrak{B}(K^+ \to \pi^+\mu^+\mu^-) = (9.15 \pm 0.08) \times 10^{-8} \tag{5.1.1}$$

by the NA62 Collaboration on a data set including the one used for the $K_{\mu\nu\mu\mu}$ analysis. The most significant source of uncertainty in the $K_{\pi\mu\mu}$ measurement originates from data sample size. Given the lower expected branching ratio of the $K_{\mu\nu\mu\mu}$ decay (see Equation 2.4.15) and a similar size of the data set used as compared to that of the $K_{\pi\mu\mu}$ analysis, the signal selection was initially designed to maximise signal acceptance. Further selection optimisation was performed to minimise the uncertainties arising from the number of signal candidates in data, the expected background contamination and the method of obtaining the background estimate.

Throughout the analysis, selection acceptances by convention include the associated trigger efficiencies. This treatment is enabled by the existence of L0 (hardware) trigger emulators and the possibility to apply the HLT (L1 software trigger) algorithms offline to simulated data. The systematic effects arising from imperfections in this approach are discussed in Section 5.8.

### 5.1.1 Branching ratio measurement

The measurement of $\mathfrak{B}(K^+ \to \mu^+\nu_\mu\mu^+\mu^-)$ (later referred to as $\mathfrak{B}_{\mu\nu\mu\mu}$) relies on counting the data events passing the full signal selection, $N_{Data}$ and subtracting the expected background contamination, $N_{Bkgd}$ as estimated with the MC samples of different $K^+$ decay modes, so that

$$\mathfrak{B}(K^+ \to \mu^+\nu_\mu\mu^+\mu^-) = \frac{N_{Data} - N_{Bkgd}}{A_{\mu\nu\mu\mu} \times N_K}. \tag{5.1.2}$$

The $A_{\mu\nu\mu\mu}$ symbol represents the acceptance of the $K_{\mu\nu\mu\mu}$ decay under the signal selection including the trigger efficiency. It is computed from a MC sample as the fraction of events passing the full selection with respect to the total number of decays of this type occurring with true decay z-position such that

$$Z_{vtx}^{true} \in [105.0, 180.0] \text{ m}, \tag{5.1.3}$$

defining the conventional range for all acceptance calculations unless specified otherwise. The MC generator used for calculation of $A_{\mu\nu\mu\mu}$, included in na62fw and following the theoretical description contained in Section 2.4.2, was provided by the author of the paper giving the Standard Model prediction for $\mathfrak{B}_{\mu\nu\mu\mu}$ [10]. The $N_K$ symbol represents the number of $K^+$ decays in the FV for the considered data sample. The quantity is measured with the $K_{\pi\mu\mu}$ decay, so that

$$N_K = \frac{N_{Cand}^{\pi\mu\mu}}{A_{\pi\mu\mu}^{Norm} \times \mathfrak{B}_{\pi\mu\mu}}, \tag{5.1.4}$$

where $N_{Cand}^{\pi\mu\mu}$ is the number of background-subtracted $K_{\pi\mu\mu}$ data events and $A_{\pi\mu\mu}^{Norm}$ is the acceptance of $K^+ \to \pi^+\mu^+\mu^-$ events under the normalisation selection including the trigger efficiency. Finally, the expected background contamination in the signal mode, $N_{Bkgd}$ is the sum of MC contributions from individual $K^+$ decay modes other than the signal. Explicitly,

$$N_{Bkgd} = \sum_{i \in MC} \frac{N_i}{N_{Sample}^i} \times \mathfrak{B}_i \times N_K, \tag{5.1.5}$$

where $N_i$ is the numbers of events passing the full signal selection including trigger emulation, $N_{Sample}^i$ quantifies the number of simulated events with the true decay z-position satisfying Equation 5.1.3, $\mathfrak{B}_i$ is the branching ratio and the index $i$ covers the relevant MC samples.

The reliability of $A_{\mu\nu\mu\mu}$ and $A_{\pi\mu\mu}^{Norm}$ estimates from MC simulation is supported by the parts of the simulation being tuned to real data, the inclusion of pileup event signatures prior to reconstruction (see Section 3.4.2) and subjecting real and simulated data to the same reconstruction routines. Furthermore, the similar experimental signature of the signal and normalisation channels should result in partial cancellation of systematic effects due to imperfect simulation of detector response. The uncertainty arising from using the MC estimate for $N_{Bkgd}$ is addressed and quantified in Section 5.7.2.

### 5.1.2 Error propagation

The formulae from the previous subsection define the full spectrum of observable variables and key quantities necessary for the computation of the target branching ratio. The uncertainties on individual

| Variable, $j$ | $\frac{\partial \mathfrak{B}_{\mu\nu\mu\mu}}{\partial j}$ | Uncertainty type |
|---|---|---|
| $N_{Data}$ | $\frac{\mathfrak{B}^{BF}_{\mu\nu\mu\mu}}{N_{Data}}$ | Data statistical |
| $A_{\mu\nu\mu\mu}$ | $-\frac{\mathfrak{B}_{\mu\nu\mu\mu}}{A_{\mu\nu\mu\mu}}$ | MC statistical |
| $N^{\pi\mu\mu}_{Cand}$ | $-\frac{\mathfrak{B}^{BF}_{\mu\nu\mu\mu}}{N^{\pi\mu\mu}_{Cand}}$ | Systematic |
| $A^{Norm}_{\pi\mu\mu}$ | $\frac{\mathfrak{B}^{BF}_{\mu\nu\mu\mu}}{A^{Norm}_{\pi\mu\mu}}$ | Systematic |
| $N_i$ | $\frac{C_i}{N_i}$ | Systematic |
| $\mathfrak{B}_i$ | $\delta^{\pi\mu\mu}_i \frac{\mathfrak{B}^{BF}_{\mu\nu\mu\mu}}{\mathfrak{B}_i} - \frac{C_i}{\mathfrak{B}_i}$ | External |

Table 5.1: Partial derivatives of $\mathfrak{B}_{\mu\nu\mu\mu}$ with respect to a complete set of key analysis variables used for error propagation. The $\delta^{\pi\mu\mu}_i$ symbol is a Kronecker delta evaluated to 1 if the sample in question is $K_{\pi\mu\mu}$ and 0 otherwise.

quantities are combined to provide the error on $\mathfrak{B}_{\mu\nu\mu\mu}$ according to the formula

$$\sigma(\mathfrak{B}_{\mu\nu\mu\mu}) = \sqrt{\sum_j \Big( \frac{\partial \mathfrak{B}_{\mu\nu\mu\mu}}{\partial j} \times \sigma_j \Big)^2}, \tag{5.1.6}$$

where the index $j$ runs over all observable variables and key quantities with uncertainties $\sigma_j$. The procedure is applied separately for statistical, systematic and external uncertainty sources, under the assumption of contributions from individual variables being uncorrelated. Correlations between the considered sources of uncertainty are neglected due to their expected small contribution in view of a dominant effect arising from data sample size.

The calculation is simplified by a reformulation of Equation 5.1.2 using Equations 5.1.4 and 5.1.5, yielding

$$\begin{aligned} \mathfrak{B}_{\mu\nu\mu\mu} &= \frac{N_{Data} \times A^{Norm}_{\pi\mu\mu}}{A_{\mu\nu\mu\mu} \times N^{\pi\mu\mu}_{Cand}} \times \mathfrak{B}_{\pi\mu\mu} - \sum_{i\in MC} \frac{N_i}{A_{\mu\nu\mu\mu} \times N_K} \times \frac{N_K \times \mathfrak{B}_i}{N^i_{Sample}} \\ &= \mathfrak{B}^{BF}_{\mu\nu\mu\mu} - \sum_{i\in MC} \frac{N_i \times \mathfrak{B}_i}{A_{\mu\nu\mu\mu} \times N^i_{Sample}} = \mathfrak{B}^{BF}_{\mu\nu\mu\mu} - \sum_{i\in MC} C_i, \end{aligned} \tag{5.1.7}$$

where $\mathfrak{B}^{BF}_{\mu\nu\mu\mu}$ is a background-free-like formulation of Equation 5.1.2, i.e. describing the branching ratio for the case $N_{Bkgd} = 0$. The $C_i$ symbol represents the correction to $\mathfrak{B}_{\mu\nu\mu\mu}$ from background contribution of mode $i$, with $i$ spanning the set of used MC samples.

The partial derivatives of $\mathfrak{B}_{\mu\nu\mu\mu}$ with respect to a key set of analysis variables are presented in Table 5.1, together with their classification as either statistical, systematic or external uncertainty. Data and MC statistical error for the signal channel are classified as statistical uncertainty, where the latter follows Reference [113] and is motivated by lack of an alternative method for estimating the parameter. The corresponding variables for the normalisation channel are treated as systematic uncertainty due to the method of measuring the number of $K^+$ decays in the FV. Error propagation for individual quantities, such as $N_K$ or $N_{Bkgd}$, follows the same principles.

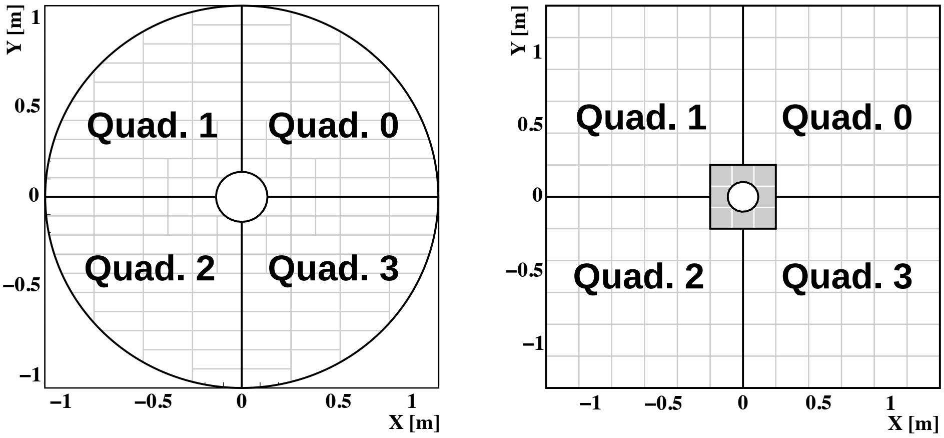

Figure 5.1: The definitions of quadrants of the CHOD and MUV3 detectors as a function of tile position, left and right respectively. The grey region of the MUV3 corresponds to the nine small "inner" tiles, not belonging to any quadrant, with the larger tiles outside of this region known as "outer". [90]

While this section discusses all sources of statistical and external uncertainties, the coverage of systematic effects is limited to phenomena of statistical nature arising from the use of $K_{\pi\mu\mu}$ as a normalisation channel and MC samples as a method for estimating $N_{Bkgd}$. The impact of other systematic effects, quantified after optimising the event selections as described in Section 5.6, is detailed in Section 5.7.2.

## 5.2 Data Sample

The analysis sample comprises all data collected by the NA62 Collaboration with the di-muon multi-track ($2\mu$MT) trigger stream in 2017 and 2018 and selected by the "2MU3TV" offline data filter. The data is subject to standard performance requirements for all systems involved in online collection and offline processing of the data, as well as for data quality of the detector systems used in the selection process.

### 5.2.1 $2\mu$MT trigger stream

The di-muon multi-track trigger stream was designed to indicate the presence of events with at least two final state muons due to a $K^+$ decay producing multiple charged tracks.

At the L0 hardware level, the stream requires a coincidence of three conditions, called "RICH", "QX" and "MO2". The first one denotes at least two signals seen by the RICH, with the L0 trigger time defined by the time of this primitive. The "QX" condition requires at least one signal from each of a pair of diagonally opposed quadrants of the CHOD detector, as shown in the left panel of Figure 5.1. This trigger condition reduces the accidental contribution to the trigger bandwidth, as charged daughters of a single $K^+$ preferentially illuminate opposite CHOD quadrants by momentum conservation. The "MO2" condition requires at least two hits in the "outer" tiles of the MUV3 detector, as defined in the right panel of Figure 5.1. Such a signature implies the presence of muons in the downstream part of the detector, with only the "outer" part of the detector used due to significant illumination of the "inner" section by $\pi^{\pm} \to \mu^{\pm}\nu$ decays occurring downstream of the FV.

After a positive decision at the L0 level, two L1 software trigger algorithms are applied, "KTAG" and "STRAW-Exo". The former algorithm utilises information from the KTAG, requesting at least one detected Cherenkov photon in more than four octants of the detector within 5 ns of the L0 trigger time. It serves to reject events triggered by scattered beam pions or halo muons, with the time window significantly larger than the KTAG time resolution to accommodate for potential drifts in the readout system. The "STRAW-Exo" algorithm imposes a requirement on a set of downstream spectrometer tracks obtained with a faster and simpler reconstruction procedure than the full offline treatment. The algorithm returns a positive decision if a negatively charged track, satisfying a set of quality conditions designed to reduced the presence of fake tracks, is found.

A detailed discussion of the performance of individual components of the $2\mu$MT trigger line as measured on 2018 data is available in [90].

### 5.2.2 2MU3TV data filter

The NA62 software framework contains "filters", i.e. analysis level tools used for broad classification of individual events according to their general properties. Each "filter" applies a few cuts to data collected through a particular set of trigger lines to select events with similar final state signatures. The "filters" are not exclusive, i.e. a single event can bear multiple positive classifications.

The Di-muon Three Track Vertex (2MU3TV) filter was developed to facilitate analyses of kaon decays with three charged tracks, two of which are muons, such as the normalisation mode $K_{\pi\mu\mu}$ and the signal $K_{\mu\nu\mu\mu}$. The 2MU3TV filter accepts events with positive decisions from either the $2\mu$MT, "Multitrack" or "Control" streams. The "Multitrack" targets $K^+$ decays with multiple charged final state particles and the latter requires at least one charged particle generating a signal in the NA48-CHOD. The event is requested to contain at least one Spectrometer track vertex satisfying a set of conditions outlined below. Individual vertices are computed from Spectrometer tracks using the Billoir-Fruhwirth-Regler formulation of the least-squares fitting method [114] accounting for a non-uniform magnetic field. The candidate should:

1. be composed of three tracks;
2. consist of tracks within geometric acceptance of all four Spectrometer stations and separated by at least 10 mm at the STRAW1 plane;
3. have a vertex z-position in the range (103 to 180) m;
4. have a vertex $\chi^2 < 40$, as defined by the track fitting procedure;
5. have a total momentum below 90 GeV/$c$.

The final criterion requires that at least two tracks have geometric associations with candidates from the MUV3.

### 5.2.3 Data quality requirements

To ensure only data of good quality is processed for analysis purposes, satisfactory performance of individual detector systems as well as the data gathering and processing infrastructure is requested on a per-burst basis. This is monitored through the centrally developed "bad burst" system. All detector systems have automatically executed analysis-level routines, such as the one designed for the

ANTI-0 and described in Sector 4.3.4, which can flag a burst as “bad” for the system based on a set of system-specific criteria. The same applies separately for the L0-primitive-generating electronics of L0 detectors as well as the trigger processing and general data processing infrastructure.

For the $K_{\mu\nu\mu\mu}$ analysis, bursts labelled as “bad” for any of the following components are rejected. The data gathering and processing components requested to perform well span the L0-primitive generators of NA48-CHOD, CHOD, MUV3 and RICH, together with the L0 and L1 trigger-processing electronics and the central processing routine. The detector systems with verified data quality include KTAG, GigaTracker, STRAW, NA48-CHOD, CHOD, LKr and MUV3.

## 5.3 Simulated data

Simulated (MC) data samples are used in the analysis to calculate the acceptances of the signal and normalisation modes and to provide background estimates. The branching ratios of $K^+$ decay channels considered as potential sources of background in the analysis cover the orders of magnitude ($10^{-8}$ to $10^{-2}$). Together with the expected small acceptances, this fact prevents the simulation of all the processes using the standard (full) procedure given the required resources. Hence, a set of biasing methods and simplified simulation modes are present within the na62fw. The **Fast** and **Standard** modes refer to the set of simulated detector systems, while the **Capped** enables constraining the lifetimes of simulated particles, making it functionally independent from the previous two. All three simulation modes are described in the following subsection, including the tools allowing for the combination of their outputs.

By design, the NA62 detector can measure products of $K^+$ decays occurring within the z-range defined in Equation 5.1.3. To account for the resolution on the reconstructed vertex position, the default approach involves forcing simulated $K^+$ particles to decay within (102.425 to 180.0) m, with the lower limit defined by the position of the third GTK station. Kaon decays upstream of that boundary can generate a signature compatible with a decay in the FV, hence samples simulated with such conditions are also produced and referred to as “upstream”. The “near upstream” mode pertinent to this analysis is described below. The section concludes with a summary of all the MC samples used in the analysis.

### 5.3.1 Simulation modes

The **Standard** simulation mode includes all NA62 detector systems described within NA62MC. As the most accurate method relying on a minimal amount of simplifications, it is the default approach for generating MC samples, whenever the required size falls within the available computing and data storage resources.

The **Fast** mode aims to reduce the computing time by factor ∼20 by not simulating any detectors downstream of the NA48-CHOD, i.e. excluding the calorimeters and the MUV3, as well as forgoing the generation and propagation of Cherenkov photons in the KTAG. In principle, data from any of the excluded detectors and the KTAG can be later emulated prior to reconstruction, using a tool called the *FastMCHandler*, based on “true”, i.e. simulated information on the passage of particles through the apparatus. The present version of the *FastMCHandler* covers only KTAG and MUV3 signatures. The KTAG response is accounted for by adding a random number of hits sampled from a Poisson distribution of rate 20, randomly distributed between the octants and the PMTs within them. The MUV3 response is emulated for particles originating from upstream of the LKr, verified from “true” information. All the muons, as well as 1% of pions with a randomised inelastic interaction contribution [115], are considered. The effect of scattering in the calorimeters is simulated including momentum-dependence. If the extrapolated position of the particle computed from “true” information at MUV3 plane with the randomised scattering contributions falls within a MUV3 tile, a signal is generated. Samples simulated in the **Fast** mode by construction do not include the calorimetric response. The energy deposit due to presence of pions that do not undergo any decay or with a final position downstream of the LKr is emulated at analysis level by the *LKrPionEnergyEmulator* tool of the na62fw. The tool samples $E_{LKr}/p_{track}$ values from two-dimensional spectra accounting for the track momentum, with the allowed range spanning (10 to 44) GeV/$c$. The spectra were obtained from data $K_{3\pi}$ events collected with the “Multitrack” trigger stream, separately for negative and positive pions.

The **Capped** mode involves biasing of the lifetimes of $K^+$ daughters, without impact on the subset of detector systems simulated. In the $K_{\mu\nu\mu\mu}$ analysis, this technique allows for forcing charged pion decays in flight, so that they can generate the experimental signature of a muon. The maximum allowed z-position of the “capped” particle, $z_{max}$ can be adjusted by the user, with the standard value of 245.9 m being the location of the iron wall preceding the MUV3 detector. The maximum proper lifetime of the particle, $t_{max}$ is defined as

$$t_{max} = 1.01 \times \frac{z_{max} - z_{vtx}}{\gamma c \beta}, \tag{5.3.1}$$

where $z_{vtx}$ is the true position of the $K^+$ decay, $\gamma$ and $c\beta$ are the Lorentz factor and speed of the particle in the laboratory frame of reference respectively. The “safety factor” of 1.01 accounts for particles not travelling parallel to the z-axis. For all unstable $K^+$ daughters, their simulated lifetime is sampled as random variable, $t$, from the distribution

$$f(t) = \frac{1}{\tau} e^{-t/\tau}, \tag{5.3.2}$$

where $\tau$ is the mean lifetime of the particle. In the **Capped** mode, the lifetimes are sampled until the required minimum number of particles satisfy $t < t_{max}$, where the probability assigned to achieving such a lifetime is

$$p = 1 - e^{-t_{max}/\tau}. \tag{5.3.3}$$

Each event is then assigned a weight computed from the probability values according the requested number of “capped” decays as well as the total number of the particles of that species. The weights allow for straightforward combination of **Capped** samples of one decay mode with standard samples of another. While the simulated proper lifetime of a particle is not propagated as “true” information from the simulation to the analysis stage, a boolean flag indicating whether the $t < t_{max}$ condition was satisfied is saved on a particle basis. In case of MC samples produced using the **Capped** functionality having multiple final state particles of the “capped” type, their name includes the required minimum number of biased decays. For example, samples representing the $K^+ \to \pi^+\pi^+\pi^-$ decay can be of the “Capped1”, “Capped2” or “Capped3” type, since all charged pions are treated as a single type.

### 5.3.2 "Near upstream" simulation

In the "near upstream" simulation mode, the $K^+$ are forced to decay within (96.95 to 102.425) m, delimited by the second and third GTK stations. The mode is used to assess the impact of early decays with a misreconstructed decay vertex. The combination of such decays with samples produced with the default kaon decay range requires the calculation of a scaling factor, $f_K$, accounting for the kaon flux into the relevant region and the probability of decay. Explicitly,

$$f_K = \frac{e^{-Z_1^U/\alpha}(1 - e^{-(Z_2^U - Z_1^U)/\alpha})}{e^{-Z_1^S/\alpha}(1 - e^{-(Z_2^S - Z_1^S)/\alpha})}, \tag{5.3.4}$$

where $Z^{S(U)}$ are the boundaries of the decay range for the standard (near upstream) mode. The symbol $\alpha = \tau\beta c\gamma$ represents the product of mean lifetime, speed and Lorentz factor of a 75 GeV/$c$ $K^+$. The $Z^S$ values used are the extremes of the acceptance range contained in Equation 5.1.3, while the $Z^U$ limits cover the whole range of the allowed by the "near upstream" mode. The $f_K$ factor is computed assuming no energy loss by the $K^+$, a straight-line trajectory in both regions and with the mean lifetime taken as [13]

$$c\tau(K^+) = 3.711 \text{ m}, \tag{5.3.5}$$

yielding the result of

$$f_K = 0.079. \tag{5.3.6}$$

The "near upstream" mode can be requested independently of the usage of the **Capped** or **Fast** functionality. By convention, samples including "Near" in the name were produced using this mode.

### 5.3.3 Summary of used MC samples

Table 5.2 outlines the MC samples used in the analysis, for the purposes obtaining both the signal and normalisation acceptances and background estimates. The method for combining samples representing the same physical process is described in Section 5.5.

## 5.4 Event Selections

The experimental signatures of both the signal and normalisation channels contain a single incoming $K^+$ observed by the upstream detectors and three charged tracks seen by the downstream systems with no other activity. This similarity allows for the development of a common part of both event selections to minimise systematic effects arising from the differences. The common approach applies to choosing the candidate downstream track vertex, the GTK kaon track and matching the two in the temporal and spatial domains. The particle identification (PID) criteria for pions and muons, shared in the two procedures, are outlined below. Should an event pass the common selection, it is considered further either as a normalisation or signal candidate depending on the PID verdict for the tracks contained in the chosen vertex. Both selections impose further cuts, making use of the kinematic properties of the two decays and accounting for the presence of backgrounds, and define the final observables used to select signal regions.

### 5.4.1 Common selection

The aim of the common requirements for signal and normalisation channels is to select well reconstructed three-track kaon decay events, i.e. ones consistent with a decay of a K12-beam kaon and

| $K^+$ decay | MC mode | Name | $N_{Sample}$ $[10^6]$ | Branching ratio, $\mathfrak{B}$ |
|---|---|---|---|---|
| $K^+ \to \mu^+ \nu_\mu \mu^+ \mu^-$ | Standard | $K_{\mu\nu\mu\mu}$ | 13.0 | - |
| $K^+ \to \pi^+ \mu^+ \mu^-$ | Standard | $K_{\pi\mu\mu}$ | 10.2 | $(9.15 \pm 0.08) \times 10^{-8}$ [2] |
| $K^+ \to \pi^+ \pi^+ \pi^-$ | Standard | $K_{3\pi}$ | 177 | $(5.583 \pm 0.024) \times 10^{-2}$ [13] |
| $K^+ \to \pi^+ \pi^+ \pi^-$ | Fast Capped 2 | $K_{3\pi}$ FC2 | $14.7 \times 10^3$ | $(5.583 \pm 0.024) \times 10^{-2}$ [13] |
| $K^+ \to \pi^+ \pi^+ \pi^-$ | Fast Capped 3 | $K_{3\pi}$ FC3 | $5.0 \times 10^3$ | $(5.583 \pm 0.024) \times 10^{-2}$ [13] |
| $K^+ \to \pi^+ \pi^+ \pi^-$ | Near Fast Capped 2 | $K_{3\pi}$ Near FC2 | 865 | $(5.583 \pm 0.024) \times 10^{-2}$ [13] |
| $K^+ \to \pi^+ \pi^- \mu^+ \nu_\mu$ | Fast Capped 1 | $K_{\mu 4}$ FC1 | 204 | $(4.5 \pm 0.2) \times 10^{-6}$ [116] |
| $K^+ \to \pi^+ \pi^- e^+ \nu_e$ | Standard | $K_{e4}$ | 98.5 | $(4.247 \pm 0.024) \times 10^{-5}$ [13] |
| $K^+ \to e^+ \nu_e \mu^+ \mu^-$ | Standard | $K_{e\nu\mu\mu}$ | 3.7 | $(1.7 \pm 0.5) \times 10^{-8}$ [13] |

Table 5.2: List of all MC samples used for the analysis, including the decay type, MC simulation mode, branching ratio, number of simulated events and sample name.

composed of good quality downstream tracks in acceptance of the timing and PID systems. The selection is devised to maximise the acceptances of the $K_{\mu\nu\mu\mu}$ and $K_{\pi\mu\mu}$ processes, in view of data sample size being the expected dominant source of uncertainty.

The first stage of the common selection seeks events with vertices composed of three downstream tracks (3TV) and satisfying the following conditions:

1. Vertex charge consistent with a $K^+$ decay, $Q_{vtx} = \sum Q_{track} = +1$;
2. The geometric compatibility between the three STRAW tracks measured though the $\chi^2$ quantity of the vertex-fitting method $< 25$;
3. Closest distance of approach, $CDA$, between the position of the 3TV and the beam axis describing the run-average trajectory of the kaons known as the beam axis, BA, $CDA < 50$ mm;
4. Z-position of the vertex within the FV, with the lower limit increased to account for the expected impact of decays upstream of the GTK3, $Z_{vtx}(3TV) \in [110, 180]$ m;
5. Presence of either a NA48-CHOD or CHOD association for every downstream track providing the timing information;
6. Compatibility of the vertex time (defined below) with the trigger time, $|t_{vtx} - t_{trigger}| < 6$ ns.

The vertex time, $t_{vtx}$ is calculated as the average of the best NA48-CHOD and CHOD associations of all three tracks, where the contributions from the two detectors are weighted by their approximate resolutions. A single outlier time, i.e. the time with the largest contribution to the $\chi^2$ calculated with respect to the initial average, can be rejected to account for accidental activity if the $p$-value of the set is below $1 \times 10^{-3}$. Should the rejection result in no representative times for one of the tracks, the vertex candidate is dismissed.

The event is accepted only if one good quality 3TV is found, with the component tracks not present in any other three-track vertex satisfying the timing criterion (6 in the list above).

The following quality requirements are then imposed on all tracks forming the selected vertex:

1. The Spectrometer candidate is composed of hits from all four STRAW chambers;
2. The hits comprising the STRAW track are compatible with a single particle signature in space and time, as defined by the $\chi^2(STRAW)$ value of the track fit being $< 40$;
3. The track is within the geometric acceptance of the NA48-CHOD, CHOD, LKr and MUV3 detectors and does not intercept the last LAV station (LAV12);
4. Track momentum magnitude is within the design range of the Spectrometer and the kinematic spectrum of target decays, $p_{track} \in [10, 45]$ GeV/$c$;
5. General temporal consistency with the vertex time, $|t_{vtx} - t_{track}| < 12$ ns;
6. Track angle with respect to the BA consistent with the geometric acceptance of the NA62 apparatus, i.e. below 9 mrad.

The tracks should also be separated transversely by at least 15 mm and 200 mm in the z-planes of the first STRAW chamber and the LKr, respectively, to mitigate the impact of misreconstruction due to signal overlap.

All positively charged tracks satisfying the criteria above are also subject to a cut aimed at removing the impact of accidental muons from in-time $K^+ \to \mu^+\nu_\mu$ decays. The muon mass hypothesis is used to define the track four momentum for the procedure, $P_{\mu^+}$, with the requirement

$$M^2_{Miss}(K_{\mu 2}) = (P_{K^+} - P_{\mu^+})^2 > 4.5 \times 10^4 \text{ MeV}^2/c^4. \tag{5.4.1}$$

The kaon four momentum, $P_{K^+}$, is set to the run-average value. The boundary value was chosen to ensure that it is greater than $(2m_\mu)^2$, which defines the end of the $K_{\mu\nu\mu\mu}$ spectrum.

With the 3TV selected, the routine proceeds to the upstream region to chose a suitable $K^+$ candidate. Firstly, the presence of a $K^+$ is established by using the KTAG detector, where a candidate constructed from a coincidence of at least five octants must be present with a time, $t_{KTAG}$ consistent with both the 3TV and the trigger times, so that

$$|t_{vtx} - t_{KTAG}| < 6 \text{ ns} \quad \text{and} \quad |t_{trigger} - t_{KTAG}| < 6 \text{ ns}. \tag{5.4.2}$$

In case of multiple KTAG candidates satisfying the criteria, the one closest in time to $t_{vtx}$ is chosen to represent the kaon crossing time.

Once the relevant PID conditions for signal and normalisation selections are satisfied, the kinematic description of the kaon is sought from GTK information. Only GTK candidates of track-fit $\chi^2_{GTK} < 25$ are considered, with the parameter representing the quality of geometric and temporal compatibility of component hits. Each candidate is then considered for a four track vertex (4TV), composed of the three STRAW tracks and the GTK candidate. The 4TV position and $\chi^2(4TV)$ values are computed with the same approach as for a purely STRAW-track vertex. The candidate giving the best geometric compatibility, i.e. a minimum $\chi^2(4TV)$ value, is chosen. The 4TV is then subject to the following requirements.

1. The GTK candidate time, $t_{GTK}$ being consistent with the kaon crossing time, $|t_{KTAG} - t_{GTK}| < 1$ ns.
2. Good geometric compatibility between components enforced by $\chi^2(4TV) < 14$.
3. Z-position of the 4TV satisfying the same condition as the 3TV equivalent, $Z_{vtx}(4TV) \in [110, 180]$ m.

Should the conditions be fulfilled, track momenta are defined by the output of the fitting procedure, which includes small corrections to the three-momenta of all components arising from the vertex position. The timing constraint was chosen to maximise acceptance, with the relative resolution of the two systems below 200 ps. The boundary of the $\chi^2(4TV)$ requirement was optimised for signal sensitivity, as described in Section 5.6.

### 5.4.2 Particle identification conditions

A set of PID conditions is designed to select pion and muon candidate tracks based on information from three detector systems. The track momentum as provided by the downstream spectrometer, $p_{track}$ and the energy of the associated LKr cluster, $E_{LKr}$ are used to represent the fraction of energy lost by the particle through interaction in the LKr. MUV3 associations from the "outer" tiles of the detector mark the presence or absence of muons. The muon and pion criteria are outlined below.

**Muon track:**

1. At least one outer MUV3 association, with the candidate time, $t_{MUV3}$ consistent with vertex and trigger times within 6 ns.
2. No inelastic interaction in the LKr, representing the minimum-ionising-particle (MIP) nature of muons in the analysis momentum range, $E_{LKr}/p_{track} < 0.2$.

**Pion track:**

1. No outer MUV3 association within 10 ns of the vertex time.
2. Energy deposit in the LKr consistent with a MIP or an inelastic interaction leading to a shower with a hadronic component, $E_{LKr}/p_{track} < 0.9$.

### 5.4.3 Normalisation selection

The normalisation selection aimed at finding well-reconstructed $K_{\pi\mu\mu}$ decays requires a single positive track identified as a pion, with the remaining pair satisfying the muon PID conditions. Should the muon candidates have one outer MUV3 association each, the MUV3 signals must originate from different tiles. The pion-identified track is further requested to be incompatible with an upstream decay by requiring that the position at the plane corresponding to the back face of the final collimator satisfies

$$|x_{col}| > 40 \text{ mm} \quad \text{or} \quad |y_{col}| > 25 \text{ mm}. \tag{5.4.3}$$

The kinematically closed nature of the $K_{\pi\mu\mu}$ decay is utilised by requesting the difference in momentum magnitudes of the vertex composed of the three downstream tracks and the GTK candidate to satisfy

$$||\vec{p}_{\pi^+} + \vec{p}_{\mu^+} + \vec{p}_{\mu^-}| - |\vec{p}_{K^+}|| < 2.5 \text{ GeV}/c, \tag{5.4.4}$$

where $\vec{p}_X$ is the three momentum vector of track $X$ including the corrections from the vertex fitter. The transverse momentum of the downstream track system calculated with respect to the kaon candidate track, $p_T$, must be consistent with a lack of additional daughter particles, i.e.

$$p_T < 30 \text{ MeV}/c. \tag{5.4.5}$$

The invariant mass of the three downstream tracks under mass hypotheses originating from the PID verdicts is computed as

$$M_{\pi\mu\mu} = \sqrt{(P_{\pi^+} + P_{\mu^+} + P_{\mu^-})^2}, \tag{5.4.6}$$

where $P_X$ is the four momentum of a track identified as $X$, with momentum including the corrections from the vertex fitter. This variable should be consistent with the $K^+$ mass, $M_{K^+}$, for $K_{\pi\mu\mu}$ decays, hence the normalisation selection signal region is defined as

$$|M_{\pi\mu\mu} - M_{K^+}| < 8 \text{ MeV}/c^2, \tag{5.4.7}$$

where the width is taken to match the recent $K_{\pi\mu\mu}$ analysis conducted on NA62 data [2].

### 5.4.4 Signal selection

For the selected three-track vertex to be compatible with a $K_{\mu\nu\mu\mu}$ decay, all three downstream tracks must be identified as muons. If a track has a single in-time outer MUV3 association and any of the other two tracks has an in-time association from the same tile, the event is rejected. Two key kinematic properties of the event are computed, including the momentum corrections from the vertex fitter. The first is the transverse momentum of the three muon tracks with respect to the kaon one, $p_T$. The second is the momentum deficit, $\Delta p$, defined as

$$\Delta p = |\vec{p}_{K^+}| - |\vec{p}_{\mu_1^+} + \vec{p}_{\mu_2^+} + \vec{p}_{\mu^-}|, \tag{5.4.8}$$

where $\vec{p_X}$ is the three momentum vector of a track identified as particle $X$. The two parameters indirectly describe the momentum and direction of the $\nu_\mu$ escaping detection. Cuts are made on both quantities, exercising the kinematically open nature of the $K_{\mu\nu\mu\mu}$ decay, so that

$$p_T \in [0, 140] \text{ MeV}/c \quad \text{and} \quad \Delta p \in [4, 40] \text{ GeV}/c. \tag{5.4.9}$$

The upper limits of both ranges correspond to the ends of the respective spectra as obtained from simulation of the $K_{\mu\nu\mu\mu}$ mode, with the lower limits determined by optimisation, as described in Section 5.6. The final kinematic variable used in the selection is the squared missing mass of the three muon system with respect to the $K^+$ track, $M^2_{Miss}(K_{\mu\nu\mu\mu})$, corresponding the the square of the $\nu_\mu$ mass and hence expected to peak at 0 for the signal mode. It is calculated as

$$M^2_{Miss}(K_{\mu\nu\mu\mu}) = (P_{K^+} - P_{\mu_1^+} - P_{\mu_2^+} - P_{\mu^-})^2, \tag{5.4.10}$$

where $P_X$ is the four momentum of particle $X$. The signal region spans

$$|M^2_{Miss}(K_{\mu\nu\mu\mu})| < 900\ \text{MeV}^2/c^4, \tag{5.4.11}$$

following prior unfinished work on the $K_{\mu\nu\mu\mu}$ analysis of NA62 data [117] and delimited by values where the simulated signal channel contribution roughly equals that of the sum of backgrounds, see Figure 5.13.

## 5.5 Background modelling

The experimental signature of the $K_{\mu\nu\mu\mu}$ decay, i.e. three downstream tracks identified as muons and a single incoming $K^+$, can be mimicked by a variety of processes in the NA62 experiment. The contribution from individual $K^+$ decays enters through daughter particle misidentification or decays. Charged particles of two species species other than muons can be created in $K^+$ decays: the electrons (positrons) and the pions. The former are stable particles unlikely to receive a positive muon PID due to containment of electromagnetic showers in the LKr. Charged pions preferentially decay to muon-neutrino pairs, with the branching ratio [13]

$$\mathfrak{B}(\pi^+ \to \mu^+\nu_\mu) = (99.98770 \pm 0.00004) \tag{5.5.1}$$

For a representative $K^+$-daughter pion of momentum 20 GeV/$c$, the mean distance travelled by the particle is

$$l = \gamma \cdot \beta c \cdot \tau_{\pi^\pm} \simeq 1120\ \text{m}, \tag{5.5.2}$$

where $c \cdot \tau_{\pi^\pm} = 7.8045\,\text{m}$ [13]. As the pions from $K^+$ decays in the FV traverse (66 to 101) m before encountering the first PID system, the LKr, the probability of a positive muon identification verdict lies in the (5.9 to 9.0)% range. Furthermore, the LKr energy deposits due to passage of pions can be consistent with a minimum-ionising-particle (MIP) signature. Hadronic shower secondaries from pion interactions in the calorimeters can generate muons, giving a temporally compatible MUV3 hit, with the probability of about 1% [115]. Accidental in-time activity in the MUV3 can also provide an association, albeit with a lower probability (see Section 5.5.1.1). Consequently, events with in-flight pion decays are expected to dominate the background contributions.

In summary, $K^+$ decays with final states being a combination of muons and charged pions are the most likely sources of background. This category includes the normalisation mode, $K_{\pi\mu\mu}$, as well as the $K_{3\pi}$ and $K_{\mu4}$ processes. The experimental signatures of such events will vary depending on the number of pion decays upstream of the LKr and their exact positions.

The following discussion assumes that the daughter muon is not co-linear with the pion. Consequences of individual pion decay in various z-ranges regarding the reconstruction of particle direction upstream of the STRAW, measurement of the momentum magnitude and impact on associations of signal from detectors downstream of the STRAW are presented in Table 5.3. Pion decays upstream of STRAW2 will lead to misreconstruction of its trajectory between the original $K^+$ decay and the Spectrometer, which is expected to affect the geometric compatibility with the other tracks and yield an increased $\chi^2$ value from the vertex fitter. Should a pion decay upstream of the final STRAW chamber, the measured momentum does not represent that of the original particle. Consequently, the momentum of a three-track vertex containing at least one such particle is not consistent with the

| Region start | Region end | Pion upstream trajectory | Momentum magnitude | Downstream associations |
|---|---|---|---|---|
| 110 $m$ | STRAW1 | × | $\mu$ measured | ✓ |
| STRAW1 | STRAW2 | × | misreconstructed | ✓ |
| STRAW2 | STRAW3 | ✓ | misreconstructed | ✓ |
| STRAW3 | STRAW4 | ✓ | misreconstructed | × |
| STRAW4 | MUV3 | ✓ | $\pi$ measured | × |

Table 5.3: The z-ranges of in-flight $K^+$-daughter pion decay and their impact on reconstructing the upstream particle trajectory, the measurement of momentum magnitude and geometric association with signal from detectors downstream of the STRAW, used for particle identification.

mother $K^+$ momentum, which can results in the measured kinematic properties being similar to the target $K_{\mu\nu\mu\mu}$ mode. In-flight pion decays downstream of the third STRAW chamber lead to a misreconstruction of particle trajectory downstream of the Spectrometer, which can impact the association with signal from PID detectors. In extreme cases, a particle not incident on the LKr or MUV3 can be identified as within geometric acceptance one or both of the two detectors.

The high-intensity nature of the NA62 experiment necessitates the consideration of multiple in-time decays with some particles going undetected or an incomplete reconstruction of a $K^+$ decay together with a presence of a halo muon. Both cases are addressed by the overlay procedure, where the $K^+$ decays and halo particles are injected into simulated data, randomly distributed in time and sampled from a library containing the observed signatures of six most likely $K^+$ decays and halo components. Kinematic constraints and the timing performance of the NA62 apparatus allow to discount triple coincidences as a significant source of background, with their expected contribution significantly smaller than that of two in-time geometrically compatible processes.

Given the lack of known particles with multiple units of electric charge below the kaon mass and conservation of electric charge, $K^+$ decays can generate only odd numbers of charged daughters. This constraint, together with the expected negligible contribution of triple coincidences, justifies considering only three track decays as background mechanisms for the purposes of this analysis. The techniques used for modelling the background contributions from all considered $K^+$ decay modes are described in this section.

### 5.5.1 $K_{3\pi}$ decays

With the theoretically predicted $\mathfrak{B}_{\mu\nu\mu\mu}$ (see Equation 2.4.15) being six orders of magnitude smaller than the branching ratio of the $K_{3\pi}$ process (see Table 5.2) and the probability of in-flight charged pion decay of order a few percent, the $K_{3\pi}$ decays are expected to be a significant source of background. To mimic the momentum deficit of the $K_{\mu\nu\mu\mu}$ signal, events of this type should include at least one in-flight pion decay upstream of the final STRAW chamber leading to misreconstruction of particle momentum.

The “Fast Capped” simulation mode is used to produce samples with at least two and three forced pion decays upstream of the MUV3. The individual event weights, defined below, allow to combine these samples with the other background channels and scale them to real data. The standard $K_{3\pi}$ sample provides events with one or no pion decays upstream of the MUV3, selected by verifying the decision of the capping algorithm, propagated from MC simulation stage to analysis level.

#### 5.5.1.1 $K_{3\pi}$ with less than two in-flight pion decays

The contribution of $K_{3\pi}$ events with less than two in-flight pion decays is expected to be smaller than that of $\geq 2$ in-flight pion decays given the relative probability of in-flight decay and misidentification based on LKr, STRAW and MUV3 signatures (misID). The production of a standard sample of sufficient statistical power for such events was deemed unfeasible, hence a forced misID procedure was developed. It relies on estimating the probability of an individual undecayed pion track not identified as a muon to receive a muon PID verdict as a function of reconstructed track momentum, $p_{track}$ and extrapolated position at the MUV3 plane, $\vec{r}_{MUV3}$, as

$$\begin{aligned} P_{\pi\to\mu}(p_{track}, \vec{r}_{MUV3}) = P_{LKr\ punch-through}(p_{track}) + P_{MUV3\ accidental}(p_{track}, \vec{r}_{MUV3}) \\ -P_{LKr\ punch-through}(p_{track}) \times P_{MUV3\ accidental}(p_{track}, \vec{r}_{MUV3}). \end{aligned} \tag{5.5.3}$$

The $P_{LKr\ punch-through}(p_{track})$ and $P_{MUV3\ accidental}(p_{track}, \vec{r}_{MUV3})$ symbols represent the probabilities of a pion track passing the muon PID requirements of Section 5.4.2 due to hadronic-shower-related and accidental activity in the MUV3, respectively. The final correlation term is subtracted to account for independent origins of the two contributions.

The “punch-through” contribution, i.e. due to muons originating from inelastic interactions of the pion in calorimeters, is quantified from a sample of simulated $K^+ \to \pi^+\nu\bar{\nu}$ events. The sample in question is generated in the non-overlaid mode, so that only the detector signals generated by the single charged pion are recorded in each event, without any accidental activity. The probability is measured on tracks satisfying the following criteria.

1. The pion originated from the $K^+$ and did not decay according to “true” MC information.
2. The resultant track passed all the quality criteria of Section 5.4.1 apart from the momentm magnitude one.
3. The Spectrometer track has a closest distance of approach, $CDA$, with respect to the run-average beam axis, $BA$ compatible with a beam $K^+$ decay, $CDA(BA) < 50$ mm.
4. The point minimising the $CDA(BA)$ value has a z-coordinate satisfying the analysis requirement $Z_{CDA} \in [110, 180]$ m.
5. The associated LKr signal points to a MIP or a shower with a hadronic component, $E_{LKr}/p_{STRAW} < 0.9$.

The probability of such tracks to satisfy muon PID requirements of Section 5.4.2 is measured as a function of track momentum. The result, with a linear fit in the range (8 to 50) GeV/$c$, is shown in Figure 5.2. The fitted linear dependence is used to compute $P_{LKr\ punch-through}(p_{track})$ in the analysis momentum range, yielding a result of $8.9 \times 10^{-4}$ for a 25 GeV/$c$ pion.

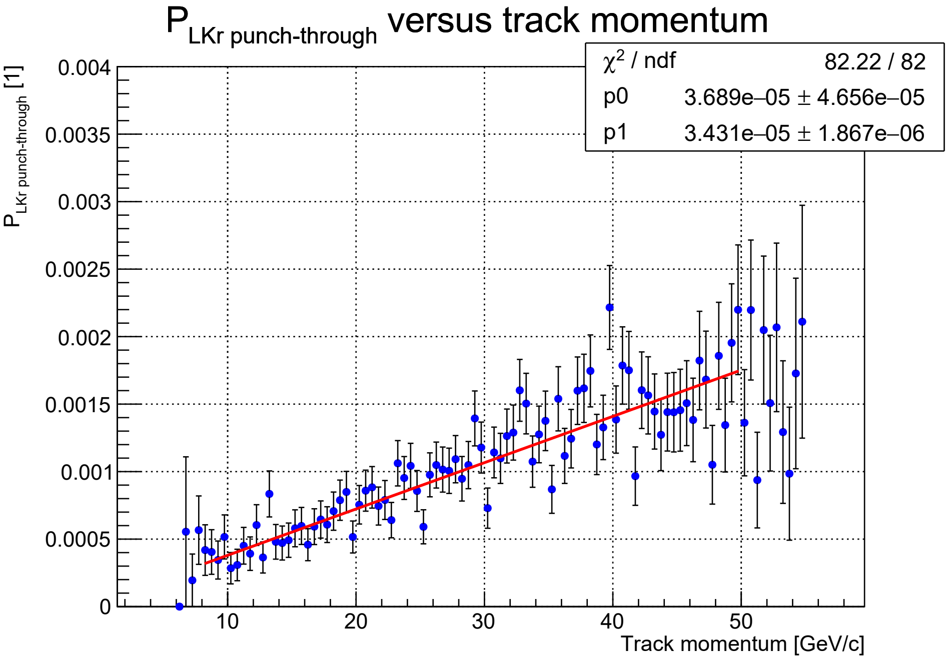

Figure 5.2: The probability of a pion track satisfying analysis quality cuts to receive a positive muon identification verdict due to hadronic-shower-related activity in the MUV3 (“LKr punch-through”). The measurement was performed on a non-overlaid MC sample of $10^7$ $K^+ \to \pi^+\nu\bar{\nu}$ decays. The results of a linear fit (red curve) are presented in the inset.

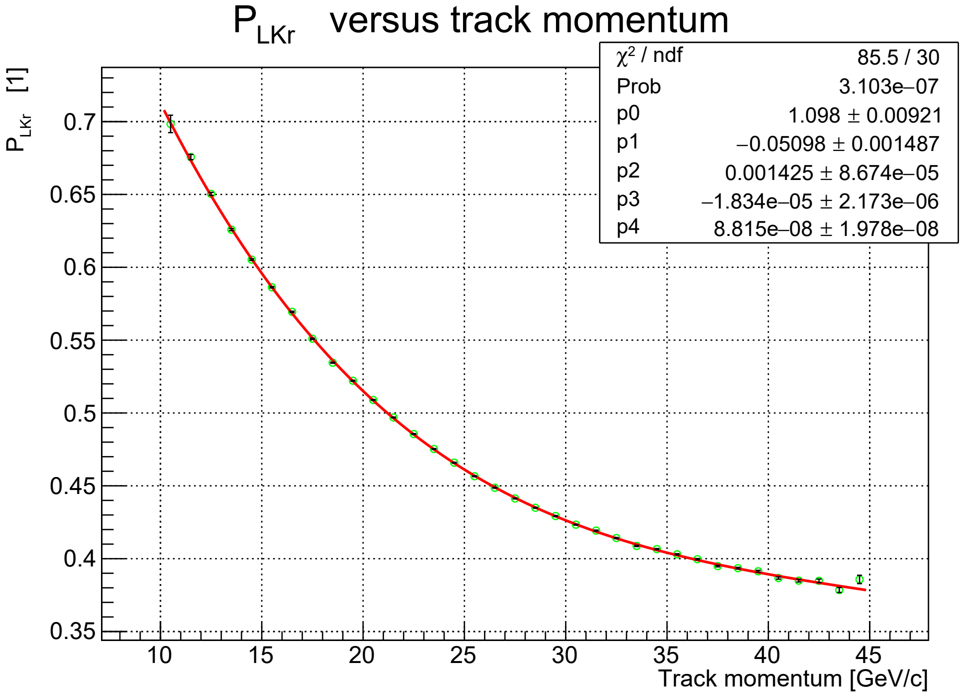

Figure 5.3: The probability for a pion track to satisfy the $E_{LKr}/p_{STRAW} < 0.2$ particle identification requirement. Measured on $E_{LKr}/p_{STRAW}$ spectra used by the *LKrPionEnergyEmulator* tool, which constructs the profiles for events passing the standard $K_{3\pi}$ selection of na62fw [96]. The results of a fit with a fourth degree polynomial of reconstructed track momentum, $f(m) = \sum_{0 \leq n \leq 4} p_n m^n$, are presented in the inset and as the red curve.

The pion misidentification contribution due to MUV3 accidental activity is further factorised as

$$P_{MUV3\,accidental}(p_{track}, \vec{r}_{MUV3}) = P_{LKr\,\mu}(p_{track}) \times P_{MUV3\,hit}(p_{tracl}, \vec{r}_{MUV3}), \tag{5.5.4}$$

where $P_{LKr\,\mu}(p_{track})$ and $P_{MUV3\,hit}(p_{track}, \vec{r}_{MUV3})$ denote the probability of the $E_{LKr}/p_{STRAW}$ value and an accidental MUV3 hit satisfying the muon PID criteria respectively. The former is computed from the $E_{LKr}/p_{STRAW}$ spectra used by the *LKrPionEnergyEmulator* tool, considering negative and positive pions together. For pion track momentum spanning (10 to 45) GeV/$c$, the probability of $E_{LKr}/p_{STRAW} < 0.2$ is calculated with a binomial error. The obtained dependence was parametrised through an empirical fit with a fourth degree polynomial of reconstructed track momentum. The calculated $E_{LKr}/p_{STRAW} < 0.2$ values and the fitted model, including numerical values for the polynomial coefficients, are shown in Figure 5.3.

The $P_{MUV3\,hit}(p_{track}, \vec{r}_{MUV3})$ dependence is calculated by exactly reproducing the Spectrometer-MUV3 association routine and summing over the average hit rate of outer tiles geometrically compatible with the track. This procedure does not account for association overlap, i.e. a single MUV3 tile providing associations to multiple Spectroemter tracks, and necessitates the usage of a data sample of minimum bias. To satisfy the requirement, out-of-time signals in the MUV3 from events collected through the "Control" trigger stream are used. The representative time window for average MUV3 illumination was chosen as

$$|t_{trigger} - t_{MUV3}| \in [20, 30] \text{ ns}, \tag{5.5.5}$$

where $t_{trigger}$ is the trigger time and the values are motivated by the profile shown in the left panel of Figure 5.4. The outer tile hit rate is computed by dividing the hits scored in a single tile by the product of the number of processed events and the width of the time window, with the result shown in the right panel of Figure 5.4. The calculation of $P_{MUV3\,hit}(p_{track}, \vec{r}_{MUV3})$ for individual tracks involves summing over rates from geometrically compatible tiles scaled by the width of the MUV3 association time window. Figure 5.5 illustrates the result of this treatment for pions passing the common selection in three momentum ranges. Note that high momentum pion tracks illuminate only the inner part of the MUV3. For reconstructed track momenta spanning (10 to 15) GeV/$c$, the largest $P_{MUV3\,hit}(\vec{r}_{MUV3})$ probabilities are obtained for trajectories extrapolated to the centers of outer MUV3 tiles, while at higher momenta the maxima migrate to tile corners. This effects is due

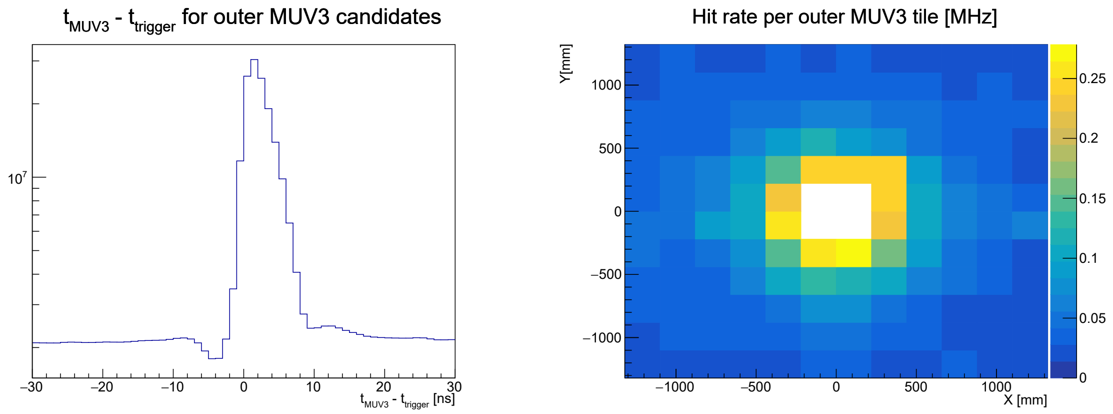

Figure 5.4: Left: difference between the time of MUV3 hits from outer tiles and the trigger time for events captured with the "Control" trigger stream in 2018. Right: average hit rate in MHz for outer MUV3 tiles as measured from hits satisfying $|t_{MUV3} - t_{trigger}| \in [20, 30]$ ns on the same data sample.

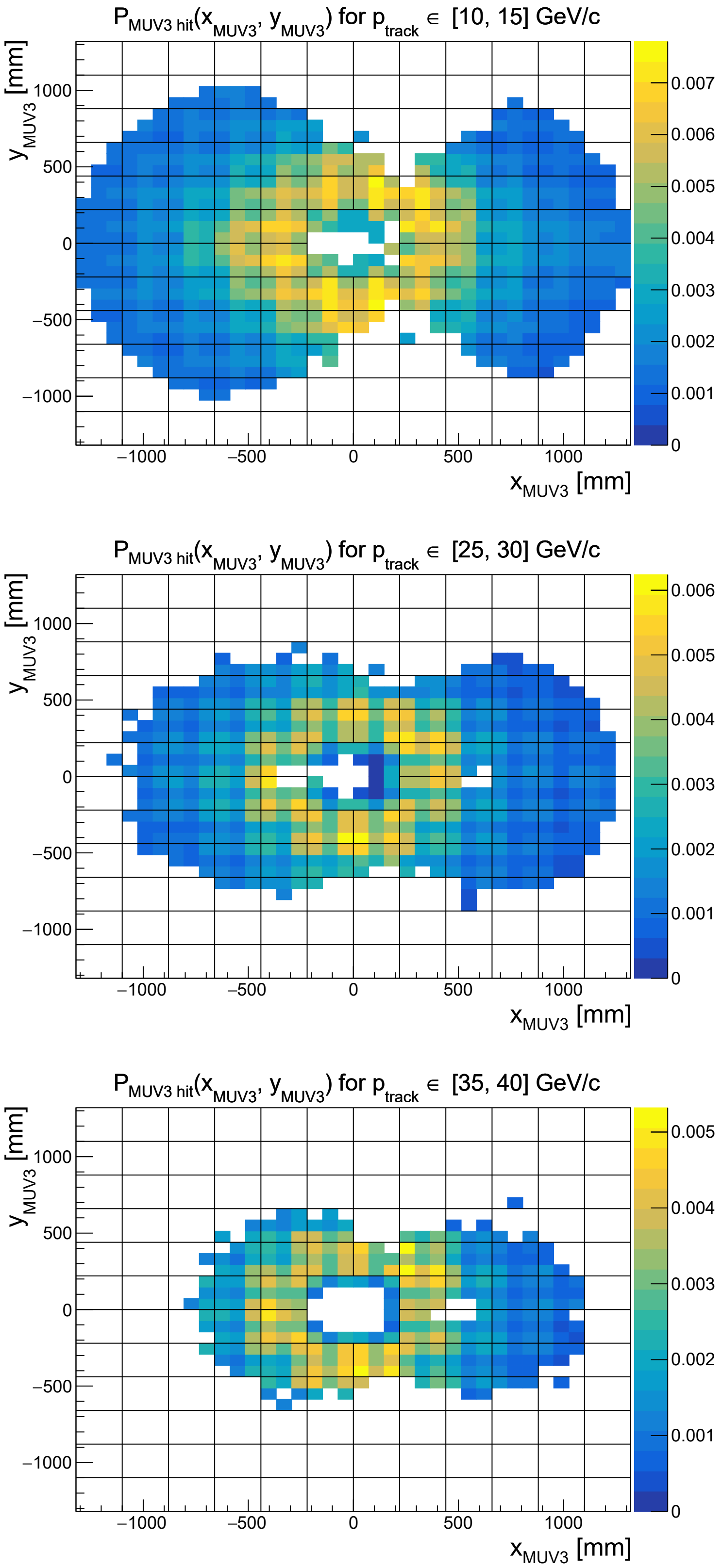

Figure 5.5: The probability for a pion track to have an in-time MUV3 association due to accidental activity in the detector as a function of extrapolated track position at MUV3 plane. Figures obtained separately for three reconstructed track momentum ranges: (10 to 15) GeV/$c$ (top), (25 to 30) GeV/$c$ (middle) and (35 to 40) GeV/$c$ (bottom). The partial illumination of the detector is due to using only pion tracks from vertices passing the common selection. On each figure, the outlines of outer MUV3 tiles are marked by black lines.

| Selection | Particle(s) for misID | Event weight |
|---|---|---|
| Signal | All undecayed $\pi^{\pm}$ | $\prod_{i\in\pi^{\pm}}\left(\frac{P^{i}_{\pi\to\mu}}{1-P^{i}_{\pi\to\mu}}\right)$ |
| Normalisation | $\pi^{+}$ | $\frac{2\times P^{+}_{\pi\to\mu}}{1-P^{+}_{\pi\to\mu}}$ |
| Normalisation | $\pi^{-}$ | $\frac{P^{-}_{\pi\to\mu}}{1-P^{-}_{\pi\to\mu}}$ |
| Normalisation | $\pi^{+},\pi^{-}$ | $\frac{2\times P^{+}_{\pi\to\mu}\times P^{-}_{\pi\to\mu}}{(1-P^{+}_{\pi\to\mu})\times(1-P^{-}_{\pi\to\mu})}$ |

Table 5.4: Weights assigned to $K_{3\pi}$ events with forced misID of pions as muons depending on the selection, number and charge of tracks matched to simulated undecayed pions. The denominators correct for application of pion PID criteria prior to forced misidentification as muons.

to the change in the association search radius, which is inversely proportional to track momentum. Overall, as evident from Figures 5.3 and 5.5, the probability of misidentifying a pion as a muon due to accidental activity in MUV3 lies in the few ‰ range.

The $K_{3\pi}$ samples subject to the forced misID mechanism are treated differently to standard samples. The common selection is applied without enforcing the “MO2” condition from the L0 trigger emulator. Tracks identified as muons are processed according to standard procedure. For the remaining tracks, the pion PID criteria must be satisfied and a match to the trajectory of a “true” simulated pion that did not decay is required. Individual $P_{\pi\to\mu}(p_{track},\vec{r}_{MUV3})$ values are then computed for the particles required to satisfy the signal or normalisation condition and the weight of the event is calculated as defined in Table 5.4, with the denominators correcting for the application of pion PID requirements. For the normalisation selection, if two undecayed positive pions are found in an event, the one to be misidentified is chosen at random with no further requirements imposed on the other track. If an event satisfies the PID conditions of a selection without the need for misID, it is rejected to avoid double-counting. The candidate vertices are then subject to the remainder of the respective selections.

The accuracy of the forced misID procedure can be verified with two methods. The first checks for consistency with respect to full MC simulation by calculating the probability of a track from a $K_{3\pi}$ event passing the common selection and produced by an undecayed pion according to “true” information to receive a muon PID verdict. In the analysis momentum range of (10 to 45) GeV/$c$ the probability measured on full MC yields (2.5 to 4.5) ‰, consistent with the quantified summed effects of LKr “punch-through” and MUV3 accidental activity. The agreement with respect to real data can be judged by investigating the sideband of the final kinematic variable of the normalisation selection, see the result in Section 5.7.1.

#### 5.5.1.2 $K_{3\pi}$ with at least two in-flight pion decays

The $K_{3\pi}$ events with two and three in-flight pion decays upstream of the MUV3 are modelled by the usage of “Fast Capped2” and “Fast Capped3” MC samples. In the former case, the single-lifetime probabilities as defined in Equation 5.3.3, $p_i$ are combined to provide an event weight such that

$$w(K_{3\pi}FC2) = p_1p_2(1-p_3) + p_1(1-p_2)p_3 + (1-p_1)p_2p_3 + p_1p_2p_3. \tag{5.5.6}$$

The mean weight of “Fast Capped2” event is $2.5 \times 10^{-2}$. The first three terms in the above equation correspond to two “capped” pions, while the fourth represents all particles being forced to decay. Consequently, the “Fast Capped3” event weight is computed as

$$w(K_{3\pi}FC3) = p_1 p_2 p_3, \tag{5.5.7}$$

yielding the mean value of $8.0 \times 10^{-4}$.

Combination of the samples in the same analysis is enabled by the decision of the cappping algorithm being saved on a single particle basis. While processing the “Fast Capped2” sample, events with three forced pion decays are counted for the acceptance denominator and then rejected. The “Fast Capped2” and “Fast Capped3” samples, with the three in-flight pion decay events removed from the former, are referred to as “$K_{3\pi}$ FC 2 Dec” and “$K_{3\pi}$ FC 3 Dec” in the following sections, respectively.

To account for the lack of calorimetric information in the **Fast** simualtion mode, muons originating from pion decays upstream of the LKr are assumed to pass the $E_{LKr}/p_{track}$ PID cut. For pions reaching the LKr, the emualted energy deposits obtained from the *LKrPionEnergyEmulator* tool are used to enforce the relevant condition.

### 5.5.2 $K^+ \to \pi^+\pi^-\mu^+\nu_\mu$ decays

The presence of a neutrino in the $K^+ \to \pi^+\pi^-\mu^+\nu_\mu$ ($K_{\mu4}$) decay final state yields similar kinematics to the signal channel. The process hence acts as a background source in the event of misidentification or in-flight decay of the two pions. The $K_{\mu4}$ decay is expected be to a subdominant background, since the ratio of the $K_{\mu4}$ to $K_{3\pi}$ branching ratios is an order of magnitude smaller than the probability of in-flight pion decay. Hence, only a “Fast Capped1” MC sample, with at least one in-fligh pion decay, is used to model the potential impact of this process. The weight of an event is defined as

$$w(K_{\mu4}FC1) = p_1 + p_2 - p_1 p_2, \tag{5.5.8}$$

where $p_i$ is the probability computed through Equation 5.3.3 for charged pion $i$. The average weight for a $K_{\mu4}$ “Fast Capped1” event is 0.17. The particle identification criteria using the $E_{LKr}/p_{STRAW}$ quantity for this sample are handled in the same manner as for the $K_{3\pi}$ “Fast Capped” samples.

### 5.5.3 $K_{\pi\mu\mu}$, $K^+ \to \pi^+\pi^-e^+\nu_e$ and $K^+ \to e^+\nu_e\mu^+\mu^-$ decays

The $K_{\pi\mu\mu}$ process is expected to provide a significant contribution to the background contamination, as a decay of the pion results in a final state identical to $K_{\mu\nu\mu\mu}$. The small branching ratio of $K_{\pi\mu\mu}$ allows to utilise the standard MC simulation mode, achieving good statistical power and a complete simulation. Both aspects are also critical in providing a reliable estimate of the normalisation mode acceptance, key to the $\mathfrak{B}_{\mu\nu\mu\mu}$ measurement.

Both the $K^+ \to \pi^+\pi^-e^+\nu_e$ ($K_{e4}$) and $K^+ \to e^+\nu_e\mu^+\mu^-$ ($K_{e\nu\mu\mu}$) decays are expected to yield small background contributions to the signal channel, given the low probabilities of misidentifying a positron as a muon. The two processes should have different kinematic signatures to $K_{\mu\nu\mu\mu}$ due to the significant mass difference of positrons and muons, lowering the expected impact of a non-reconstructed positron track being replaced by an in-time muon or pion. The $K_{e4}$ and $K_{e\nu\mu\mu}$ decays can mimic the normalisation channel signature if the positron receives a positive pion PID verdict. The impact of $K_{e4}$ and $K_{e\nu\mu\mu}$ processes is estimated using the standard simulation mode.

## 5.6 Signal selection optimisation

The signal selection described in Sections 5.4.1 and 5.4.4 offers two opportunities for the reduction of backgrounds based on the kinematic and geometric properties of the signal and background modes. The former utilises the transverse momentum, $p_T$, and momentum deficit, $\Delta p$ (defined in Equation 5.4.8). The latter relies on in-flight pion decays potentially causing the track trajectory upstream of the Spectrometer not being consistent with the original pion direction, leading to poorer geometric consistency between the tracks. Both of these approaches allow to optimise the selection to minimise the uncertainty on the measured branching ratio or maximise signal sensitivity by repeating the entire analysis procedure for each hypothesis in the considered range of selection requirements.

### 5.6.1 Vertex kinematics

The kinematic quantities $p_T$ and $\Delta p$ are an indirect representations of the momentum magnitude and direction of the signal mode neutrino. The two-dimensional spectra of these variables obtained prior to the $M^2_{Miss}(K_{\mu\nu\mu\mu})$ cut for real data and three simulated samples: $K_{\mu\nu\mu\mu}$ and $K_{3\pi}$ with two and three forced in-flight pion decays, are presented in Figure 5.6. The distribution obtained for the signal MC sample motivated the choice of the upper limits of the allowed ranges for both quantities, as defined in Equation 5.4.9. An upper limit on the $p_T$ quantity is necessary in view of the presence of data events above the value, most likely due to misreconstructed $K_{3\pi}$ events with pion decays. The spectra of Figure 5.6 show the discriminating power of cuts on those two variables, given the significantly different shapes of the signal mode and $K_{3\pi}$ decays, which are expected to be the most significant background contributions. To exercise the discriminating capability of the $p_T$ and $\Delta p$ variables, a two-dimensional scan is performed with the kinematic cuts

$$p_T \in [p_T^{min}, 140]\ \text{MeV}/c \quad \text{and} \quad \Delta p \in [\Delta p^{min}, 40]\ \text{GeV}/c, \tag{5.6.1}$$

where the minima span the values

$$p_T^{min} \in [0, 90]\ \text{MeV}/c \quad \text{and} \quad \Delta p^{min} \in [0, 15]\ \text{GeV}/c, \tag{5.6.2}$$

in steps of $5\,\text{MeV}/c$ and $1\,\text{GeV}/c$ respectively. The study was performed prior to the optimisation described in the next section, i.e. with a cut of $\chi^2(4TV) < 15$. A computation of key parameters described in Section 5.1.1 is performed for each pair of values by applying the full analysis procedure to both real and simulated data. The resultant dependence of the observed background fraction, i.e. the ratio of numbers of expected background contamination to the data events in the $K_{\mu\nu\mu\mu}$ selection signal region ($N_{Bkgd}/N_{data}$), respectively, is shown in Figure 5.7. In the bottom left corner of the plot, covering values $p_T^{min} < 30$ MeV/$c$ and $\Delta p^{min} < 2$ GeV/$c$, the signal region is clearly dominated by background. The top extremities of Figure 5.7 show the possibility of nearly background-free selection, where $N_{Bkgd}/N_{Data} < 5\%$.

To obtain a better metric representing the discriminating power of the $p_T$ and $\Delta p$ cuts, one can utilise signal significance, $(N_{Data} - N_{Bkgd})/\sqrt{N_{Data}}$, i.e. the ratio of background-subtracted data events to the square root of the total population of the signal region. In the case of a purely signal-

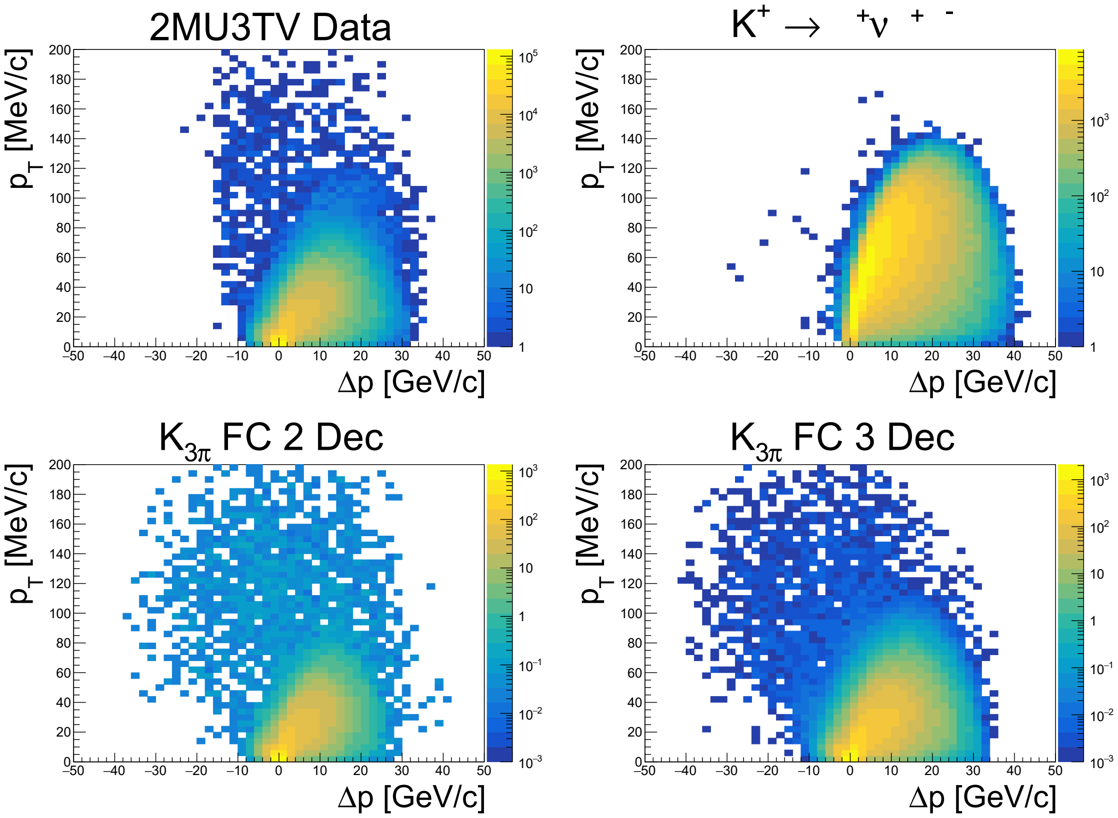

Figure 5.6: Spectra of $p_T$ and $\Delta p$ variables obtained during signal selection prior to the final mass cut. From top left to bottom right: data sample and three samples of simulated events: $K_{\mu\nu\mu\mu}$, $K_{3\pi}$ with two forced in-flight pion decays and $K_{3\pi}$ with three such decays.

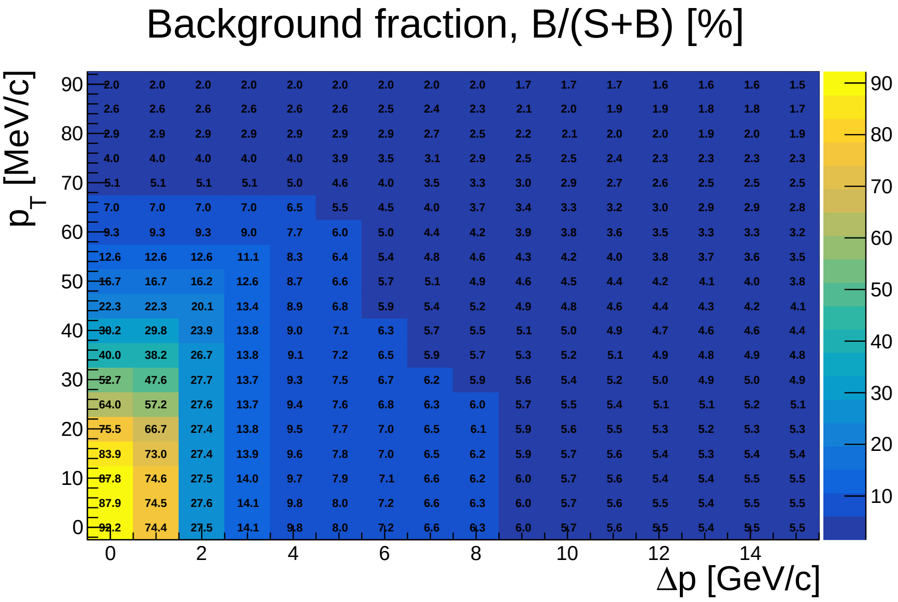

| | | | | | | | | | | | | | | | |
|---|---|---|---|---|---|---|---|---|---|---|---|---|---|---|---|
| 2.0 | 2.0 | 2.0 | 2.0 | 2.0 | 2.0 | 2.0 | 2.0 | 2.0 | 1.7 | 1.7 | 1.7 | 1.6 | 1.6 | 1.6 | 1.5 |
| 2.6 | 2.6 | 2.6 | 2.6 | 2.6 | 2.6 | 2.5 | 2.4 | 2.3 | 2.1 | 2.0 | 1.9 | 1.9 | 1.8 | 1.8 | 1.7 |
| 2.9 | 2.9 | 2.9 | 2.9 | 2.9 | 2.9 | 2.9 | 2.7 | 2.5 | 2.2 | 2.1 | 2.0 | 2.0 | 1.9 | 2.0 | 1.9 |
| 4.0 | 4.0 | 4.0 | 4.0 | 4.0 | 3.9 | 3.5 | 3.1 | 2.9 | 2.5 | 2.5 | 2.4 | 2.3 | 2.3 | 2.3 | 2.3 |
| 5.1 | 5.1 | 5.1 | 5.1 | 5.0 | 4.6 | 4.0 | 3.5 | 3.3 | 3.0 | 2.9 | 2.7 | 2.6 | 2.5 | 2.5 | 2.5 |
| 7.0 | 7.0 | 7.0 | 7.0 | 6.5 | 5.5 | 4.5 | 4.0 | 3.7 | 3.4 | 3.3 | 3.2 | 3.0 | 2.9 | 2.9 | 2.8 |
| 9.3 | 9.3 | 9.3 | 9.0 | 7.7 | 6.0 | 5.0 | 4.4 | 4.2 | 3.9 | 3.8 | 3.6 | 3.5 | 3.3 | 3.3 | 3.2 |
| 12.6 | 12.6 | 12.6 | 11.1 | 8.3 | 6.4 | 5.4 | 4.8 | 4.6 | 4.3 | 4.2 | 4.0 | 3.8 | 3.7 | 3.6 | 3.5 |
| 16.7 | 16.7 | 16.2 | 12.6 | 8.7 | 6.6 | 5.7 | 5.1 | 4.9 | 4.6 | 4.5 | 4.4 | 4.2 | 4.1 | 4.0 | 3.8 |
| 22.3 | 22.3 | 20.1 | 13.4 | 8.9 | 6.8 | 5.9 | 5.4 | 5.2 | 4.9 | 4.8 | 4.6 | 4.4 | 4.3 | 4.2 | 4.1 |
| 30.2 | 29.8 | 23.9 | 13.8 | 9.0 | 7.1 | 6.3 | 5.7 | 5.5 | 5.1 | 5.0 | 4.9 | 4.7 | 4.6 | 4.6 | 4.4 |
| 40.0 | 38.2 | 26.7 | 13.8 | 9.1 | 7.2 | 6.5 | 5.9 | 5.7 | 5.3 | 5.2 | 5.1 | 4.9 | 4.8 | 4.9 | 4.8 |
| 52.7 | 47.6 | 27.7 | 13.7 | 9.3 | 7.5 | 6.7 | 6.2 | 5.9 | 5.6 | 5.4 | 5.2 | 5.0 | 4.9 | 5.0 | 4.9 |
| 64.0 | 57.2 | 27.6 | 13.7 | 9.4 | 7.6 | 6.8 | 6.3 | 6.0 | 5.7 | 5.5 | 5.4 | 5.1 | 5.1 | 5.2 | 5.1 |
| 75.5 | 66.7 | 27.4 | 13.8 | 9.5 | 7.7 | 7.0 | 6.5 | 6.1 | 5.9 | 5.6 | 5.5 | 5.3 | 5.2 | 5.3 | 5.3 |
| 83.9 | 73.0 | 27.4 | 13.9 | 9.6 | 7.8 | 7.0 | 6.5 | 6.2 | 5.9 | 5.7 | 5.6 | 5.4 | 5.3 | 5.4 | 5.4 |
| 87.8 | 74.6 | 27.5 | 14.0 | 9.7 | 7.9 | 7.1 | 6.6 | 6.2 | 6.0 | 5.7 | 5.6 | 5.4 | 5.4 | 5.5 | 5.5 |
| 87.9 | 74.5 | 27.6 | 14.1 | 9.8 | 8.0 | 7.2 | 6.6 | 6.3 | 6.0 | 5.7 | 5.6 | 5.5 | 5.4 | 5.5 | 5.5 |
| 92.2 | 74.4 | 27.5 | 14.1 | 9.8 | 8.0 | 7.2 | 6.6 | 6.3 | 6.0 | 5.7 | 5.6 | 5.5 | 5.4 | 5.5 | 5.5 |

Figure 5.7: Observed background fraction, i.e. the ratio of the numbers of background contamination events and observed data events under the full signal selection, as a function of the minima of allowed $p_T$ and $\Delta p$ values.

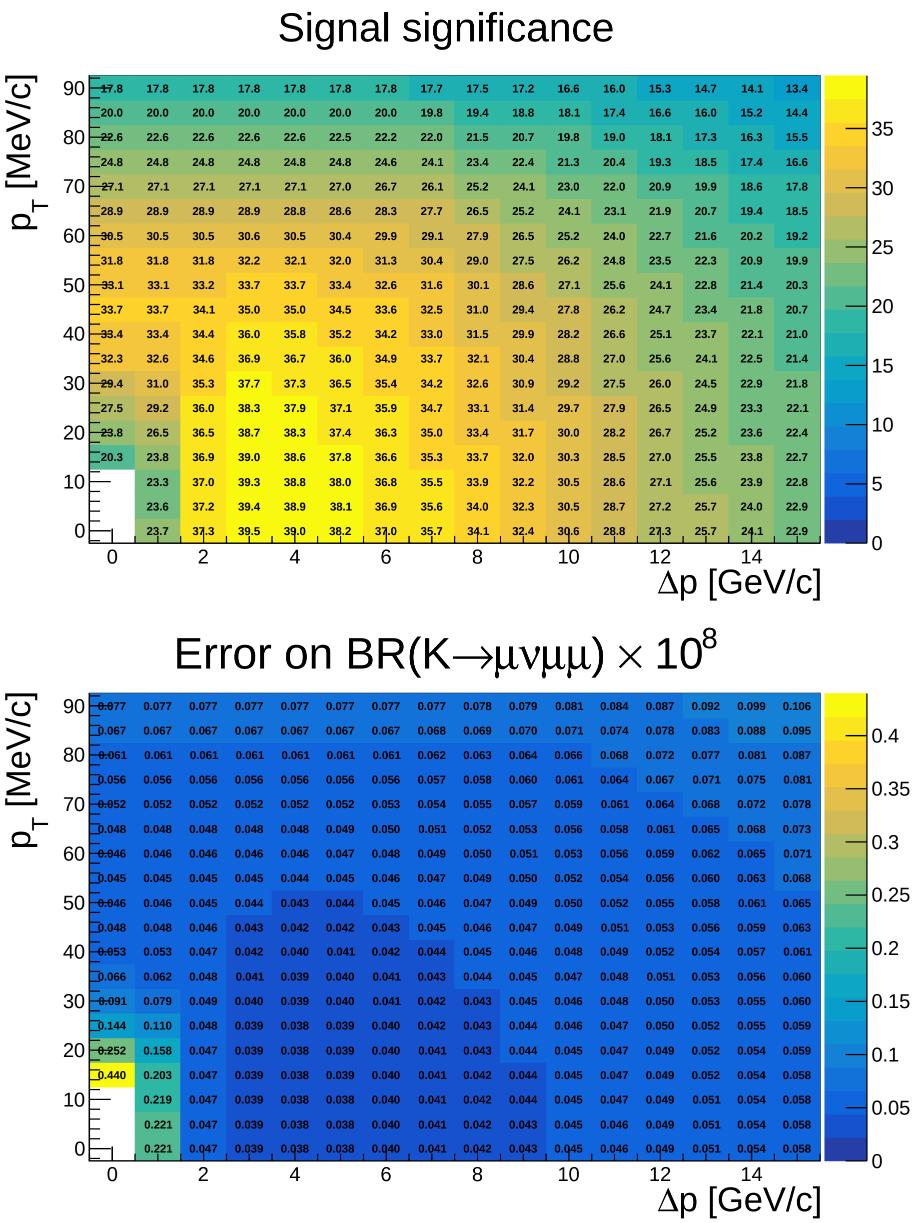

Figure 5.8: Observed signal significance, i.e. $(N_{Data} - N_{Bkgd})/\sqrt{N_{Data}}$, (top) and total error on the measured $\mathfrak{B}_{\mu\nu\mu\mu}$ value (bottom) as a function of the minimum required $p_T$ and $\Delta p$ for a candidate vertex under the signal selection. The total error includes complete treatment of statistical and external uncertainties, with those of systematic origin limited to the contributions of Sections 5.1.2 and 5.7.2.

statistics-limited measurement, the maximum of the quantity corresponds to the minimum of the final uncertainty. The obtained dependence of signal significance is depicted in the top panel of Figure 5.8. The observed dependence as a function of $p_T^{min}$ and $\Delta p^{min}$ shows the presence of a broad local maximum for low transverse momenta and a momentum deficit of $\Delta p^{min} \approx 4$ GeV$/c$. The bottom left corner of the spectrum, corresponding to a background-dominated region, underlines the importance of background rejection.

The full treatment of uncertainties, as defined in Section 5.1.2, including the systematic effect of 5% uncertainty on $N_{Bkgd}$ due to the method of background modelling, covered in Section 5.7.2, allows for investigating the dependence of the total observed error on the $\mathfrak{B}_{\mu\nu\mu\mu}$ measurement on

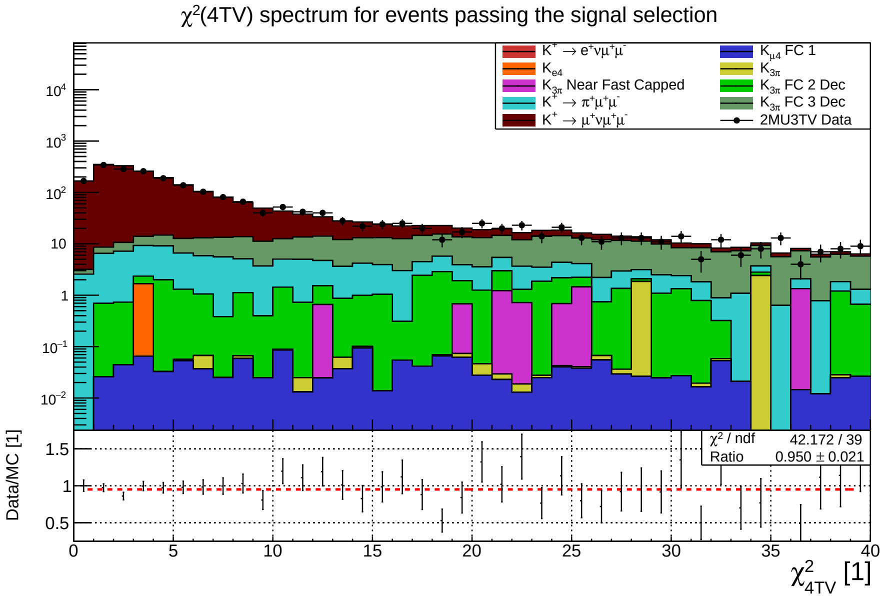

Figure 5.9: Spectrum of $\chi^2(4TV)$ values for data and MC samples under the full signal selection including the final mass cut, with a looser $\chi^2(4TV) < 40$ cut. The $K_{\mu\nu\mu\mu}$ sample was scaled using the theoretically predicted branching ratio of $1.35 \times 10^{-8}$. The plot includes the ratio of data to sum of expected MC events, presented in the bottom panel, together with a one parameter fit.

$p_T^{min}$ and $\Delta p^{min}$. The result is shown in the bottom panel of Figure 5.8. As was the case for signal significance, the observed uncertainty is significant in the background-dominated region. The similar features observed for the two quantities suggests that the dominant source of uncertainty on the $\mathfrak{B}_{\mu\nu\mu\mu}$ measurement is due to signal statistics. A broad local minimum of the total expected error on $\mathfrak{B}_{\mu\nu\mu\mu}$ is found to coincide with the signal significance maximum. This defines the choice of minimum required values of transverse momentum and momentum deficit cuts in the signal selection as

$$p_T^{min} = 0 \text{ MeV}/c \quad \text{and} \quad \Delta p^{min} = 4.0 \text{ GeV}/c. \tag{5.6.3}$$

### 5.6.2 Vertex geometry

The quality of the geometric compatibility of the three muon-identified downstream tracks and a kaon track is defined by the $\chi^2(4TV)$ quantity originating from the vertex-fitting algorithm specified in Section 5.2.2. In background events including in-flight pion decay(s) upstream of the second STRAW chamber giving a non-collinear muon, the original pion direction is misreconstructed. Such events are expected to yield large $\chi^2(4TV)$ values, allowing for further optimisation of the selection procedure.

The spectrum of this variable for data and MC samples under full signal selection with the relaxed cut of $\chi^2(4TV) < 40$ is presented in Figure 5.9. The figure includes a plot of the ratio of data events to sum of scaled contributions from MC samples fitted with a constant. The fit result is consistent with unity only at the $2.5\sigma$ level, mostly due to the use of the theoretically predicted rather than measured $\mathfrak{B}_{\mu\nu\mu\mu}$ value. While quantitative validation of the agreement between real and simulated data spectra is statistically limited, the top panel of Figure 5.9 implies a good qualitative description of the contributing processes. The simulated $K_{\mu\nu\mu\mu}$ events generate a $\chi^2(4TV)$ profile with a prominent peak at low values and a subsequent decay, consistent with accurate reconstruction of the trajectories of the incoming kaon and daughter particle momenta. The majority of considered background modes,

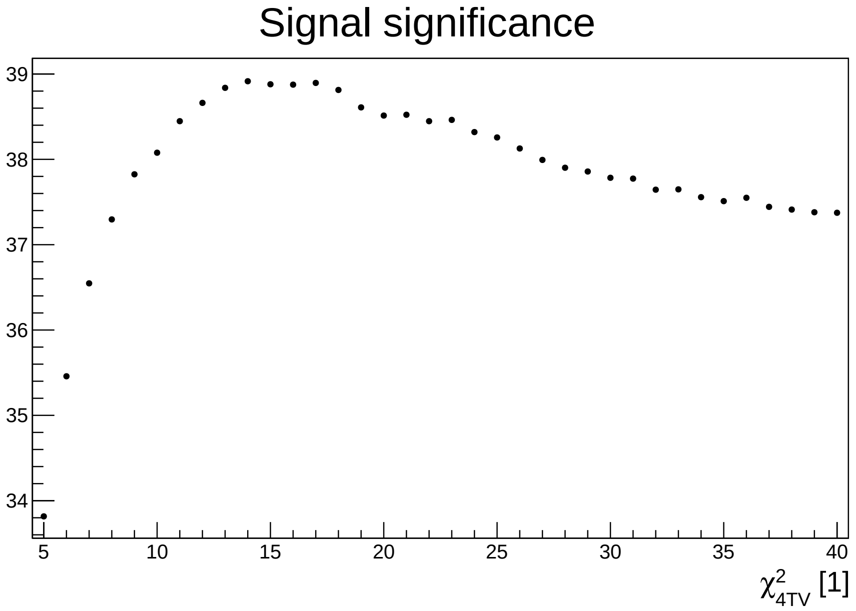

Figure 5.10: Observed signal significance, $(N_{Data} - N_{Bkgd})/\sqrt{N_{Data}}$, as computed for different values of the $\chi^2(4TV)$ cut applied both in normalisation and signal selections.

in particular the dominant $K_{3\pi}$ process with 3 in-flight pion decays, exhibit effectively flat $\chi^2(4TV)$ spectra, underlining the discriminating power of the shown variable.

Contrary to the cut on kinematic properties of the vertex described in the previous section, the $\chi^2(4TV)$ requirement is present in both the normalisation and signal selection. To avoid the systematic impact of different cut values on the quantity for the two selections, the full analysis procedure is followed with the maximum allowed $\chi^2(4TV)$ value spanning

$$\chi^2(4TV)_{max} \in [5, 40], \tag{5.6.4}$$

in units of 1. The upper limit on the variable is defined by the 2MU3TV data filter, while the lower was chosen considering the statistically-limited nature of the $\mathfrak{B}_{\mu\nu\mu\mu}$ measurement. For each cut hypothesis, the signal significance, $(N_{Data} - N_{Bkgd})/\sqrt{N_{Data}}$ is computed, with the result displayed in Figure 5.10. The shown dependence has a clear maximum for $\chi^2(4TV)_{max} = 14$, corresponding to a region in Figure 5.9 where the single-bin contribution from the $K_{\mu\nu\mu\mu}$ decay roughly equals the sum of all background modes. A stricter cut, while further suppressing backgrounds, leads to a reduction in signal acceptance, decreasing the signal significance. A more lenient approach yields a larger fractional increase in the acceptance of background modes as compared to the $K_{\mu\nu\mu\mu}$ decay.

The uncertainty in the $\mathfrak{B}_{\mu\nu\mu\mu}$ measurement was also computed for each $\chi^2(4TV)_{max}$ hypothesis. The dependence of the statistical, systematic and external sources of uncertainty as described in Section 5.1.2, with the inclusion of the background-modelling effect of Section 5.7.2, on $\chi^2(4TV)_{max}$ is shown in Figure 5.11. The statistical uncertainty, in red, decreases with a rise in the maximum allowed $\chi^2(4TV)$ and then nearly plateaus, as expected from the variable spectrum for the simulated $K_{\mu\nu\mu\mu}$ events of Figure 5.9. The external uncertainty follows an opposite trend, with the increase expected given its dependence on background contamination. The systematic uncertainty has a local minimum, arising from competing effects of the normalisation selection ($N^{\pi\mu\mu}_{Cand}$ and $A^{Norm}_{\pi\mu\mu}$) and the

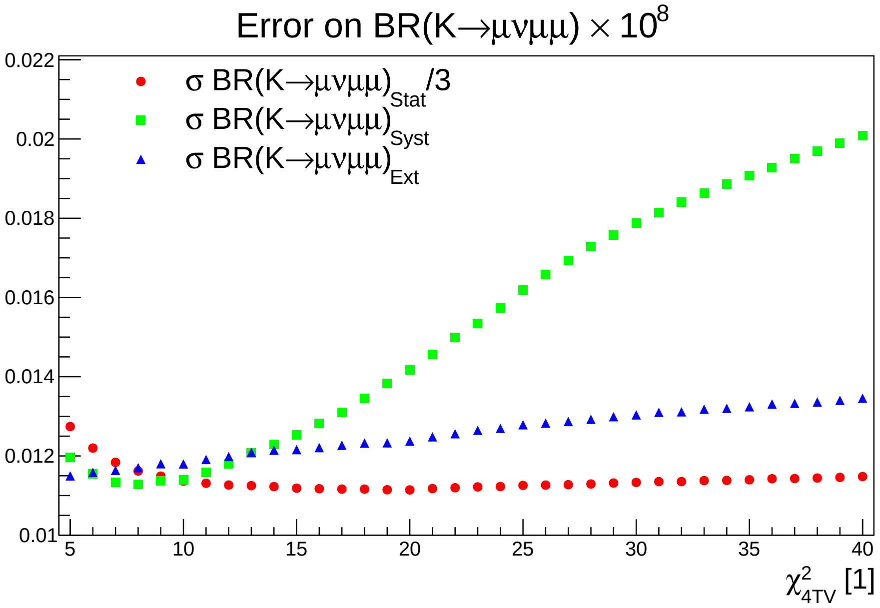

Figure 5.11: Statistical (scaled by 1/3 for presentation purposes), systematic and external uncertainties on the measured $\mathfrak{B}_{\mu\nu\mu\mu}$ as a function of the $\chi^2(4TV)$ cut value. The included uncertainty sources comprise those covered in Section 5.1.2 and systematic effect due to background modelling of Section 5.7.2.

background modelling uncertainty, proportional to the total number of expected background events. The latter phenomenon dominates the large $\chi^2(4TV)_{max}$ regime, leading to an approximately linear dependence. The consideration of signal significance and the expected uncertainty on the $\mathfrak{B}_{\mu\nu\mu\mu}$ measurement motivated the

$$\chi^2(4TV) < 14 \tag{5.6.5}$$

condition for both signal and normalisation selections.

## 5.7 Results

### 5.7.1 $N_K$ measurement

The total number of $K^+$ decays in the FV, $N_K$, for the considered data sample is measured using the $K_{\pi\mu\mu}$ decay. The final kinematic variable used to select normalisation events is the invariant mass of three Spectrometer tracks under mass hypotheses corresponding to $\pi^+$, $\mu^+$ and $\mu^-$ particle identification verdict, $M_{\pi\mu\mu}$. The signal region of the normalisation selection is defined in Equation 5.4.7. The spectrum of $M_{\pi\mu\mu}$ obtained for data and MC samples is shown in Figure 5.12.

The studied $M_{\pi\mu\mu}$ range extends beyond the charged kaon mass, to allow for a verification of the background modelling methods in the normalisation channel. In particular, the region (405 to 460) MeV/$c$ dominated by $K_{3\pi}$ and $K_{\mu4}$ events and well populated for data, suggests a precision of ~2.9% based on the one parameter fit to the ratio of data to sum of MC events shown in the bottom panel of Figure 5.12. In the fitted $M_{\pi\mu\mu}$ range, the $K_{3\pi}$ events with less than two pion decays in flight subject to the forced misID procedure (shown in yellow in Figure 5.12) account for ~13.5% of the total data count. Together with the observed Data/MC ratio, this values validates the forced misID procedure as described in Section 5.5.1.1 as accurate to a factor of <2. Low data statistics for $M_{\pi\mu\mu}$

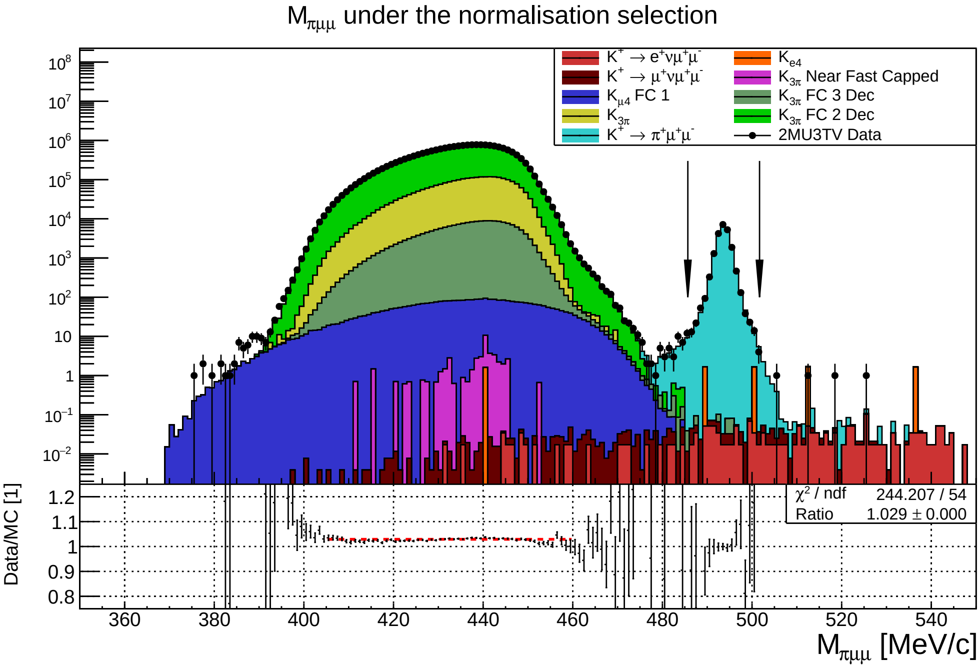

Figure 5.12: Final $M_{\pi\mu\mu}$ spectrum obtained for events passing the normalisation selection with the exclusion of the final mass cut. The ratio of data to summed MC contributions per bin is included in the bottom panel, with a one parameter fit in the region dominated by $K_{3\pi}$ events spanning $M_{\pi\mu\mu} \in [405, 460]$ MeV/$c$. The arrows indicate the signal region.

values above the signal region limit the possibility of verification of the accuracy of the model in that regime. Four data events are observed in the region (502 to 550) MeV/$c$, with the contributions from considered MC samples yielding $9.3 \pm 2.3$.

The expected background contributions to the normalisation signal region are shown in Table 5.5, with the number of data events passing the full normalisation selection being

$$N^{\pi\mu\mu}_{Cand} = 20981. \tag{5.7.1}$$

The total background contribution of $4.2 \pm 2.3$ is negligible compared to the uncertainty arising from signal statistics. The number of data events observed in the signal region is hence taken as the number of observed $K_{\pi\mu\mu}$ decays.

The $K_{\pi\mu\mu}$ mode acceptance under the full normalisation selection is obtained from a MC sample yielding

$$A^{Norm}_{\pi\mu\mu} = (6.466 \pm 0.008) \times 10^{-2}. \tag{5.7.2}$$

The total number of $K^+$ decays in the FV for the considered data sample is calculated from Equation 5.1.4 as

$$N_K = (3.546 \,\pm\, 0.024_{\text{Stat}} \,\pm\, 0.031_{\text{Ext}}) \times 10^{12}, \tag{5.7.3}$$

with the statistical uncertainty due to $N^{\pi\mu\mu}_{Cand}$ and $A^{Norm}_{\pi\mu\mu}$, and the external propagated from $\mathfrak{B}_{\pi\mu\mu}$.

| Sample | Contribution | Acceptance |
|---|---|---|
| $K^+ \to \mu^+\nu\mu^+\mu^-$ | $0.30 \pm 0.03_{\text{Stat}}$ | $6.2 \times 10^{-6}$ |
| $K^+ \to e^+\nu\mu^+\mu^-$ | $0.48 \pm 0.09_{\text{Stat}}$ | $7.9 \times 10^{-6}$ |
| $K_{\mu4}$ FC 1 | $0.01 \pm 0.01_{\text{Stat}}$ | $7.2 \times 10^{-10}$ |
| $K_{e4}$ | $3.2 \pm 2.3_{\text{Stat}}$ | $2.1 \times 10^{-8}$ |
| $K_{3\pi}$ | - | - |
| $K_{3\pi}$ FC 2 Dec | - | - |
| $K_{3\pi}$ FC 3 Dec | $0.17 \pm 0.09_{\text{Stat}}$ | $8.7 \times 10^{-13}$ |
| $K_{3\pi}$ Near Fast Capped | - | - |
| Total | $4.3 \pm 2.3_{\text{Stat}}$ | - |

Table 5.5: Scaled contributions to the normalisation selection signal region and acceptances for the considered MC samples.

### 5.7.2 Number of signal candidates and total background contamination

The final kinematic variable used to select signal events is the squared missing mass of the three muon-identified Spectrometer tracks with respect to the kaon track as measured by the GTK, $M^2_{Miss}(K_{\mu\nu\mu\mu})$. The signal region is defined in Equation 5.4.11. The $M^2_{Miss}(K_{\mu\nu\mu\mu})$ spectra obtained for data and MC samples are presented in Figure 5.13. The investigated $M^2_{Miss}(K_{\mu\nu\mu\mu})$ range extends beyond the region occupied by the $K_{\mu\nu\mu\mu}$ decay, to allow for validation of the background modelling procedure. The processes involving multiple in-fight pion decays, i.e. $K_{3\pi}$ and $K_{\mu4}$, provide broad distributions populating mostly $M^2_{Miss}(K_{\mu\nu\mu\mu})$ values above the signal region, where the position of the maxima and shapes of the tails extending into the signal region heavily depend on the selected vertex kinematics, discussed in Section 5.6. In contrast, the $K_{\pi\mu\mu}$ feature is a narrow peak centered on $M^2_{Miss}(K_{\mu\nu\mu\mu})= 0$. The contribution of upstream $K_{3\pi}$ events with at least two in-flight pion decays is multiple orders of magnitude below that of $K_{3\pi}$ decays in the FV, as expected from the minimum required $Z_{vtx}$ value.

Table 5.6 shows the integral of data events and summed MC contributions in two regions to either side of the signal peak, where the latter is calculated by summing the scaled contributions of all background modes and that of the simulated signal using the theoretically predicated branching ration of Equation 2.4.15. The regions are well separated from the analysis signal region to ensure small contamination of $K_{\mu\nu\mu\mu}$ events, so the compatibility between real and simulated data can be verified for a majority of the background channels.

| $M^2_{Miss}$ range [$10^3$ MeV$^2$] | Data | MC sum |
|---|---|---|
| $[-10, -2]$ | 39 | $37.5 \pm 3.6$ |
| $[2, 20]$ | 191448 | $182052 \pm 155$ |

Table 5.6: Integrals of data events and summed MC contributions in $M^2_{Miss}(K_{\mu\nu\mu\mu})$ regions to both sides of the $K_{\mu\nu\mu\mu}$ signal peak. The summed MC contributions include all background modes and the simulated signal scaled by the predicted SM branching ratio. The uncertainty quoted on the MC value is the sum in quadrature of scaled statistical contributions for individual samples.

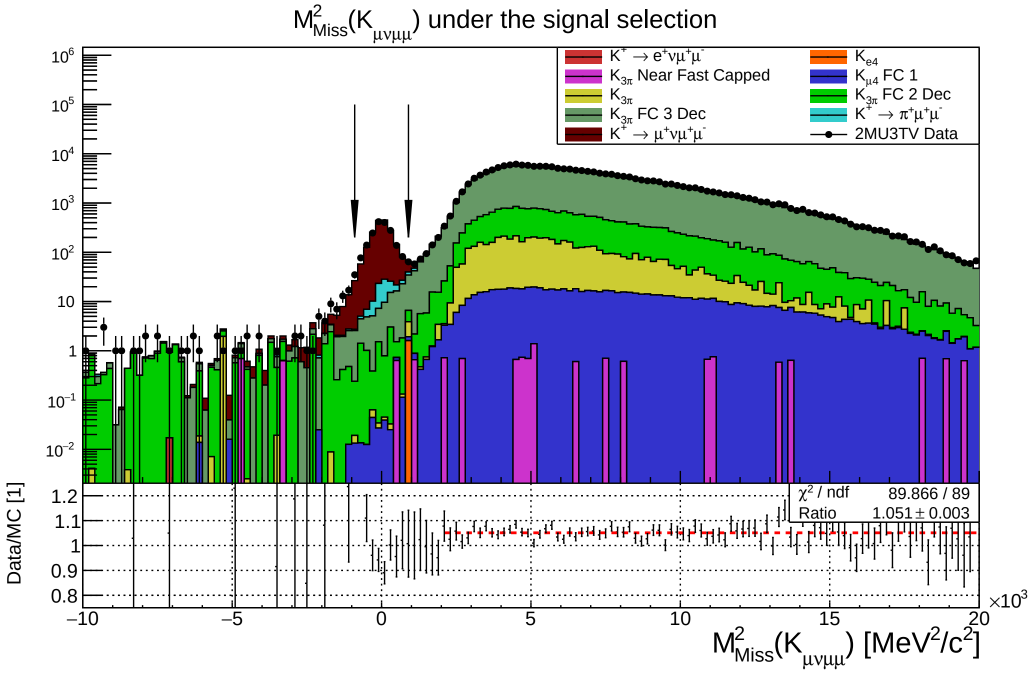

Figure 5.13: Final $M^2_{Miss}$ spectrum obtained for events passing the signal selection with the exclusion of the final mass cut. The ratio of data to summed MC contributions per bin is included in the bottom panel, with a one parameter fit in the region dominated by $K_{3\pi}$ events spanning $M^2_{Miss}(K_{\mu\nu\mu\mu}) \in [2, 20] \times 10^3$ MeV$^2/c^2$. The $K_{\mu\nu\mu\mu}$ sample was scaled using the theoretically predicted branching ratio of $1.35 \times 10^{-8}$. The arrows indicate the signal region.

Integrated values are used in Table 5.6 due to low statistics in the lower $M^2_{Miss}(K_{\mu\nu\mu\mu})$ regime, where the integral counts for data and MC are in agreement. The region dominated by the $K_{3\pi}$ and $K_{\mu4}$ decays, spanning $M^2_{Miss} \in [2, 20] \times 10^3$ MeV$^2$, shows a discrepancy of ∼5% of unknown origin. This difference can also be seen in the one parameter fit to the Data/MC ratio of the bottom panel of Figure 5.13, covering the same range of values. These two arguments motivated the introduction of a systematic uncertainty due to background modelling of the size

$$\sigma^{\text{Syst}}_{N_{Bkgd}} = 0.05 \times N_{Bkgd}, \tag{5.7.4}$$

under the assumption of similar composition of events due to background modes in the fitted $M^2_{Miss}(K_{\mu\nu\mu\mu})$ range and the signal region. This conservative approach consequently applies to the contribution from $K_{\pi\mu\mu}$ decays, which is not present in the investigated $M^2_{Miss}$ regions. Since the uncertainty in the $K_{\pi\mu\mu}$ background is evaluated by applying the signal and normalisation selections on the same MC sample, leading to an expected partial cancellation of systematic effects, it is likely overestimated. An alternative method for estimating the systematic uncertainty in the $K_{\pi\mu\mu}$ contribution remains to be investigated.

The expected background contributions to the signal region of the $K_{\mu\nu\mu\mu}$ selection for all the considered processes are shown in Table 5.7. The three dominant background modes are $K_{3\pi}$ events with three in-flight pion decays, the $K_{\pi\mu\mu}$ decays and $K_{3\pi}$ events with two in-flight pion decays. The small acceptances of the different types of $K_{3\pi}$ processes motivate the use of the "Fast Capped" simulation mode and the forced misID approach. The scaled statistical uncertainties in contributions from the investigated processes, determined by the sizes of the employed MC samples and the event

| Sample | Contribution | Acceptance |
|---|---|---|
| $K^+ \to \pi^+\mu^+\mu^-$ | $65.2 \pm 1.5_{\text{Stat}} \pm 3.3_{\text{Syst}}$ | $2.01 \times 10^{-4}$ |
| $K^+ \to e^+\nu\mu^+\mu^-$ | - | - |
| $K_{\mu 4}$ FC 1 | $0.527 \pm 0.085_{\text{Stat}} \pm 0.036_{\text{Syst}}$ | $3.30 \times 10^{-8}$ |
| $K_{e4}$ | $1.6 \pm 1.6_{\text{Stat}} \pm 0.2_{\text{Syst}}$ | $1.07 \times 10^{-8}$ |
| $K_{3\pi}$ | $0.088 \pm 0.026_{\text{Stat}} \pm 0.005_{\text{Syst}}$ | $4.44 \times 10^{-13}$ |
| $K_{3\pi}$ FC 2 Dec | $11.7 \pm 2.1_{\text{Stat}} \pm 0.6_{\text{Syst}}$ | $5.93 \times 10^{-11}$ |
| $K_{3\pi}$ FC 3 Dec | $87.8 \pm 1.8_{\text{Stat}} \pm 4.5_{\text{Syst}}$ | $4.43 \times 10^{-10}$ |
| $K_{3\pi}$ Near Fast Capped | $0.63 \pm 0.63_{\text{Stat}} \pm 0.03_{\text{Syst}}$ | $3.21 \times 10^{-12}$ |
| Total | $168.0 \pm 3.6_{\text{Stat}} \pm 8.4_{\text{Syst}}$ | - |

Table 5.7: Scaled contributions to the $K_{\mu\nu\mu\mu}$ selection signal region and acceptances from MC samples. The systematic uncertainty in each value originates from the 5% uncertainty of background modelling.

weights, are all of order 1 or below. The systematic uncertainty due to background modelling for the two most prominent background modes exceeds the statistical effect, underlining the appropriate sizes of the utilised MC samples. The total background contamination of the $K_{\mu\nu\mu\mu}$ signal region yields

$$N_{Bkgd} = 168.0 \pm 3.6_{\text{Stat}} \pm 8.4_{\text{Syst}} \pm 0.4_{\text{Ext}}, \tag{5.7.5}$$

where the external uncertainty originates from those on the branching ratios of the considered processes.

The number of data events passing the full signal selection is

$$N_{Data} = 1832. \tag{5.7.6}$$

The relative background contamination is hence 9.2%.

### 5.7.3 $\mathfrak{B}(K^+ \to \mu^+\nu_\mu\mu^+\mu^-)$ with complete statistical and external uncertainty

The acceptance of the $K_{\mu\nu\mu\mu}$ decay under the full signal selection is computed from the simulated data sample as

$$A_{\mu\nu\mu\mu} = (3.590 \pm 0.005) \times 10^{-2}. \tag{5.7.7}$$

Using the results presented in this section and Equation 5.1.2, one arrives at the $K^+ \to \mu^+\nu_\mu\mu^+\mu^-$ branching ratio measurement of

$$\mathfrak{B}(K^+ \to \mu^+\nu\mu^+\mu^-) = (1.307 \pm 0.034_{\text{Stat}} \pm 0.012_{\text{Syst}} \pm 0.012_{\text{Ext}}) \times 10^{-8}, \tag{5.7.8}$$

where the statistical uncertainty is due to the $N_{Cand}$ and $A_{\mu\nu\mu\mu}$ and the external due to the uncertainty on the branching ratios of all other investigated $K^+$ decay modes (dominated by $\mathfrak{B}_{\pi\mu\mu}$). The sources of systematic uncertainty included in Equation 5.7.8 comprise the acceptance and data statistics of the normalisation mode, and the total uncertainty on the background contamination in the signal region. The impact of further systematic effects is discussed in the following section, with the complete result presented in Section 5.9.

## 5.8 Systematic effects

The propagation of uncertainties due to systematic effects arising from data and MC statistics in the normalisation channel as well as the expected background contribution is covered in Section 5.1.2. This section describes the method for quantification of systematic uncertainties due to the trigger system, modelling of the instantaneous beam intensity and the geometric compatibility between upstream (GTK) and downstream (STRAW) spectrometer tracks. All three effects are estimated from the changes in the final measured $\mathfrak{B}_{\mu\nu\mu\mu}$ value and are assumed to be uncorrelated with each other and the remainder of the considered sources of uncertainty.

### 5.8.1 Trigger emulation

The default approach to quantifying the impact of trigger effects on the analysis would involve measurements of the efficiencies of individual algorithms as a function of instantaneous beam intensity and event kinematics for real and simulated data, and estimating the impact of a potential difference. Such a method requires the presence of a minimum bias data sample large enough to contain a statistically significant number of events passing the full signal and normalisation selections. Considering the average ratio of downscaling factors for the minimum bias and di-muon multi-track triggers of ~100 for Run1 NA62 data, a ~5% selection acceptance and a branching ratio of $O(10^{-8})$, the expected yield of such events would be $O(10^1)$. Hence, the default method was deemed inappropriate for the $K_{\mu\nu\mu\mu}$ analysis, instead exercising the similar experimental signatures of the signal and normalisation modes and a common data set used for selection of $K_{\pi\mu\mu}$ and $K_{\mu\nu\mu\mu}$ events.

The trigger emulator decisions for simulated data both at L0 and HLT are neglected, with the remainder of the selection unaltered. The key numerical outputs of the analysis in this scenario, together with the standard results outlined in the previous section, are shown in Table 5.8. The change in the measured total number of $K^+$ decays in the FV is caused by the increase of $A^{Norm}_{\pi\mu\mu}$. The total background estimation for the $K_{\mu\nu\mu\mu}$ signal window does not change, with a marginal fluctuation in background composition. The fractional increase in the signal mode acceptance when excluding trigger emulation is 11.1%, while for the normalisation selection acceptance one obtains a difference of 11.3%.

| Quantity | Standard treatment | No trigger emulators for MC |
|---|---|---|
| $A^{Norm}_{\pi\mu\mu} \times 10^2$ | $6.466 \pm 0.008$ | $7.196 \pm 0.008$ |
| $N_K \times 10^{-12}$ | $3.546 \pm 0.039_{\text{Tot}}$ | $3.187 \pm 0.036_{\text{Tot}}$ |
| $A_{\mu\nu\mu\mu} \times 10^2$ | $3.590 \pm 0.005$ | $3.987 \pm 0.006$ |
| $N_{Bkgd}(K_{3\pi}$ FC 3 Dec$)$ | $87.8 \pm 1.8_{\text{Stat}}$ | $88.2 \pm 1.8_{\text{Stat}}$ |
| $N_{Bkgd}(K_{\pi\mu\mu})$ | $65.2 \pm 1.5_{\text{Stat}}$ | $64.1 \pm 1.4_{\text{Stat}}$ |
| $N_{Bkgd}$ | $168 \pm 9_{\text{Tot}}$ | $168 \pm 9_{\text{Tot}}$ |
| $\mathfrak{B}_{\mu\nu\mu\mu} \times 10^8$ | $1.307 \pm 0.038_{\text{Tot}}$ | $1.310 \pm 0.038_{\text{Tot}}$ |

Table 5.8: Key analysis quantities resultant from the full $K_{\pi\mu\mu}$ and $K_{\mu\nu\mu\mu}$ selections for standard treatment and with the exclusion of trigger emulation for all simulated data. The number of signal and normalisation candidate events in data does not change, hence these figures are not included.

The resultant fractional change to the measured $\mathfrak{B}_{\mu\nu\mu\mu}$ is

$$\frac{|\mathfrak{B}^{Standard}_{\mu\nu\mu\mu} - \mathfrak{B}^{No\,Trig\,Emul}_{\mu\nu\mu\mu}|}{\mathfrak{B}^{Standard}_{\mu\nu\mu\mu}} = \frac{0.003}{1.307} \approx 2.3 \times 10^{-3} = \frac{\sigma^{\text{Syst}}_{Trigger}(\mathfrak{B}_{\mu\nu\mu\mu})}{\mathfrak{B}_{\mu\nu\mu\mu}}, \tag{5.8.1}$$

taken as the systematic uncertainty due to different behaviour of the signal and normalisation events under the emulated trigger conditions.

### 5.8.2 Instantaneous beam intensity modelling

The instantaneous beam intensity is expected to impact the accuracy of signal and normalisation events selections due to multiple different phenomena. The association of accidental signal in the LKr or the MUV3 detectors can lead to changes in the particle identification verdict for a downstream track. The increased number of GTK candidates due to higher beam intensities increases the probability of selecting either a track of a kaon not responsible for the observed decay, or a pion or proton track. Analogously, an increased number of downstream tracks boosts the probability of selecting a halo particle or a decay product of a different $K^+$ as part of the three-track vertex. A larger number of downstream tracks also leads to an increased probability of rejecting an event due to the common selection requirement of component tracks of the selected vertex not being a part of another in-time three-track vertex. The daughter particle identification effect is expected to contribute to both signal and normalisation modes. The upstream track selection should preferentially impact the $K_{\mu\nu\mu\mu}$ selection, due to open kinematics of the final state allowing for a wider range of kaon momenta and directions as compared to the $K_{\pi\mu\mu}$ process. The effect of inclusion of a halo particle track in the three track vertex is expected to be more prominent for the signal selection, due to the halo consisting mostly of muons and the open kinematics of the $K_{\mu\nu\mu\mu}$ final state.

The instantaneous beam intensity, $I_{GTK}$ is calculated per event from the average number of hits per GTK station as observed in the time interval $(-25$ to $25)$ ns with the exclusion of a 5 ns central gap around the trigger time. For simulated data, the per-event value is sampled at random from a distribution obtained from real data contained in a single run, designated as representative for Run1 conditions. In principle, the underlying $I_{GTK}$ distribution could reflect all data collected in the analysed period, with the current central treatment within na62fw motivated by a small expected effect.

The $I_{GTK}$ spectra for data and simulated events passing the full normalisation and signal selections are shown in Figure 5.14. The spectra observed for events passing the full $K_{\pi\mu\mu}$ selection suggest the presence a systematic effect, with the simulated data containing a higher fraction of low intensity events. The effect is evident from the different population for real and simulated events to either side of the maximum shown in the top panel of Figure 5.14 and the resultant ratio of data to summed MC contributions. The limited statistical power of the signal channel data sample, as reflected in the size of error bars in the Data/MC ratio included in the bottom panel of Figure 5.14, precludes a conclusive judgment on the modelling of the beam intensity under the $K_{\mu\nu\mu\mu}$ selection.

The standard approach to correcting for the discrepancy in intensity profiles of real and simulated data would involve a reweighing of the latter based on the relative population of intensity bins. While providing a numerically reliable result, the procedure involves the computational expense of fully reprocessing the simulated data samples. This together with the limited statistical power of the signal event sample motivated a simplified approach, where the simulated data is split into two ranges of

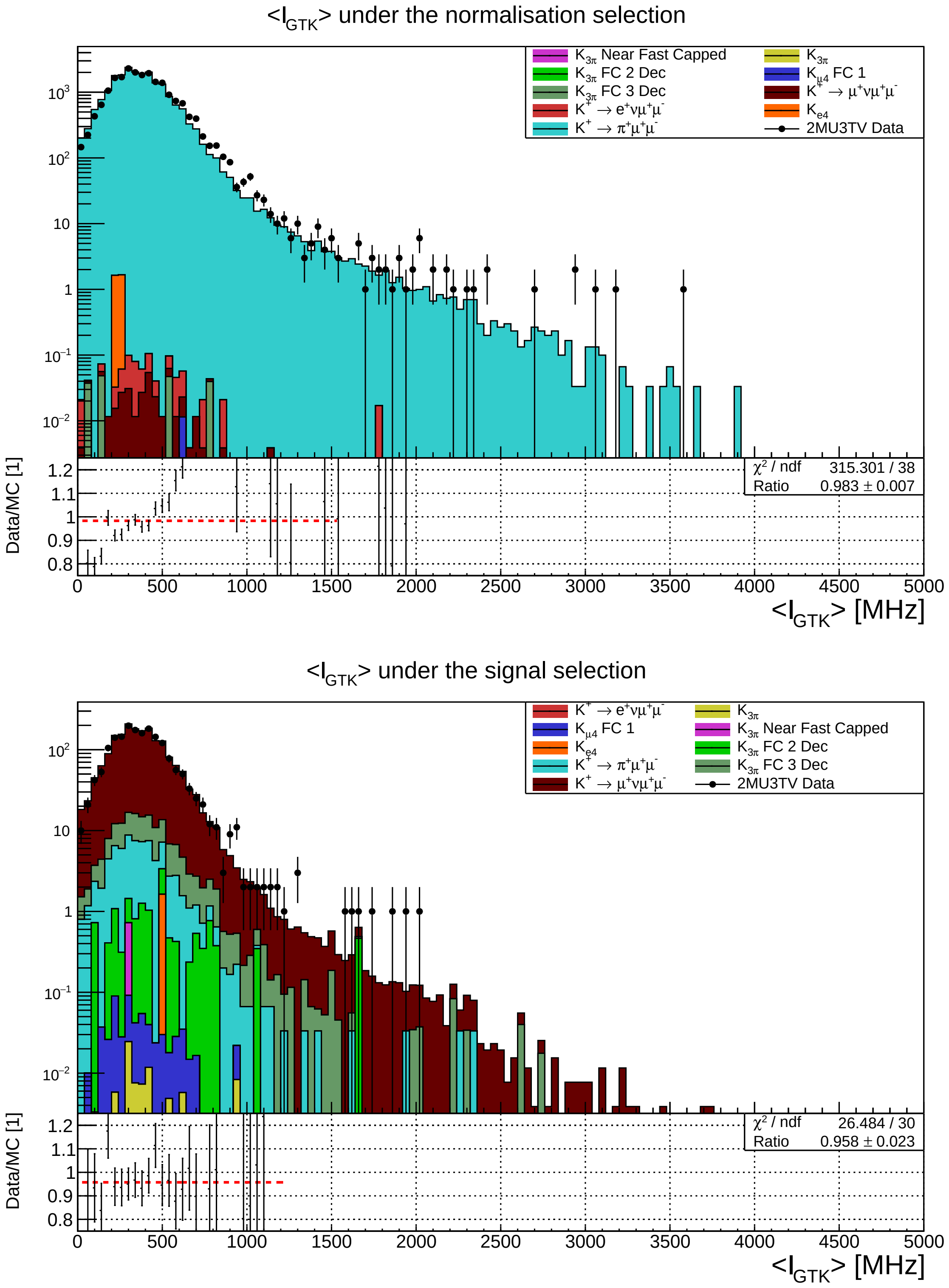

Figure 5.14: Spectra of mean instantaneous beam intensity calculated from GTK hit multiplicity for data and simulated events passing the full signal and normalisation selections. The bottom panel of each plot contains the Data/MC ratio with a constant fit. The $K_{\mu\nu\mu\mu}$ sample was scaled using the theoretically predicted branching ratio of $1.35 \times 10^{-8}$.

| Quantity | $I_{GTK} \leq 400\ MHz$ | $I_{GTK} > 400\ MHz$ | Standard |
|---|---|---|---|
| $A^{Norm}_{\pi\mu\mu} \times 10^2$ | $6.993 \pm 0.011$ | $5.777 \pm 0.011$ | $6.466 \pm 0.008$ |
| $N_K \times 10^{-12}$ | $3.279 \pm 0.037_{\text{Tot}}$ | $3.969 \pm 0.045_{\text{Tot}}$ | $3.546 \pm 0.039_{\text{Tot}}$ |
| $A_{\mu\nu\mu\mu} \times 10^2$ | $3.950 \pm 0.008$ | $3.170 \pm 0.007$ | $3.590 \pm 0.005$ |
| $N_{Bkgd}(K_{3\pi}$ FC 3 Dec$)$ | $80.6 \pm 2.3_{\text{Stat}}$ | $98.9 \pm 2.9_{\text{Stat}}$ | $87.8 \pm 1.8_{\text{Stat}}$ |
| $N_{Bkgd}(K_{\pi\mu\mu})$ | $66.7 \pm 1.9_{\text{Stat}}$ | $63.0 \pm 2.3_{\text{Stat}}$ | $65.2 \pm 1.5_{\text{Stat}}$ |
| $N_{Bkgd}$ | $159 \pm 9_{\text{Tot}}$ | $181 \pm 11_{\text{Tot}}$ | $168 \pm 9_{\text{Tot}}$ |
| $\mathfrak{B}_{\mu\nu\mu\mu} \times 10^8$ | $1.291 \pm 0.037_{\text{Tot}}$ | $1.312 \pm 0.039_{\text{Tot}}$ | $1.307 \pm 0.038_{\text{Tot}}$ |

Table 5.9: Key quantities resultant from the full $K_{\pi\mu\mu}$ and $K_{\mu\nu\mu\mu}$ selections for the full analysis procedure, where either low or high intensity simulated data is used. The number of signal and normalisation candidate events in data does not change, hence these figures are not included.

emulated instantaneous beam intensity, using the boundary value of

$$I^{boundary}_{GTK} = 400 \text{ MHz}. \tag{5.8.2}$$

The real data could also be split into two sub-samples but the uncorrelated uncertainties originating from data statistics in such a case could obscure the impact of instantaneous beam intensity.

The low and high intensity MC sub-samples are then used in the full analysis procedure, together with the complete real data sample. The key numerical outputs of the analyses involving the two MC sub-samples and the standard treatment are presented in Table 5.9. The acceptances of the normalisation and signal modes for only low (high) intensity simulated data change by +8% (−11%) and +10% (−12%) with respect to the standard treatment. This effect can be explained by the vertex selection criterion under which no other downstream tracks forming in-time vertices with the selected three can be present for the event to be accepted. While the dominant sources of background for the $K_{\mu\nu\mu\mu}$ decay retain their hierarchy, the contributions of $K_{3\pi}$ events with three in-flight pion decays increases (decreases) in the high (low) intensity sample by $> 3\sigma_{\text{Stat}}$. These changes account for the majority of the discrepancy in the total background level, $N_{Bkgd}$. The population of $M^2_{Miss}$ regions outside of the $K_{\mu\nu\mu\mu}$ signal region also changes with respect to the standard treatment, see Table 5.10. The low (high) intensity simulated data underestimates (overestimates) the number of observed events in the low $M^2_{Miss}(K_{\mu\nu\mu\mu})$ region. The low intensity sample provides a more complete description in the region dominated by $K_{3\pi}$ and $K_{\mu 4}$ decays, i.e. above the signal region, but still yields an integrated deficit of 3.5%.

| $M^2_{Miss}$ range $[10^3$ MeV$^2]$ | Data | $I_{GTK} \leq 400\ MHz$ | $I_{GTK} > 400\ MHz$ |
|---|---|---|---|
| $[-10, -2]$ | 39 | $26.2 \pm 3.7$ | $53.1 \pm 7.1$ |
| $[2, 20]$ | 191448 | $184969 \pm 202$ | $182098 \pm 244$ |

Table 5.10: Integrals of data events and summed MC contributions for the low and high intensity sub-samples in $M^2_{Miss}(K_{\mu\nu\mu\mu})$ regions to the sides of the $K_{\mu\nu\mu\mu}$ signal peak. The uncertainty quoted on the MC values is the sum in quadrature of individual scaled sample contributions.

The differences arising from using the separated low and high intensity sub-samples motivate the introduction of a systematic uncertainty due to intensity modelling, $\sigma^{\text{Syst}}_{Intensity}(\mathfrak{B}_{\mu\nu\mu\mu})$, as the maximum of the difference between one sub-sample and the central result

$$\frac{\sigma^{\text{Syst}}_{Intensity}(\mathfrak{B}_{\mu\nu\mu\mu})}{\mathfrak{B}_{\mu\nu\mu\mu}} = \frac{\max(|\mathfrak{B}^{Standard}_{\mu\nu\mu\mu} - \mathfrak{B}^{Int}_{\mu\nu\mu\mu}|)}{\mathfrak{B}^{Standard}_{\mu\nu\mu\mu}} = \frac{0.016}{1.307} \approx 1.22 \times 10^{-2}. \tag{5.8.3}$$

### 5.8.3 Vertex geometry requirement

As discussed in Section 5.6.2, the common selection requirement on the geometric consistency between one upstream and three downstream tracks combining to form a vertex candidate presents the opportunity of background rejection. The described scan procedure also allows for a check on stability of key analysis quantities as a function of $\chi^2(4TV)$, which can serve as an indirect method of estimating the systematic uncertainty due to the geometric compatibility between upstream (GTK) and downstream (STRAW) spectrometer tracks. The impact of the timing cut on the GTK candidate can be neglected, as the permitted range of $t_{GTK} - t_{KTAG}$ values exceeds the relative resolution of the two systems by factor $\sim$8. A number of phenomena can contribute to this systematic effect: a discrepancy between real and simulated data in both the normalisation or signal channels and different behaviour of $K_{\mu\nu\mu\mu}$ signal events and the expected background under the $\chi^2(4TV)$ requirement.

To complement the statistically limited spectrum of $\chi^2(4TV)$ under the full $K_{\mu\nu\mu\mu}$ selection with a loosened upper bound on the target quantity (see Figure 5.9), one can also investigate the agreement between $\chi^2(4TV)$ profiles obtained from real and simulated data under the normalisation selection, see Figure 5.15. With the normalisation channel being effectively background free, the included ratio

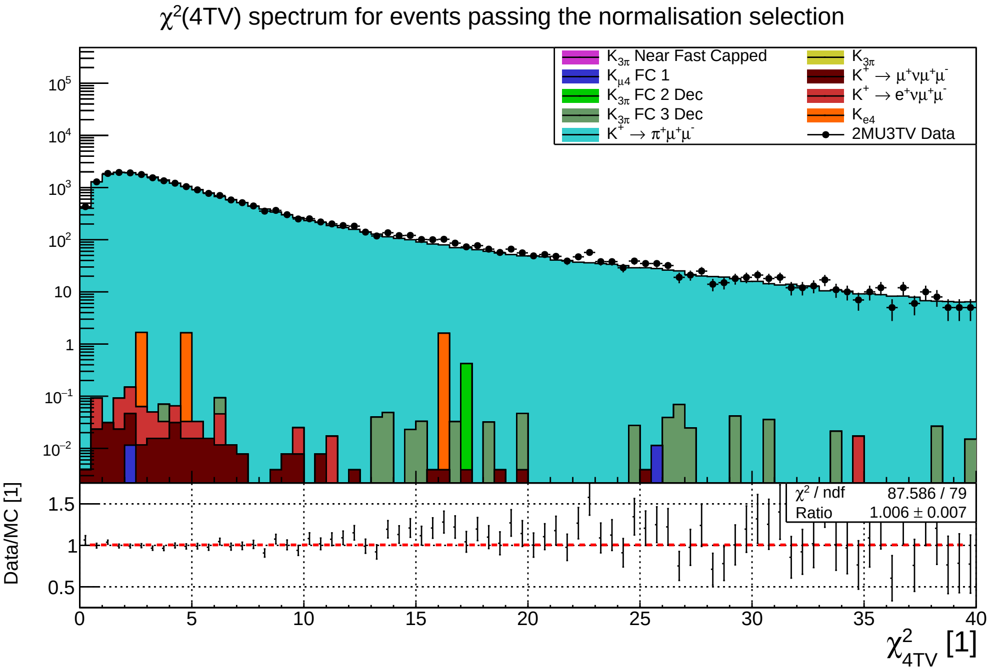

Figure 5.15: Spectrum of $\chi^2(4TV)$ values for data and MC samples under the full normalisation selection including the final mass cut, with a looser $\chi^2(4TV) < 40$ cut. The $K_{\mu\nu\mu\mu}$ sample was scaled using the theoretically predicted branching ratio of $1.35 \times 10^{-8}$. The plot includes the ratio of data to sum of MC events, presented in the bottom panel, together with a constant fit.

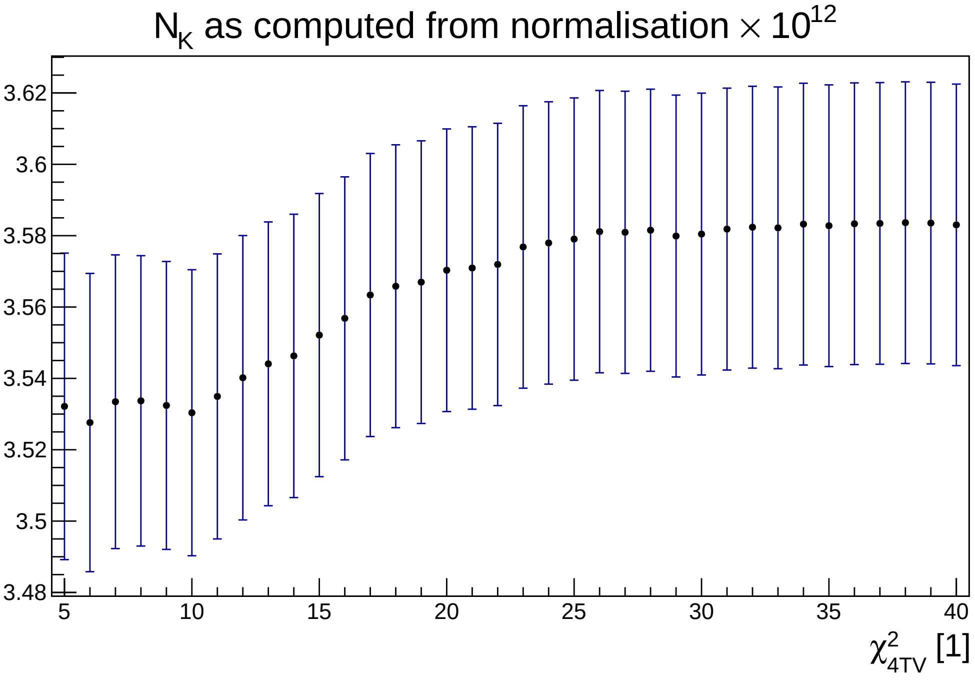

Figure 5.16: Number of $K^+$ decays in the FV as computed from the $K_{\pi\mu\mu}$ channel including the total error as a function of the maximum allowed $\chi^2(4TV)$ value, quantifying the geometric compatibility of the three downstream and one upstream tracks used to define a candidate vertex.

of real to simulated data events enables a verification of the accuracy of simulating the $K_{\pi\mu\mu}$ events. While the constant fit yields a result consistent with unity, an overabundance of real data events can be observed for $\chi^2(4TV) \gtrsim 10$, both in the spectra and the included ratio of data to summed MC contributions.

The observed pattern motivated the investigation of the dependence of the number of $K^+$ decays in the FV, $N_K$, on the upper bound on the $\chi^2(4TV)$ quantity, with the result shown in Figure 5.16. While the range of obtained $N_K$ values spans $\pm\sigma$ from the final result, a clear trend can be observed. Between $\chi^2(4TV)$ of 10 and 20, the measured $N_K$ increases steadily. This result is purely due to a different dependence of $N^{\pi\mu\mu}_{Cand}$ and $A^{Norm}_{\pi\mu\mu}$ on the maximum allowed $\chi^2(4TV)$ value, as the background contamination in the normalisation channels remains $< 10$ for all investigated values.

To quantify the impact of the geometric compatibility requirement on the full $K_{\mu\nu\mu\mu}$ analysis procedure, the variation in the final measured $\mathfrak{B}_{\mu\nu\mu\mu}$ was investigated, see Figure 5.17. Note that the final result is sensitive to both discrepancies between real and simulated data, cancellations between the signal and normalisation channels, and the expected background contribution. The final quantity was observed to increase from ∼4% to ∼20% of the total real data count in the $K_{\mu\nu\mu\mu}$ signal region under the $\chi^2(4TV)$ scan. The $\mathfrak{B}_{\mu\nu\mu\mu}$ values of Figure 5.17 are fully contained within one total uncertainty on the central result (Equation 5.7.8). The fluctuations in $\mathfrak{B}_{\mu\nu\mu\mu}$ for neighbouring $\chi^2(4TV)$ bins show the impact of limited signal statistics. A decreasing pattern can be seen for $\chi^2(4TV) > 14$, corresponding to the opposite behaviour of the $N_K$ dependence presented in Figure 5.16. The uncertainty on the measured $\mathfrak{B}_{\mu\nu\mu\mu}$ due to the vertex geometry requirement including the use of GTK information, $\sigma^{\text{Syst}}_{Geometry}(\mathfrak{B}_{\mu\nu\mu\mu})$, is hence estimated as half of the difference between the lowest and highest values

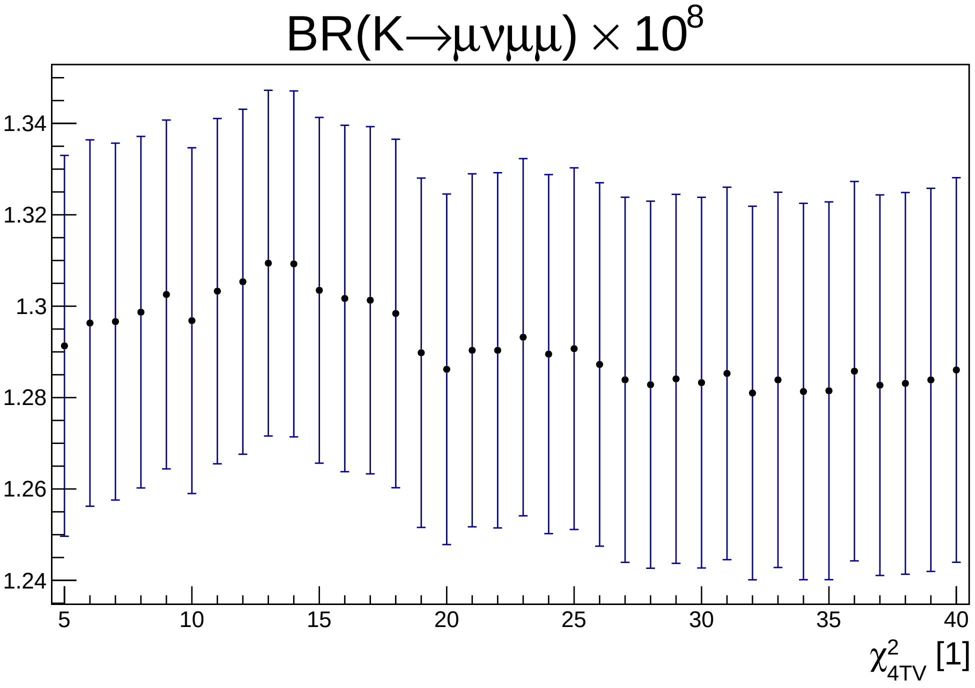

Figure 5.17: Measured $\mathfrak{B}_{\mu\nu\mu\mu}$ as a function of the maximum allowed $\chi^2(4TV)$ value, quantifying the geometric compatibility of the three downstream and one upstream tracks used to define a candidate vertex. The error bars represent the sum in quadrature of statistical, external and systematic uncertainties, where the latter includes only the normalisation and background estimate statistical effects and the uncertainty due to the method of modelling the background in the $K_{\mu\nu\mu\mu}$ channel.

observed under the vertex geometry study,

$$\frac{\sigma^{\text{Syst}}_{Geometry}(B_{\mu\nu\mu\mu})}{B_{\mu\nu\mu\mu}} = \frac{\max(B^{\chi^2(4TV)\ scan}_{\mu\nu\mu\mu}) - \min(B^{\chi^2(4TV)\ scan}_{\mu\nu\mu\mu})}{2 \times B_{\mu\nu\mu\mu}} = \frac{0.030}{2 \times 1.307} \approx 1.15 \times 10^{-2}. \quad (5.8.4)$$

## 5.9 $\mathfrak{B}(K^+ \to \mu^+\nu_\mu\mu^+\mu^-)$ with an error budget

The error budget for the measurement of the $K^+ \to \mu^+\nu_\mu\mu^+\mu^-$ branching ratio on Run1 NA62 data collected with the di-muon multi-track trigger stream is presented in Table 5.11. For classification of different sources of uncertainty and employed error propagation methods refer to Section 5.1.2. The measured values for statistical and systematic contributions subject to the propagation are contained in Section 5.7. The uncertainties on the branching ratios used for calculation of the number of kaon decay in the FV and estimation of the expected background contamination in the signal channel, which are used to quantify the external contribution, are listed in Table 5.2. The evaluation of systematic effects due to trigger emulation, instantaneous beam intensity modelling and the vertex geometry requirement is covered in Section 5.8. The full result using the $K_{\pi\mu\mu}$ decay as the normalisation channel with 1832 $K_{\mu\nu\mu\mu}$ candidate events observed in data and an expected background contribution of $168 \pm 9$ yields

$$\mathfrak{B}(K^+ \to \mu^+\nu_\mu\mu^+\mu^-)^{NA62\ Run1}_{exp} = (1.307 \pm 0.034_{Stat} \pm 0.025_{\text{Syst}} \pm 0.012_{\text{Ext}}) \times 10^{-8}. \quad (5.9.1)$$

| Source | Absolute value [$10^{-8}$] | Fractional value [%] |
|---|---|---|
| Data statistical | 0.034 | 2.60 |
| MC statistical | 0.002 | 0.15 |
| **Total statistical** | **0.034** | **2.60** |
| $N_K$ data statistical | 0.010 | 0.77 |
| $N_K$ MC statistical | 0.003 | 0.23 |
| Background MC statistical | 0.003 | 0.23 |
| Background modelling | 0.007 | 0.54 |
| Trigger emulation | 0.003 | 0.23 |
| Beam intensity modelling | 0.016 | 1.22 |
| Vertex geometry requirement | 0.015 | 1.15 |
| **Total systematic** | **0.025** | **1.91** |
| Error on $\mathfrak{B}_i$ for $i \in MC$ | 0.012 | 0.92 |
| **Total external** | **0.012** | **0.92** |
| **TOTAL** | **0.044** | **3.37** |

Table 5.11: The complete error budget for the $\mathfrak{B}_{\mu\nu\mu\mu}$ value measured on Run1 NA62 data. The fractional uncertainty is calculated with respect to the central value of $1.307 \times 10^{-8}$ after the absolute values are propagated and rounded to one-hundredth of a percent. The individual absolute contributions are summed in quadrature.

## 5.10 Discussion

The measured $K^+ \to \mu^+\nu_\mu\mu^+\mu^-$ branching fraction of $(1.307 \pm 0.044_{\mathrm{Tot}}) \times 10^{-8}$ agrees with the most up-to-date theoretical prediction (see Equation 2.4.15) to one standard deviation, with further quantification of the agreement impeded by no uncertainty provided for the Standard Model value [10].

The $K_{\pi\mu\mu}$ normalisation channel provides the largest contribution to the external uncertainty, which is a consequence of the small background contamination in the signal channel, as outlined in Table 5.1. The data analysed for this work is part of the sample used to provide the used $\mathfrak{B}_{\pi\mu\mu}$ value [2], where the total uncertainty was dominated by data statistics, with 27 679 candidate events observed and no usage of GTK information. The current conservative approach involves a combination of the error on the branching ratio with the uncertainty on normalisation channel data statistics under the assumption of uncorrelated data sets, leading to an overestimation of the total uncertainty. The precise quantification of the correlation between the data sets, while technically difficult, will allow for an exact treatment.

The second and third largest contributions to the measurement uncertainty are due to beam intensity modelling and vertex geometry requirement respectively. Both were quantified using simplified approaches. The beam intensity modelling effect can be validated by investigating the full analysis results using simulated data reweighed to account for the observed discrepancy. A similar method could be applied to verify the impact of the vertex geometry requirement, with the normalisation channel used to quantify the discrepancy between real and simulated data.

The uncertainty due to trigger effects was estimated by neglecting the emulation for simulated data and verifying the stability of the final result. The obtained fractional uncertainty of 0.23% differs from the result of a significantly more involved approach of the $K_{\pi\mu\mu}$ analysis [2], yielding 0.19% for the combined effect of L0 and L1 trigger efficiencies. The small discrepancy enhances the reliability of the presented estimate, given limited data statistics in both signal and normalisation channels of the $K_{\mu\nu\mu\mu}$ analysis.

The presented result was obtained by analysing Run1 NA62 data. The ongoing Run2 data-collection campaign promises a significantly larger sample of $K_{\mu\nu\mu\mu}$ events, reducing the dominant source of uncertainty. The combination of Run1 and Run2 data is not a trivial endeavour due differences in the experimental setup, a change to di-muon multi-track trigger line and variations in the beam intensity for the latter sample.

Once all the outlined issues are addressed, the feasibility of extracting information on the form factors relevant to the $K^+ \to \mu^+\nu_\mu\mu^+\mu^-$ decay (see Section 2.4.2) will be investigated. The $K_{\mu\nu\mu\mu}$ data sample can also be used to conduct a search for a BSM muon-philic force carrier, as described in Section 2.4.3. The search was not performed as part of the presented work due to time constraints and the expected higher sensitivity in case of the inclusion of Run2 NA62 data, the feasibility of which will be investigated.

# Chapter 6

# Conclusion

The complete software package for the ANTI-0 detector developed by the author within the NA62 software framework is described, including detector simulation, algorithms for data reconstructions and analysis-level tools for associating ANTI-0 signals with STRAW tracks and measuring the performance of the system. The software enabled the verification of ANTI-0 data quality during the commissioning period and subsequent operation from 2021 onwards, and the use of ANTI-0 information in searches for the presence of a Dark Photon on NA62 data collected in 2021 [105] [106]. The ANTI-0 performance in 2021, 2022 and 2023 is summarised, characterised by a long-term efficiency of 98% and a time resolution of 600 ps.

The first observation of the rare $K^+ \to \mu^+\nu_\mu\mu^+\mu^-$ decay was achieved by analysing Run1 (2017 and 2018) NA62 data, with the number of data candidate events of 1832 and a background contamination of $168 \pm 9$. The measured branching ratio of

$$\mathfrak{B}(K^+ \to \mu^+\nu_\mu\mu^+\mu^-)_{exp}^{NA62\ Run1} = (1.307 \pm 0.034_{\text{Stat}} \pm 0.025_{\text{Syst}} \pm 0.012_{\text{Ext}}) \times 10^{-8}$$

agrees with the most up-to-date SM prediction [10]. The uncertainty on the measurement is dominated by data sample size, with the two largest systematic effects arising from the modelling of instantaneous beam intensity and the geometric compatibility between upstream (GTK) and downstream (STRAW) spectrometer tracks. The $K^+ \to \pi^+\mu^+\mu^-$ decay was used as the normalisation channel, with the error on $\mathfrak{B}(K^+ \to \pi^+\mu^+\mu^-)$ dominating the external uncertainty contributions. The $K^+ \to \mu^+\nu_\mu\mu^+\mu^-$ data set will be subject to further studies on the sensitivity to kaon radiative form factors and phase space reach into new physics models capable of addressing the $(g-2)_\mu$ anomaly [11].

# Bibliography

[1] E. Cortina Gil et al. “Measurement of the very rare $K^+ \to \pi^+\nu\bar{\nu}$ decay”. In: *Journal of High Energy Physics* 2021.6 (June 2021). ISSN: 1029-8479. DOI: `10.1007/jhep06(2021)093`. URL: `http://dx.doi.org/10.1007/JHEP06(2021)093`.

[2] E. Cortina Gil et al. “A measurement of the $K^+ \to \pi^+\mu^+\mu^-$ decay”. In: *Journal of High Energy Physics* 2022.11 (Nov. 2022). ISSN: 1029-8479. DOI: `10.1007/jhep11(2022)011`. URL: `http://dx.doi.org/10.1007/JHEP11(2022)011`.

[3] J. H. Christenson et al. “Evidence for the $2\pi$ Decay of the $K_2^0$ Meson”. In: *Phys. Rev. Lett.* 13 (4 July 1964), pp. 138–140. DOI: `10.1103/PhysRevLett.13.138`. URL: `https://link.aps.org/doi/10.1103/PhysRevLett.13.138`.

[4] Makoto Kobayashi and Toshihide Maskawa. “CP-Violation in the Renormalizable Theory of Weak Interaction”. In: *Progress of Theoretical Physics* 49.2 (Feb. 1973), pp. 652–657. DOI: `10.1143/PTP.49.652`. URL: `https://doi.org/10.1143/PTP.49.652`.

[5] S. Abachi et al. “Observation of the Top Quark”. In: *Phys. Rev. Lett.* 74 (14 Apr. 1995), pp. 2632–2637. DOI: `10.1103/PhysRevLett.74.2632`. URL: `https://link.aps.org/doi/10.1103/PhysRevLett.74.2632`.

[6] F. Abe et al. “Observation of Top Quark Production in $\overline{p}p$ Collisions with the Collider Detector at Fermilab”. In: *Phys. Rev. Lett.* 74 (14 Apr. 1995), pp. 2626–2631. DOI: `10.1103/PhysRevLett.74.2626`. URL: `https://link.aps.org/doi/10.1103/PhysRevLett.74.2626`.

[7] G. Aad et al. “Observation of a new particle in the search for the Standard Model Higgs boson with the ATLAS detector at the LHC”. In: *Physics Letters B* 716.1 (2012), pp. 1–29. ISSN: 0370-2693. DOI: `https://doi.org/10.1016/j.physletb.2012.08.020`. URL: `https://www.sciencedirect.com/science/article/pii/S037026931200857X`.

[8] S. Chatrchyan et al. “Observation of a new boson at a mass of 125 GeV with the CMS experiment at the LHC”. In: *Physics Letters B* 716.1 (2012), pp. 30–61. ISSN: 0370-2693. DOI: `https://doi.org/10.1016/j.physletb.2012.08.021`. URL: `https://www.sciencedirect.com/science/article/pii/S0370269312008581`.

[9] Andrzej J. Buras et al. “Can we reach the Zeptouniverse with rare K and B s,d decays?” In: *Journal of High Energy Physics* 2014.11 (Nov. 2014). ISSN: 1029-8479. DOI: `10.1007/jhep11(2014)121`. URL: `http://dx.doi.org/10.1007/JHEP11(2014)121`.

[10] J. Bijnens, G. Ecker, and J. Gasser. “Radiative semileptonic kaon decays”. In: *Nuclear Physics B* 396.1 (May 1993), pp. 81–118. ISSN: 0550-3213. DOI: `10.1016/0550-3213(93)90259-r`. URL: `http://dx.doi.org/10.1016/0550-3213(93)90259-R`.

[11] Gordan Krnjaic et al. "Probing Muonphilic Force Carriers and Dark Matter at Kaon Factories". In: *Physical Review Letters* 124.4 (Jan. 2020). ISSN: 1079-7114. DOI: `10.1103/physrevlett.124.041802`. URL: `http://dx.doi.org/10.1103/PhysRevLett.124.041802`.

[12] John Campbell, Joey Huston, and Frank Krauss. *The Black Book of Quantum Chromodynamics: A Primer for the LHC Era*. Oxford University Press, Dec. 2017. ISBN: 9780199652747. DOI: `10.1093/oso/9780199652747.001.0001`. URL: `https://doi.org/10.1093/oso/9780199652747.001.0001`.

[13] R. L. Workman et al. "Review of Particle Physics". In: *PTEP* 2022 (2022), p. 083C01. DOI: `10.1093/ptep/ptac097`.

[14] C. A. Baker et al. "Improved Experimental Limit on the Electric Dipole Moment of the Neutron". In: *Physical Review Letters* 97.13 (Sept. 2006). ISSN: 1079-7114. DOI: `10.1103/physrevlett.97.131801`. URL: `http://dx.doi.org/10.1103/PhysRevLett.97.131801`.

[15] J. M. Pendlebury et al. "Revised experimental upper limit on the electric dipole moment of the neutron". In: *Physical Review D* 92.9 (Nov. 2015). ISSN: 1550-2368. DOI: `10.1103/physrevd.92.092003`. URL: `http://dx.doi.org/10.1103/PhysRevD.92.092003`.

[16] Sheldon L. Glashow. "Partial-symmetries of weak interactions". In: *Nuclear Physics* 22.4 (1961), pp. 579–588. ISSN: 0029-5582. DOI: `https://doi.org/10.1016/0029-5582(61)90469-2`. URL: `https://www.sciencedirect.com/science/article/pii/0029558261904692`.

[17] Peter W. Higgs. "Broken Symmetries and the Masses of Gauge Bosons". In: *Phys. Rev. Lett.* 13 (16 Oct. 1964), pp. 508–509. DOI: `10.1103/PhysRevLett.13.508`. URL: `https://link.aps.org/doi/10.1103/PhysRevLett.13.508`.

[18] Lincoln Wolfenstein. "Parametrization of the Kobayashi-Maskawa Matrix". In: *Phys. Rev. Lett.* 51 (21 Nov. 1983), pp. 1945–1947. DOI: `10.1103/PhysRevLett.51.1945`. URL: `https://link.aps.org/doi/10.1103/PhysRevLett.51.1945`.

[19] V. C. Rubin, Jr. Ford W. K., and N. Thonnard. "Rotational properties of 21 SC galaxies with a large range of luminosities and radii, from NGC 4605 (R=4kpc) to UGC 2885 (R=122kpc)." In: *The Astrophysical Journal* 238 (June 1980), pp. 471–487. DOI: `10.1086/158003`.

[20] Douglas Clowe et al. "A Direct Empirical Proof of the Existence of Dark Matter*". In: *The Astrophysical Journal* 648.2 (Aug. 2006), p. L109. DOI: `10.1086/508162`. URL: `https://dx.doi.org/10.1086/508162`.

[21] Marco Cirelli, Alessandro Strumia, and Jure Zupan. *Dark Matter*. 2024. arXiv: `2406.01705 [hep-ph]`. URL: `https://arxiv.org/abs/2406.01705`.

[22] Andrei D Sakharov. "Violation of CP invariance, C asymmetry, and baryon asymmetry of the universe". In: *Soviet Physics Uspekhi* 34.5 (May 1991), p. 392. DOI: `10.1070/PU1991v034n05ABEH002497`. URL: `https://dx.doi.org/10.1070/PU1991v034n05ABEH002497`.

[23] Y. Fukuda et al. "Evidence for Oscillation of Atmospheric Neutrinos". In: *Phys. Rev. Lett.* 81 (8 Aug. 1998), pp. 1562–1567. DOI: `10.1103/PhysRevLett.81.1562`. URL: `https://link.aps.org/doi/10.1103/PhysRevLett.81.1562`.

[24] Q. R. Ahmad et al. "Measurement of the Rate of $\nu_e + d \rightarrow p + p + e^-$ Interactions Produced by $^8B$ Solar Neutrinos at the Sudbury Neutrino Observatory". In: *Phys. Rev. Lett.* 87 (7 July 2001), p. 071301. DOI: `10.1103/PhysRevLett.87.071301`. URL: `https://link.aps.org/doi/10.1103/PhysRevLett.87.071301`.

[25] Q. R. Ahmad et al. “Direct Evidence for Neutrino Flavor Transformation from Neutral-Current Interactions in the Sudbury Neutrino Observatory”. In: *Phys. Rev. Lett.* 89 (1 June 2002), p. 011301. DOI: `10.1103/PhysRevLett.89.011301`. URL: `https://link.aps.org/doi/10.1103/PhysRevLett.89.011301`.

[26] B. Pontecorvo. “Inverse beta processes and nonconservation of lepton charge”. In: *Zh. Eksp. Teor. Fiz.* 34 (1957), p. 247.

[27] Ziro Maki, Masami Nakagawa, and Shoichi Sakata. “Remarks on the Unified Model of Elementary Particles”. In: *Progress of Theoretical Physics* 28.5 (Nov. 1962), pp. 870–880. ISSN: 0033-068X. DOI: `10.1143/PTP.28.870`. URL: `https://doi.org/10.1143/PTP.28.870`.

[28] T. Aoyama et al. “The anomalous magnetic moment of the muon in the Standard Model”. In: *Physics Reports* 887 (Dec. 2020), pp. 1–166. ISSN: 0370-1573. DOI: `10.1016/j.physrep.2020.07.006`. URL: `http://dx.doi.org/10.1016/j.physrep.2020.07.006`.

[29] Yonatan Kahn et al. “M3: a new muon missing momentum experiment to probe $(g2)_\mu$ and dark matter at Fermilab”. In: *Journal of High Energy Physics* 2018.9 (Sept. 2018). ISSN: 1029-8479. DOI: `10.1007/jhep09(2018)153`. URL: `http://dx.doi.org/10.1007/JHEP09(2018)153`.

[30] D. P. Aguillard et al. “Measurement of the Positive Muon Anomalous Magnetic Moment to 0.20 ppm”. In: *Phys. Rev. Lett.* 131 (16 Oct. 2023), p. 161802. DOI: `10.1103/PhysRevLett.131.161802`. URL: `https://link.aps.org/doi/10.1103/PhysRevLett.131.161802`.

[31] Thomas DeGrand and Carleton DeTar. *Lattice Methods for Quantum Chromodynamics*. Sept. 2006, pp. 1–346. ISBN: 978-981-256-727-7. DOI: `10.1142/6065`.

[32] Sz. Borsanyi et al. “Leading hadronic contribution to the muon magnetic moment from lattice QCD”. In: *Nature* 593.7857 (Apr. 2021), pp. 51–55. ISSN: 1476-4687. DOI: `10.1038/s41586-021-03418-1`. URL: `http://dx.doi.org/10.1038/s41586-021-03418-1`.

[33] G. D. Rochester and C. C. Butler. “Evidence for the Existence of New Unstable Elementary Particles”. In: *Nature* 160 (1947), pp. 855–857. DOI: `10.1038/160855a0`.

[34] S. L. Glashow, J. Iliopoulos, and L. Maiani. “Weak Interactions with Lepton-Hadron Symmetry”. In: *Phys. Rev. D* 2 (7 Oct. 1970), pp. 1285–1292. DOI: `10.1103/PhysRevD.2.1285`. URL: `https://link.aps.org/doi/10.1103/PhysRevD.2.1285`.

[35] Mikołaj Misiak and Jörg Urban. “QCD corrections to FCNC decays mediated by Z-penguins and W-boxes”. In: *Physics Letters B* 451.1–2 (Apr. 1999), pp. 161–169. ISSN: 0370-2693. DOI: `10.1016/s0370-2693(99)00150-1`. URL: `http://dx.doi.org/10.1016/S0370-2693(99)00150-1`.

[36] Andrzej J Buras et al. “Charm quark contribution to $K^+ \to \pi^+ \nu\bar{\nu}$ at next-to-next-to-leading order”. In: *Journal of High Energy Physics* 2006.11 (Nov. 2006), pp. 002–002. ISSN: 1029-8479. DOI: `10.1088/1126-6708/2006/11/002`. URL: `http://dx.doi.org/10.1088/1126-6708/2006/11/002`.

[37] Joachim Brod, Martin Gorbahn, and Emmanuel Stamou. “Two-loop electroweak corrections for the $K \to \pi\nu\bar{\nu}$ decays”. In: *Physical Review D* 83.3 (Feb. 2011). ISSN: 1550-2368. DOI: `10.1103/physrevd.83.034030`. URL: `http://dx.doi.org/10.1103/PhysRevD.83.034030`.

[38] Joachim Brod and Martin Gorbahn. “Electroweak corrections to the charm quark contribution to $K \to \pi\nu\bar{\nu}$”. In: *Physical Review D* 78.3 (Aug. 2008). ISSN: 1550-2368. DOI: `10.1103/physrevd.78.034006`. URL: `http://dx.doi.org/10.1103/PhysRevD.78.034006`.

[39] Gino Isidori, Federico Mescia, and Christopher Smith. "Light-quark loops in $K \to \pi\nu\bar{\nu}$". In: *Nuclear Physics B* 718.1–2 (July 2005), pp. 319–338. ISSN: 0550-3213. DOI: 10.1016/j.nuclphysb.2005.04.008. URL: http://dx.doi.org/10.1016/j.nuclphysb.2005.04.008.

[40] Federico Mescia and Christopher Smith. "Improved estimates of rare $K$ decay matrix elements from $K_{l3}$ decays". In: *Physical Review D* 76.3 (Aug. 2007). ISSN: 1550-2368. DOI: 10.1103/physrevd.76.034017. URL: http://dx.doi.org/10.1103/PhysRevD.76.034017.

[41] Andrzej J. Buras et al. "$K^+ \to \pi^+\nu\bar{\nu}$ and $K_L \to \pi^0\nu\bar{\nu}$ in the Standard Model: status and perspectives". In: *Journal of High Energy Physics* 2015.11 (Nov. 2015). ISSN: 1029-8479. DOI: 10.1007/jhep11(2015)033. URL: http://dx.doi.org/10.1007/JHEP11(2015)033.

[42] A. Höcker et al. "A new approach to a global fit of the CKM matrix". In: *The European Physical Journal C* 21.2 (June 2001), pp. 225–259. ISSN: 1434-6052. DOI: 10.1007/s100520100729. URL: http://dx.doi.org/10.1007/s100520100729.

[43] G. Anzivino et al. *Workshop summary – Kaons@CERN 2023*. 2024. arXiv: 2311.02923 [hep-ph].

[44] Andrzej J. Buras, Dario Buttazzo, and Robert Knegjens. "$K \to \pi\nu\bar{\nu}$ and $\epsilon/\epsilon$ in simplified new physics models". In: *Journal of High Energy Physics* 2015.11 (Nov. 2015). ISSN: 1029-8479. DOI: 10.1007/jhep11(2015)166. URL: http://dx.doi.org/10.1007/JHEP11(2015)166.

[45] Hiroaki Watanabe. "The new $K_L \to \pi^0\nu\bar{\nu}$ experiment (KOTO) at J-PARC". In: *PoS* ICHEP2010 (2010). Ed. by Bernard Pire et al., p. 274. DOI: 10.22323/1.120.0274.

[46] T. Nomura. "KOTO results and prospects". Kaons @ J-PARC 2024. July 2024. URL: https://conference-indico.kek.jp/event/273/contributions/5412/attachments/3619/4970/koto-240727-v1.pdf.

[47] A. V. Artamonov et al. "New Measurement of the $K^+ \to \pi^+\nu\bar{\nu}$ Branching Ratio". In: *Phys. Rev. Lett.* 101 (19 Nov. 2008), p. 191802. DOI: 10.1103/PhysRevLett.101.191802. URL: https://link.aps.org/doi/10.1103/PhysRevLett.101.191802.

[48] A. V. Artamonov et al. "Study of the decay $K^+ \to \pi^+\nu\bar{\nu}$ in the momentum region $140 < P_\pi < 199$ MeV/$c$". In: *Phys. Rev. D* 79 (9 May 2009), p. 092004. DOI: 10.1103/PhysRevD.79.092004. URL: https://link.aps.org/doi/10.1103/PhysRevD.79.092004.

[49] M. S. Atiya et al. "Search for a light Higgs boson in the decay $K^+ \to \pi^+$H, H$\to \mu^+\mu^-$". In: *Phys. Rev. Lett.* 63 (20 Nov. 1989), pp. 2177–2180. DOI: 10.1103/PhysRevLett.63.2177. URL: https://link.aps.org/doi/10.1103/PhysRevLett.63.2177.

[50] Aneesh Manohar and Howard Georgi. "Chiral Quarks and the Nonrelativistic Quark Model". In: *Nucl. Phys. B* 234 (1984), pp. 189–212. DOI: 10.1016/0550-3213(84)90231-1.

[51] A Pich. "Chiral perturbation theory". In: *Reports on Progress in Physics* 58.6 (June 1995), pp. 563–609. ISSN: 1361-6633. DOI: 10.1088/0034-4885/58/6/001. URL: http://dx.doi.org/10.1088/0034-4885/58/6/001.

[52] J Gasser and H Leutwyler. "Chiral perturbation theory to one loop". In: *Annals of Physics* 158.1 (1984), pp. 142–210. ISSN: 0003-4916. DOI: https://doi.org/10.1016/0003-4916(84)90242-2. URL: https://www.sciencedirect.com/science/article/pii/0003491684902422.

[53] Stefan Scherer. "Introduction to Chiral Perturbation Theory". In: *Advances in Nuclear Physics, Volume 27*. Ed. by J. W. Negele and E. W. Vogt. Boston, MA: Springer US, 2003, pp. 277–538. ISBN: 978-0-306-47916-8. DOI: 10.1007/0-306-47916-8_2. URL: https://doi.org/10.1007/0-306-47916-8_2.

[54] J. J. Hernandez et al. “Review of particle properties. Particle Data Group”. In: *Phys. Lett. B* 239 (1990). [Erratum: Phys.Lett.B 253, 524–527 (1991)], pp. 1–515. DOI: 10.1016/0370-2693(91)91762-K.

[55] H. Leutwyler and M. Roos. “Determination of the Elements V(us) and V(ud) of the Kobayashi-Maskawa Matrix”. In: *Z. Phys. C* 25 (1984), p. 91. DOI: 10.1007/BF01571961. URL: https://link.springer.com/article/10.1007/BF01571961.

[56] J. Gasser and H. Leutwyler. “Chiral perturbation theory: Expansions in the mass of the strange quark”. In: *Nuclear Physics B* 250.1 (1985), pp. 465–516. ISSN: 0550-3213. DOI: https://doi.org/10.1016/0550-3213(85)90492-4. URL: https://www.sciencedirect.com/science/article/pii/0550321385904924.

[57] M Tanabashi et al. “Review of Particle Physics, 2018-2019”. In: *Phys. Rev. D* 98.3 (2018), p. 030001. DOI: 10.1103/PhysRevD.98.030001. URL: https://cds.cern.ch/record/2636832.

[58] L. Marsicano et al. “Probing leptophilic dark sectors at electron beam-dump facilities”. In: *Physical Review D* 98.11 (Dec. 2018). ISSN: 2470-0029. DOI: 10.1103/physrevd.98.115022. URL: http://dx.doi.org/10.1103/PhysRevD.98.115022.

[59] J. P. Lees et al. “Search for a muonic dark force atBaBar”. In: *Physical Review D* 94.1 (July 2016). ISSN: 2470-0029. DOI: 10.1103/physrevd.94.011102. URL: http://dx.doi.org/10.1103/PhysRevD.94.011102.

[60] CERN Geographic Information System. URL: https://gis.cern.ch/.

[61] Giorgio Brianti and Niels T Doble. *The SPS North Area High Intensity Facility: a review of the project and of possible beams.* Tech. rep. Geneva: CERN, 1977. URL: http://cds.cern.ch/record/643069.

[62] E. Cortina Gil et al. “The beam and detector of the NA62 experiment at CERN”. In: *Journal of Instrumentation* 12.05 (May 2017), P05025–P05025. ISSN: 1748-0221. DOI: 10.1088/1748-0221/12/05/p05025. URL: http://dx.doi.org/10.1088/1748-0221/12/05/P05025.

[63] Claude Bovet et al. *The CEDAR counters for particle identification in the SPS secondary beams: a description and an operation manual.* CERN Yellow Reports: Monographs. Geneva: CERN, 1982. DOI: 10.5170/CERN-1982-013. URL: https://cds.cern.ch/record/142935.

[64] Evgueni Goudzovski et al. “Development of the kaon tagging system for the NA62 experiment at CERN”. In: *Nuclear Instruments and Methods in Physics Research Section A: Accelerators, Spectrometers, Detectors and Associated Equipment* 801 (2015), pp. 86–94. ISSN: 0168-9002. DOI: https://doi.org/10.1016/j.nima.2015.08.015. URL: https://www.sciencedirect.com/science/article/pii/S0168900215009493.

[65] The NA62 Collaboration. “Development of a new CEDAR for kaon identification at the NA62 experiment at CERN”. In: (2023). arXiv: 2312.17188 [hep-ex].

[66] M. Fiorini et al. “High rate particle tracking and ultra-fast timing with a thin hybrid silicon pixel detector”. In: *Nucl. Instrum. Meth. A* 718 (2013). Ed. by Franco Cervelli et al., pp. 270–273. DOI: 10.1016/j.nima.2012.10.108.

[67] H.J. Ziock et al. “Temperature dependence of radiation damage and its annealing in silicon detectors”. In: *Nuclear Science, IEEE Transactions on* 40 (Sept. 1993), pp. 344–348. DOI: 10.1109/23.256577.

[68] A. Kluge et al. “The TDCpix readout ASIC: A 75ps resolution timing front-end for the NA62 Gigatracker hybrid pixel detector”. In: *Nuclear Instruments and Methods in Physics Research Section A: Accelerators, Spectrometers, Detectors and Associated Equipment* 732 (2013). Vienna Conference on Instrumentation 2013, pp. 511–514. ISSN: 0168-9002. DOI: https://doi.org/10.1016/j.nima.2013.06.089. URL: https://www.sciencedirect.com/science/article/pii/S0168900213009352.

[69] F. Ambrosino et al. “CHANTI: a fast and efficient charged particle veto detector for the NA62 experiment at CERN”. In: *Journal of Instrumentation* 11.03 (Mar. 2016), P03029. DOI: 10.1088/1748-0221/11/03/P03029. URL: https://dx.doi.org/10.1088/1748-0221/11/03/P03029.

[70] Roland Winston. “Light Collection within the Framework of Geometrical Optics∗”. In: *J. Opt. Soc. Am.* 60.2 (Feb. 1970), pp. 245–247. DOI: 10.1364/JOSA.60.000245. URL: https://opg.optica.org/abstract.cfm?URI=josa-60-2-245.

[71] I. Panichi. “High level performance of the NA62 RICH detector”. In: *Nuclear Instruments and Methods in Physics Research Section A: Accelerators, Spectrometers, Detectors and Associated Equipment* 1045 (2023), p. 167583. ISSN: 0168-9002. DOI: https://doi.org/10.1016/j.nima.2022.167583. URL: https://www.sciencedirect.com/science/article/pii/S0168900222008750.

[72] G. Anzivino et al. “Light detection system and time resolution of the NA62 RICH”. In: *Journal of Instrumentation* 15.10 (Oct. 2020), P10025. DOI: 10.1088/1748-0221/15/10/P10025. URL: https://dx.doi.org/10.1088/1748-0221/15/10/P10025.

[73] V. Fanti et al. “The beam and detector for the NA48 neutral kaon CP violation experiment at CERN”. In: *Nuclear Instruments and Methods in Physics Research Section A: Accelerators, Spectrometers, Detectors and Associated Equipment* 574.3 (2007), pp. 433–471. ISSN: 0168-9002. DOI: https://doi.org/10.1016/j.nima.2007.01.178. URL: https://www.sciencedirect.com/science/article/pii/S0168900207002719.

[74] D.A. Gedcke and W.J. McDonald. “A constant fraction of pulse height trigger for optimum time resolution”. In: *Nuclear Instruments and Methods* 55 (1967), pp. 377–380. ISSN: 0029-554X. DOI: https://doi.org/10.1016/0029-554X(67)90145-0. URL: https://www.sciencedirect.com/science/article/pii/0029554X67901450.

[75] S. Kholodenko. “NA62 Charged Particle Hodoscope. Design and performance in 2016 run”. In: *Journal of Instrumentation* 12.06 (June 2017), pp. C06042–C06042. ISSN: 1748-0221. DOI: 10.1088/1748-0221/12/06/c06042. URL: http://dx.doi.org/10.1088/1748-0221/12/06/C06042.

[76] A Ceccucci et al. “The NA62 liquid Krypton calorimeter’s new readout system”. In: *Journal of Instrumentation* 9.01 (Jan. 2014), p. C01047. DOI: 10.1088/1748-0221/9/01/C01047. URL: https://dx.doi.org/10.1088/1748-0221/9/01/C01047.

[77] Guillaume Unal. *Performances of the NA48 Liquid Krypton calorimeter*. 2000. arXiv: hep-ex/0012011 [hep-ex].

[78] M Jeitler. “The NA48 liquid-krypton calorimeter”. In: *Nuclear Instruments and Methods in Physics Research Section A: Accelerators, Spectrometers, Detectors and Associated Equipment* 494.1 (2002). Proceedings of the 8th International Conference on Instrumentatio n for Colliding Beam Physics, pp. 373–377. ISSN: 0168-9002. DOI: https://doi.org/10.1016/S0168-

9002(02)01505-X. URL: https://www.sciencedirect.com/science/article/pii/S016890020201505X.

[79] F. Ambrosino et al. *The Large-Angle Photon Veto System for the NA62 Experiment at CERN.* 2011. arXiv: 1111.4075 [physics.ins-det].

[80] OPAL Collaboration. “The OPAL detector at LEP”. In: *Nuclear Instruments and Methods in Physics Research Section A: Accelerators, Spectrometers, Detectors and Associated Equipment* 305.2 (1991), pp. 275–319. ISSN: 0168-9002. DOI: https://doi.org/10.1016/0168-9002(91)90547-4. URL: https://www.sciencedirect.com/science/article/pii/0168900291905474.

[81] A Antonelli et al. “Performance of the NA62 LAV front-end electronics”. In: *Journal of Instrumentation* 8.01 (Jan. 2013), p. C01020. DOI: 10.1088/1748-0221/8/01/C01020. URL: https://dx.doi.org/10.1088/1748-0221/8/01/C01020.

[82] F Hahn et al. *NA62: Technical Design Document.* Tech. rep. Geneva: CERN, 2010. URL: https://cds.cern.ch/record/1404985.

[83] M. B. Golubeva et al. “Forward hadron calorimeter for measurements of projectile spectators in heavy-ion experiment”. In: *Phys. Atom. Nucl.* 75 (2012), pp. 673–675. DOI: 10.1134/S1063778812060142.

[84] NA62 Collaboration. *2022 NA62 Status Report to the CERN SPSC.* Tech. rep. Geneva: CERN, 2022. URL: https://cds.cern.ch/record/2805351.

[85] Soo Ryu and on behalf of the ATLAS TDAQ Collaboration. “FELIX: The new detector readout system for the ATLAS experiment”. In: *Journal of Physics: Conference Series* 898.3 (Oct. 2017), p. 032057. DOI: 10.1088/1742-6596/898/3/032057. URL: https://dx.doi.org/10.1088/1742-6596/898/3/032057.

[86] Collaboration NA62. *2023 NA62 Status Report to the CERN SPSC.* Tech. rep. Geneva: CERN, 2023. URL: https://cds.cern.ch/record/2856997.

[87] *8th Workshop on Electronics for LHC Experiments: Colmar, France 9 - 13 Sep 2002.* CERN. Geneva: CERN, 2002. DOI: 10.5170/CERN-2002-003. URL: https://cds.cern.ch/record/592042.

[88] R. Ammendola et al. “The integrated low-level trigger and readout system of the CERN NA62 experiment”. In: *Nuclear Instruments and Methods in Physics Research Section A: Accelerators, Spectrometers, Detectors and Associated Equipment* 929 (June 2019), pp. 1–22. ISSN: 0168-9002. DOI: 10.1016/j.nima.2019.03.012. URL: http://dx.doi.org/10.1016/j.nima.2019.03.012.

[89] D. Soldi and S. Chiozzi. “Level Zero Trigger Processor for the NA62 experiment”. In: *Journal of Instrumentation* 13.05 (May 2018), P05004. DOI: 10.1088/1748-0221/13/05/P05004. URL: https://dx.doi.org/10.1088/1748-0221/13/05/P05004.

[90] The NA62 Collaboration. *Performance of the NA62 trigger system.* 2023. arXiv: 2208.00897 [hep-ex].

[91] G. Haefeli et al. “The LHCb DAQ interface board TELL1”. In: *Nuclear Instruments and Methods in Physics Research Section A: Accelerators, Spectrometers, Detectors and Associated Equipment* 560.2 (2006), pp. 494–502. ISSN: 0168-9002. DOI: https://doi.org/10.1016/j.nima.2005.12.212. URL: https://www.sciencedirect.com/science/article/pii/S0168900205026100.

[92] B. Angelucci et al. “TEL62: an integrated trigger and data acquisition board”. In: *2011 IEEE Nuclear Science Symposium Conference Record*. 2011, pp. 823–826. DOI: 10.1109/NSSMIC.2011.6154547.

[93] Elena Pedreschi et al. “A High-Resolution TDC-Based Board for a Fully Digital Trigger and Data Acquisition System in the NA62 Experiment at CERN”. In: *IEEE Transactions on Nuclear Science* 62.3 (June 2015), pp. 1050–1055. ISSN: 1558-1578. DOI: 10.1109/tns.2015.2423702. URL: http://dx.doi.org/10.1109/TNS.2015.2423702.

[94] D Moraes et al. *The CARIOCA Front End Chip for the LHCb muon chambers*. Tech. rep. Geneva: CERN, 2003. URL: http://cds.cern.ch/record/691709.

[95] A Ceccucci et al. “The NA62 Liquid Krypton calorimeter readout module”. In: *Journal of Instrumentation* 6.12 (Dec. 2011), p. C12017. DOI: 10.1088/1748-0221/6/12/C12017. URL: https://dx.doi.org/10.1088/1748-0221/6/12/C12017.

[96] NA62 Collaboration. *NA62 Framework*. URL: https://na62-sw.web.cern.ch.

[97] Karl L Brown and F Christoph Iselin. *DECAY TURTLE (Trace Unlimted Rays Through Lumped Elements): a computer program for simulating charged-particle beam transport systems, including decay calculations*. CERN Yellow Reports: Monographs. Geneva: CERN, 1974. DOI: 10.5170/CERN-1974-002. URL: http://cds.cern.ch/record/186178.

[98] L.J. Nevay et al. “BDSIM: An accelerator tracking code with particle–matter interactions”. In: *Computer Physics Communications* 252 (July 2020), p. 107200. ISSN: 0010-4655. DOI: 10.1016/j.cpc.2020.107200. URL: http://dx.doi.org/10.1016/j.cpc.2020.107200.

[99] S. Agostinelli et al. “Geant4—a simulation toolkit”. In: *Nuclear Instruments and Methods in Physics Research Section A: Accelerators, Spectrometers, Detectors and Associated Equipment* 506.3 (2003), pp. 250–303. ISSN: 0168-9002. DOI: https://doi.org/10.1016/S0168-9002(03)01368-8. URL: https://www.sciencedirect.com/science/article/pii/S0168900203013688.

[100] Rene Brun and Fons Rademakers. “ROOT — An object oriented data analysis framework”. In: *Nuclear Instruments and Methods in Physics Research Section A: Accelerators, Spectrometers, Detectors and Associated Equipment* 389.1 (1997). New Computing Techniques in Physics Research V, pp. 81–86. ISSN: 0168-9002. DOI: https://doi.org/10.1016/S0168-9002(97)00048-X. URL: https://www.sciencedirect.com/science/article/pii/S016890029700048X.

[101] H. Danielsson et al. “New veto hodoscope ANTI-0 for the NA62 experiment at CERN”. In: *Journal of Instrumentation* 15.07 (July 2020), pp. C07007–C07007. ISSN: 1748-0221. DOI: 10.1088/1748-0221/15/07/c07007. URL: http://dx.doi.org/10.1088/1748-0221/15/07/C07007.

[102] A. Calcaterra et al. “Proposal to study the design and technology of a veto detector (ANTI-0) upstream of the decay vessel of the NA62 Experiment”. NA62 Internal Note 17-01. Jan. 2017. URL: https://na62.web.cern.ch/restricted/NotesDoc/NA62-17-01.pdf.

[103] L. Gatignon and N. Doble. “Comparisons T10 target IN versus target OUT with K12 TAX open or closed”. NA62 Internal Note 16-14. Dec. 2016. URL: https://na62.web.cern.ch/restricted/NotesDoc/NA62-16-14.pdf.

[104] Babette Döbrich. *Dark Sectors at fixed targets: The example of NA62*. 2018. arXiv: 1807.10170 [hep-ex]. URL: https://arxiv.org/abs/1807.10170.

[105] The NA62 collaboration. *Search for leptonic decays of the dark photon at NA62*. 2023. arXiv: 2312.12055 [hep-ex]. URL: https://arxiv.org/abs/2312.12055.

[106] NA62 Collaboration. *Search for dark photon decays to $\mu^+\mu^-$ at NA62*. 2023. arXiv: 2303.08666 [hep-ex]. URL: https://arxiv.org/abs/2303.08666.

[107] S. Kholodenko. "Status of ANTI-0". NA62 Weekly Meeting. June 2021. URL: https://indico.cern.ch/event/1046830/contributions/4408269/attachments/2265505/3847983/ANTI-0_status_17062021.pdf.

[108] Sunghwan Kim et al. "PubChem 2023 update". In: *Nucleic Acids Research* 51.D1 (Oct. 2022), pp. D1373–D1380. ISSN: 0305-1048. DOI: 10.1093/nar/gkac956. eprint: https://academic.oup.com/nar/article-pdf/51/D1/D1373/48441598/gkac956.pdf. URL: https://doi.org/10.1093/nar/gkac956.

[109] S A Kholodenko et al. "Time resolution measurements of scintillating counters for a new NA62 trigger charged hodoscope". In: *Journal of Instrumentation* 9.09 (Sept. 2014), p. C09002. DOI: 10.1088/1748-0221/9/09/C09002. URL: https://dx.doi.org/10.1088/1748-0221/9/09/C09002.

[110] Gerald R. Lynch and Orin I. Dahl. "Approximations to multiple Coulomb scattering". In: *Nuclear Instruments and Methods in Physics Research Section B: Beam Interactions with Materials and Atoms* 58.1 (1991), pp. 6–10. ISSN: 0168-583X. DOI: https://doi.org/10.1016/0168-583X(91)95671-Y. URL: https://www.sciencedirect.com/science/article/pii/0168583X9195671Y.

[111] S. Kholodenko. "ANTI0 in dump mode". NA62 Weekly Meeting. Oct. 2021. URL: https://indico.cern.ch/event/1091870/contributions/4591098/attachments/2336730/3982885/ANTI0_NewCHOD_RunMeeting_29October.pdf.

[112] S. Ruggiero. "Instensity Studies Update". NA62 Collaboration Meeing. Sept. 2023. URL: https://indico.cern.ch/event/1234203/contributions/5563467/attachments/2708447/4702622/PinunuWG_05_09_2023.pdf.

[113] L. Bician. "New Measurement of $K^+ \to \pi^+\mu^+\mu^-(\gamma)$ Decay with NA62 Run 1 Data". NA62 Internal Note 22-02. May 2022. URL: https://na62.web.cern.ch/restricted/NotesDoc/NA62-22-02.pdf.

[114] P. Billoir, R. Frühwirth, and M. Regler. "Track element merging strategy and vertex fitting in complex modular detectors". In: *Nuclear Instruments and Methods in Physics Research A* 241.1 (Nov. 1985), pp. 115–131. DOI: 10.1016/0168-9002(85)90523-6.

[115] V. Duk. "Search for resonances in $K^+ \to \pi^+X(X \to \mu^+\mu^-)$ decay". NA62 Lepton Flavour Working Group Meeting. July 2018. URL: https://indico.cern.ch/event/743094/contributions/3072923/attachments/1689624/2718281/inflaton_search_19jul18.pdf.

[116] J.R. Batley et al. "Searches for lepton number violation and resonances in $K^+ \to \pi\mu\mu$ decays". In: *Physics Letters B* 769 (2017), pp. 67–76. ISSN: 0370-2693. DOI: https://doi.org/10.1016/j.physletb.2017.03.029. URL: https://www.sciencedirect.com/science/article/pii/S0370269317302174.

[117] M. Boretto. "$K_{\mu\nu\mu\mu}$ analysis". NA62 Rare Decays Working Group Meeting. June 2020. URL: https://indico.cern.ch/event/927016/contributions/3917114/attachments/2063184/3461678/PhD_Final_presentation___Kmunumumu_analysis1.pdf.